2019-01-01

Material Characterizations Of Organic-Inorganic Halide Perovskites Using Various Deposition Techniques For Planar Perovskite Solar Cell

Shaimum Shahriar
University of Texas at El Paso

MATERIAL CHARACTERIZATIONS OF ORGANIC-INORGANIC HALIDE PEROVSKITES USING VARIOUS DEPOSITION TECHNIQUES FOR PLANAR PEROVSKITE SOLAR CELL

SHAIMUM SHAHRIAR

Doctoral Program in Electrical and Computer Engineering

APPROVED:

Deidra Hodges, Ph.D., Chair

John Moya, Ph.D.

Norman Love, Ph.D.

Stephen Crites, Ph.D.
Dean of the Graduate School

Dedication

I dedicate this thesis to my family for their constant support and unconditional love.

I love you all dearly.

MATERIAL CHARACTERIZATIONS OF ORGANIC-INORGANIC HALIDE PEROVSKITES USING VARIOUS DEPOSITION TECHNIQUES FOR PLANAR PEROVSKITE SOLAR CELL

by

SHAIMUM SHAHRIAR, M.S.

DISSERTATION

Presented to the Faculty of the Graduate School of

The University of Texas at El Paso

in Partial Fulfillment

of the Requirements

for the Degree of

DOCTOR OF PHILOSOPHY

Department of Electrical and Computer Engineering

THE UNIVERSITY OF TEXAS AT EL PASO

December 2019

Acknowledgements

This work was supported by (i) the departments of (a) Electrical & Computer Engineering and (b) Metallurgical, Materials and Biomedical Engineering and the Office of Research and Sponsored Projects at the University of Texas at El Paso and (ii) the Center for Functional Nanomaterials at the Brookhaven National Laboratory.

Abstract

Organic–inorganic halide perovskites have rapidly become emerging materials for photovoltaic applications. Strong characterization methods are needed to fully comprehend the chemistry and composition of perovskite solar cells. Understanding the interaction between layers inside a cell and how they react with the environment is important to achieve optimum manufacturing processes, and improve the efficiency of perovskite solar cells. The present work demonstrates the material characterizations of organic–inorganic halide perovskites using (i) one-step deposition, (ii) two-steps deposition, (iii) solvent-to-solvent extraction, and (iv) mixed-cation solution processing. Investigations by X-ray photoelectron spectroscopy (XPS), X-ray diffraction (XRD), and scanning electron microscopy (SEM) have been undertaken to better understand the oxidation of core elements of perovskites, film crystallography, morphology, and stoichiometry when using different deposition techniques of perovskites. Time resolved photoluminescence (TRPL) and photoluminescence (PL) allow us to clearly interpret the lifetime and the bandgap of perovskite material. UV-Vis spectrophotometer results help us to investigate the influence of various deposition techniques on optoelectronic properties of perovskite. Mixed-cation perovskites show the most promising results among the four deposition techniques. The best photovoltaic performance is achieved by a SnO_2-based mixed-cation perovskite solar cell with a power conversion efficiency of 18.75%. A power conversion efficiency of 16.74% is obtained by a TiO_2-based mixed-cation perovskite solar cell when the optimum thickness of the TiO_2 blocking layer is 60–65 nm.

Table of Contents

Dedication iii

Acknowledgements v

Abstract vi

Table of Contents vii

List of Tables x

List of Figures xi

Chapter 1: Introduction 1

1.1 The global energy challenge 2

1.2 Basic operation principles of photovoltaics 3

1.3 What is perovskite 5

1.4 Perovskite classification 6

1.5 Organic metal perovskite structure 7

1.6 Why perovskite 9

1.7 Perovskite photovoltaic technology 14

1.8 State of art 17

1.9 Motivation and strategies 21

Chapter 2: Experimental Methods 23

2.1 Introduction 23

2.2 One step deposition 23

2.3 Two steps deposition 25

2.4 Solvent to solvent extraction 26

2.5 Mixed cation solution processing 27

2.6 Summary 27

Chapter 3: Material Characterizations 29

3.1 Introduction 29

3.2 Crystallography: XRD 29

3.3 Morphology: SEM 31

3.4 Surface topology: AFM 33

3.5 Optical properties: UV-Vis 34
3.6 Electronic properties: PL, TRPL, Hall 39
3.7 Surface chemistry: XPS 42
3.8 Summary 44

Chapter 4: ETM, Absorber and HTM Layers Optimization 46
4.1 Introduction 46
4.2 Mesoporous TiO_2 46
4.2.1 Deposition 46
4.2.2 Characterization 47
4.3 Solaronix TiO_2 blocking layer 49
4.3.1 Deposition 49
4.3.2 Characterization 49
4.4 Influence of temperature and thickness on ETM layer 51
4.5 Bilayer perovskite 53
4.6 Spiro-OMeTAD is better HTM than P3HT 54
4.7 Summary 55

Chapter 5: Device Fabrication 56
5.1 Introduction 56
5.2 Transparent conducting oxide (TCO) layer 58
5.3 ETM layer 58
5.5 HTM layer 59
5.6 Back contact 59
5.7 Summary 59

Chapter 6: Device Characterization 61
6.1 Introduction 61
6.2 J-V characterization 61
6.2.1 One Step Bilayer Deposition Based Planar Perovskite Solar Cells 61
6.2.2 Mixed Cation Solution Processing Based Planar Perovskite Solar Cells 62
6.3 Dark J-V characterization 63
6.3.1 One Step Bilayer Deposition Based Planar Perovskite Solar Cells 63
6.3.2 Mixed Cation Solution Processing Based Planar Perovskite Solar Cells 64
6.4 J-V comparison between TiO_2 and SnO_2 based planar perovskite solar cells 67

6.5 Power conversion efficiency (PCE) Histograms 70
6.6 External quantum efficiency (EQE)....71
6.7 Summary....72
Chapter 7: Degradation....73
7.1 Introduction....73
7.2 One step deposition....77
7.3 Two steps deposition....77
7.4 Mixed cation solution processing 78
7.5 Summary....78
Chapter 8: Conclusion....79
References....81
Appendix....85
Vita 86

List of Tables

Table 3.1: Crystallite size of perovskite using the Scherrer equation for the (110) peak, calculated from XRD patterns obtained under ambient conditions. 31
Table 3.2: Average grain diameter of perovskite calculated from SEM image. 33
Table 3.3: Extracted bandgap of perovskites from PL spectra. 40
Table 3.4: Extracted the fitting decay lifetimes of τ_1, τ_2 and the average lifetime τ_{avg} from TRPL. 41
Table 3.5: Mobility (μ), Bulk Concentration (N_b), Resistivity (ρ), Conductivity (σ) at room temperature. 42
Table 3.6: Type of semiconductor depends on the quantity of MAI and PbI_2. 42
Table 3.7: Calculations of the atomic percentage of each element and the ratio of I:Pb for one step deposition. 44
Table 3.8: Calculations of the atomic percentage of each element and the ratio of I:Pb for two steps deposition. 44
Table 3.9: Calculations of the atomic percentage of each element and the ratio of I:Pb for solvent to solvent extraction deposition. 44
Table 3.10: Calculations of the atomic percentage of each element and the ratio of I:Pb for mixed cation solution processing. 44
Table 4.1: Effect on bulk concentration, mobility, resistivity and conductivity by annealing the TiO_2 blocking layer. 52
Table 4.2: Effect on mobility of perovskite layer with Spiro-OMeTAD and P3HT. 55
Table 7.1: Calculated degradation rate after 100 hours. 78

List of Figures

Figure 1.1: Projected non-hydro power renewable electricity generation worldwide. 2
Figure 1.2: The principle of operation of the solar cell. 4
Figure 1.3: Perovskite ABX_3 crystal structure where typically A = $CH_3NH_3^+$, $CH(NH_2)_2^+$, B = Pb^{2+}, Sn^{2+} and X = I^-, Br^-, Cl^-, or mixtures thereof. 5
Figure 1.4: Classification of perovskite. 7
Figure 1.5: Methylammonium cation ($CH_3NH_3^+$) is surrounded by PbX_6 octahedral. 8
Figure 1.6: The absorption coefficient, α, in a variety of semiconductor materials at 300K as a function of the vacuum wavelength of light. 9
Figure 1.7: Absorption coefficient Vs Wavelength for various perovskite deposition techniques 10
Figure 1.8: Time-Resolved Photoluminescence (TRPL) shows long carrier lifetime for perovskite. 11
Figure 1.9: Limiting solar cell efficiency as a function of the material bandgap for one-sun illumination. 12
Figure 1.10: Photoluminescence (PL) shows 1.6eV bandgap for one step deposition 13
Figure 1.11: Classification of photovoltaic technology. 15
Figure 1.12: Best Research-Cell Efficiency Chart 17
Figure 1.13: Photovoltaic Characteristics of Perovskite-Based Cells 18
Figure 1.14: Cross-sectional SEM image of the device 18
Figure 1.15: Inverted planar-heterojunction perovskite device. 19
Figure 1.16: Diagram of energy levels (relative to the vacuum level) of each functional layer in the device. 20
Figure 1.17: Diagram of the device configuration. 21
Figure 1.18: Research flow chart. 22
Figure 2.1: Flow chart of synthesizing MAI. 24
Figure 2.2: Flow chart for one step deposition. 24
Figure 2.3: Flow chart for two steps deposition. 25
Figure 2.4: Flow chart for solvent to solvent extraction deposition. 26
Figure 2.5: Flow chart for mixed cation solution processing. 27
Figure 3.1: XRD profiles of perovskites show the main diffraction peaks. 30
Figure 3.2: Low- and high-magnification SEM micrographs of the top surface of perovskite films deposited on a glass substrate. 32
Figure 3.3: AFM topographic 3D images of the surface of 2μm × 2μm films. 33
Figure 3.4: UV-vis absorbance and PL spectra of perovskite thin films. 34
Figure 3.5: Absorption coefficient (α) as a function of wavelength for perovskite. 35
Figure 3.6: The Dependence of the skin depth upon the photon energy of perovskites. 36
Figure 3.7: Variation of the optical density, OD as a function of the photon energy for perovskites. 37
Figure 3.8: Urbach energies extracted from absorbance measurements (UV-Vis) plotted against the bandgap. 38
Figure 3.9: PL spectra of the perovskite films. 39
Figure 3.10: Time resolution photoluminescence (TRPL) analysis of perovskite films. 40
Figure 3.11: X-ray photoelectron spectroscopy (XPS) survey spectra of perovskite films documented for I 3d5/2, and Pb 4f7/2. 43

Figure 4.1: XRD patterns of TiO_2 anatase mesoporous film. 47
Figure 4.2: Low- and high-magnification SEM micrographs of the top surface of mesoporous TiO_2 films deposited on a glass substrate. 48
Figure 4.3: Current density vs voltage (J–V) curves from forward and reverse scans of mesoporous TiO_2 based one step deposition PSCs. 48
Figure 4.4: XRD patterns of TiO_2 anatase blocking layer film. 49
Figure 4.5: Optical transmission spectrum through anatase TiO_2 film. 50
Figure 4.6: Low- and high-magnification SEM micrographs of the top surface of solaronix blocking layer TiO_2 films deposited on a glass substrate. 50
Figure 4.7: Current density vs voltage (J–V) curves from forward and reverse scans of solaronix blocking layer TiO_2 based one step deposition PSCs. 51
Figure 4.8: Effect on bulk concentration (N_b) and mobility (μ) by increasing the thickness of TiO_2 blocking layer. 52
Figure 4.9: Mean roughness depth (R_z) comparison between single layer and bilayer one step deposition. 53
Figure 4.10: a) Optical transmission spectrum for perovskite, perovskite with Spiro-OMeTAD and perovskite with P3HT and b) Optical absorbance spectrum for perovskite, perovskite with Spiro-OMeTAD and perovskite with P3HT. 54
Figure 4.11: Energy bandgap diagram of hybrid perovskite materials. 54
Figure 5.1: Schematic diagrams of perovskite solar cells in the (a) n-i-p mesoscopic, (b) n-i-p planar, (c) p-i-n planar, and (d) p-i-n mesoscopic structures. 57
Figure 5.2: 3D structure and device fabrication processes of planar perovskite solar cell with one step deposition. 57
Figure 4.3: 3D structure and device fabrication processes of planar perovskite solar cell with mixed cation solution processing. 58
Figure 5.4: Top view after fabricate perovskite solar cells. 59
Figure 6.1: (a) Current density vs voltage (J–V) curves of one step planar perovskite solar cells (PSCs) under simulated one-sun AM 1.5G (100 mW/cm^2) illumination with different thicknesses of TiO_2 blocking layer, (b) effect of the TiO_2 film thickness on series resistance (R_{series}) of planar PSCs, (c) effect of the TiO_2 film thickness on open-circuit voltage (V_{oc}) and short-circuit current density (J_{sc}), and (d) effect of the TiO_2 film thickness on power conversion efficiency (PCE) and fill factor (FF). 61
Figure 6.2: (a) Current density vs voltage (J–V) curves of mixed-cation planar perovskite solar cells (PSCs) under simulated one-sun AM 1.5G (100 mW/cm^2) illumination with different thicknesses of blocking layer, which are achieved by varying the speed (5000 rpm, 6000 rpm, and 7000 rpm) of the spin coater while depositing the TiO_2 layer, (b) effect of the TiO_2 film thickness on series resistance (R_{series}) of planar PSCs, (c) effect of the TiO_2 film thickness on open-circuit voltage (V_{oc}) and short circuit current density (J_{sc}), and (d) effect of the TiO_2 film thickness on power conversion efficiency (PCE) and fill factor (FF). 62
Figure 6.3: Illuminate and dark current density-voltage (J-V) curves of one step deposition based perovskite solar cells. 63
Figure 6.4: Current density vs voltage (J–V) curves in the dark for different thicknesses of blocking layer with (a) semi logarithmic scale to identify the recombination mechanism and (b) natural-log scale to calculate the diode ideality factors (n) (the lines are fitted to the Shockley diode equation) 64

Figure 6.5: Current density vs voltage (J–V) curves in the dark for different electron transport layers with the semi logarithmic scale to identify the recombination mechanism. 66
Figure 6.6: Current density vs voltage (J–V) curves from forward and reverse scans of mixed-cation planar PSCs based on (a) spin-coated TiO_2 with a thickness of 60–65 nm and (b) spin-coated SnO_2 as an electron-transport layer. 67
Figure 6.7: Histogram of PCE measured from 15 one step deposition based devices, which shows an average PCE of a) 3.5% with 3BL and b) 3.5% with 4BL. 70
Figure 6.8: Histogram of PCE measured from 30 mixed cation based devices, which shows an average PCE of a) 13.5% with TiO_2 and b) 15.7% with SnO_2. 70
Figure 6.9: External quantum efficiency and the integrated current density of the perovskite solar cells 71
Figure 7.1: Chain of reactions from $MAPbI_3$ perovskites, catalyzed by water. 73
Figure 7.2: Possible crystal phases of perovskites depending on tolerance factor. 75
Figure 7.3: XRD patterns shows distinct peak of PbI_2 after two months of spin coating. 77
Figure 7.4: FTIR spectra of the perovskite. 77
X-ray photoelectron spectroscopy (XPS) survey spectra of perovskite films documented..... 85
for C 1s, O 1s, N 1s, I 3d5/2, and Pb 4f7/2. (a) One-step deposition, (b) Solvent-to-solvent 85
extraction (SSE), (c) Hot casting, and (d) Mixed-cation show the core-level spectra of the 85
different elements for perovskite films respectively..... 85

Chapter 1: Introduction

Solar cells are considered as one of the prominent sources of renewable energy suitable for large-scale adoption in a carbon-constrained world and can contribute to reduced reliance on energy imports, whilst improving the security of energy supply. A new arrival in the family of solar cells technologies is the organic-inorganic halide perovskite. The major thrust for endorsing these new solar cells pertains to their potential as an economically and environmentally viable option to traditional silicon-based technology. Perovskite solar cells (PSCs) have recently emerged as so called "next generation solar cells". Across the years, there has been a remarkable improvement in the efficiencies of photovoltaic (PV) technologies and their deployment. For instance, traditional solar cells constructed using silicon have yielded efficiency of up to 25%. Those built using gallium arsenide, which are considerably more expensive, have recorded efficiency of roughly 29% and 40% in single and multi-junction devices, respectively [1]. Over time, PV technologies based on thin-film polycrystalline materials, emerged as a potential alternative to silicon-based cells with efficiencies > 20% [2]. These developments led to the arrival of "next generation solar cells" [3] or "emerging photovoltaics", which are designed to ensure significant cost reduction of the module manufacturing and widen the applications of devices to compete with other systems of energy production [4]. PSCs were first introduced in 2009 as a promising architecture for high-efficiency devices but initial studies only reported an efficiency of 3.8% [5]. After years of active research, the efficiency has reached up to 25.2% in 2018 [6]. With the rapid growth of efficiency from 3.8% to 25.2% in recent years, PSCs have drawn significant attention of researchers from both academia and industry.

1.1 THE GLOBAL ENERGY CHALLENGE

Today's energy landscape is dominated by the use of fossil fuels, like oil, natural gas and coal. These types of energy carrier took millions of years to be formed and thus humankind will run out of them sooner or later [7]. New forms of energy will have to be utilized to sustain our energy intake past this point. But the development of so-called renewable energies, like wind, tide and solar, is not only driven by the need to satisfy our ever-growing demand for energy. Continuously burning fossil fuels over the past 150 years and the concurrent release of the combustion products into the atmosphere has caused a so-called greenhouse effect. This means that the energy emitted from the sun and being reflected from the earth cannot be emitted back into space as efficiently, but rather stays in our atmosphere to a greater extent. This additional energy heats up the world's atmosphere – we encounter global warming [8].

To keep the Earth an inhabitable planet for future generations, we need to change the way we produce our energy as soon as possible. While energy from wind and water is already utilized with high efficiencies [9], solar energy only encounters a niche importance. Less than 1 percent of the world's total electricity production can be attributed to photovoltaic [10]. It is estimated that about 3.5 $x10^{24}$ J of solar energy reach the Earth's surface every year. That is approximately 10,000 times more energy than the total annual human consumption [11].

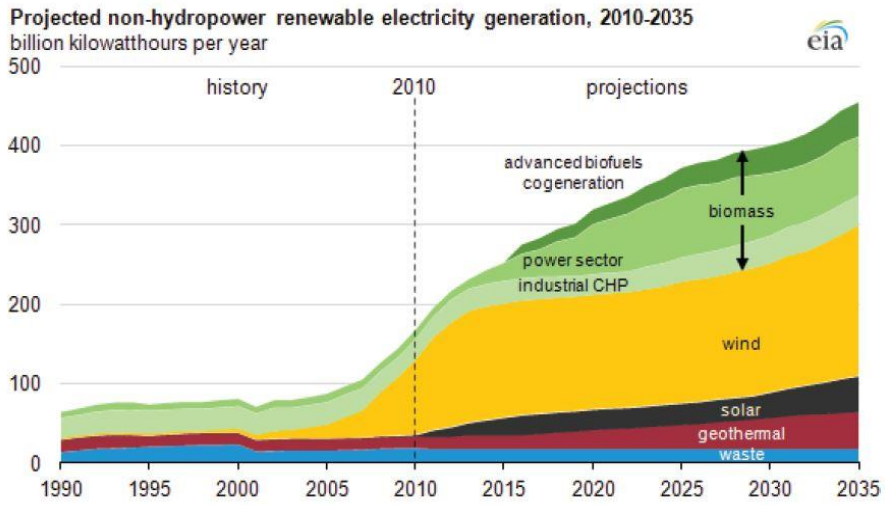

Figure 1.1: Projected non-hydro power renewable electricity generation worldwide.

1.2 BASIC OPERATION PRINCIPLES OF PHOTOVOLTAICS

A simplified schematic diagram of a typical solar cell is shown in Figure 1.2. Consider a p-n junction with a very narrow and more heavily doped n -region. The illumination is through the thin n-side. The depletion region (W) or the space charge layer (SCL) extends primarily into the p-side. There is a built-in field E_0 in this depletion layer. The electrodes attached to the n-side must allow illumination to enter the device and at the same time result in a small series resistance. They are deposited on the n-side to form an array of finger electrodes on the surface. As the n-side is very narrow, most of the photons are absorbed within the depletion region (W) and within the neutral p-side (l_p) and photogenerate EHPs in these regions. EHPs photogenerated in the depletion region are immediately separated by the built-in field £0 which drifts them apart. The electron drifts and reaches the neutral n^+ side whereupon it makes this region negative by an amount of charge -e. Similarly, the hole drifts and reaches the neutral p-side and thereby makes this side positive. Consequently an open circuit voltage develops between the terminals of the device with the p-side positive with respect to the n-side. If an external load is connected, then the excess electron in the n-side can travel around the external circuit, do work, and reach the p-side to recombine with the excess hole there. It is important to realize that without the internal field E_0 it is not possible to drift apart the photogenerated HHPs and accumulate excess electrons on the n-side and excess holes on thep-side. The EHPs photogenerated by long-wavelength photons that are absorbed in the neutral p-side diffuse around in this region as there is no electric field. If the recombination lifetime of the electron is τ_e, it diffuses a mean distance $L_e = \sqrt{2D_e\tau_e}$ where D_e is its diffusion coefficient in the p-side. Those electrons within a distance L_e to the depletion region can readily diffuse and reach this region whereupon they become drifted by to the n-side as shown in Figure 1.2. Consequently only those EHPs photogenerated within the minority carrier diffusion length L_e to the depletion layer can contribute to the photovoltaic effect. Again the importance of the built-in field E_0 is apparent. Once an electron diffuses to the depletion region, it is swept over to the n-side by E_0 to give an additional negative charge there.

Holes left behind in the p-side contribute a net positive charge to this region. Those photogenerated EHPs further away from the depletion region than L_e are lost by recombination. It is therefore important to have the minority carrier diffusion length L_e be as long as possible. This is the reason for choosing this side of a Si pn junction to be p-type which makes electrons the minority carriers; the electron diffusion length in Si is longer than the hole diffusion length. The same ideas also apply to EHPs photogenerated by short wavelength photons absorbed in the n-side. Those holes photogenerated within a diffusion length L_h can reach the depletion layer and become swept across to the p-side. The photogeneration of EHPs that contributes to the photovoltaic effect therefore occurs in a volume covering $L_h + W + L_e$. If the terminals of the device are shorted, then the excess electron in the n-side can flow through the external circuit to neutralize the excess hole in the p-side. This current due to the flow of the photogenerated carriers is called the photocurrent [12].

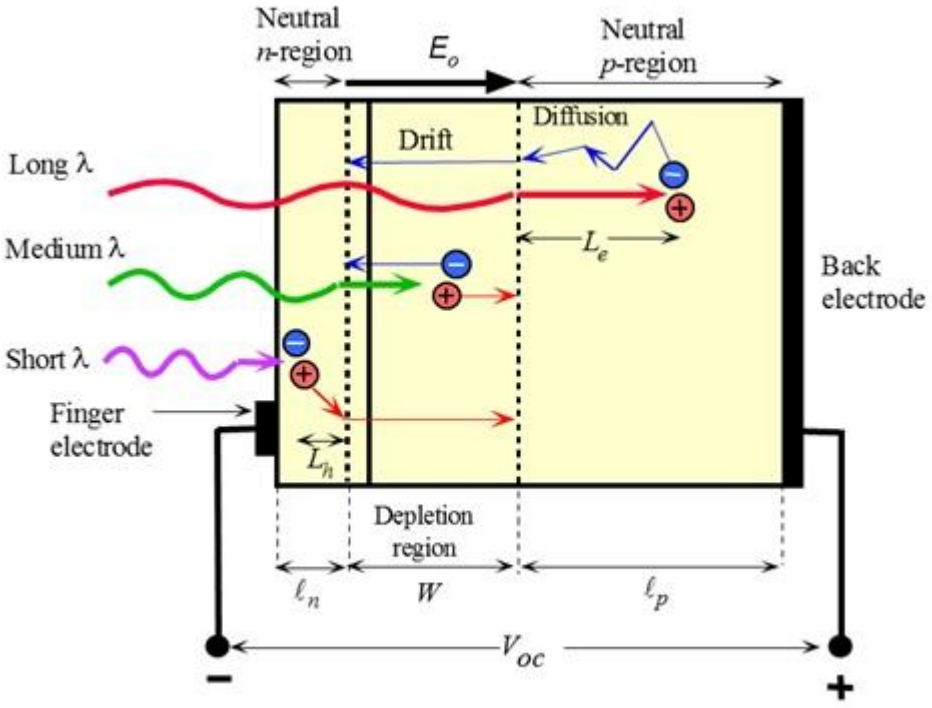

Figure 1.2: The principle of operation of the solar cell.

1.3 WHAT IS PEROVSKITE

The term perovskite refers to the crystal structure of calcium titanate ($CaTiO_3$), which was discovered by the German mineralogist Gustav Rose in 1839 and named in honor of the Russian mineralogist Lev Perovski. In the field of optoelectronics, organometal halide perovskites (OMHPs) are a group of materials with the formula ABX_3, where A is an organic cation ($CH_3NH_3^+$ or $NH_2CH_3NH_2^+$), B is a divalent metal cation (Pb^{2+} or Sn^{2+}), and X is a monovalent halide anion (I−, Br−, or Cl−). Figure 1.3 shows the crystal structure and a single crystal of $MAPbI_3$. In a unit cell of the OHMP structure, eight A cations are located at the vertices of a cubic cage, an B cation is located at the center of the cube, and the latter species is octahedrally coordinated to six X− species that sit at the cube's faces. The OMHP family of materials were studied in the 1990s due to their excellent optoelectronic properties and potential for solution-processed fabrication but the main goal of this early work was to develop new materials for field effect transistors and organic light-emitting diodes [13].

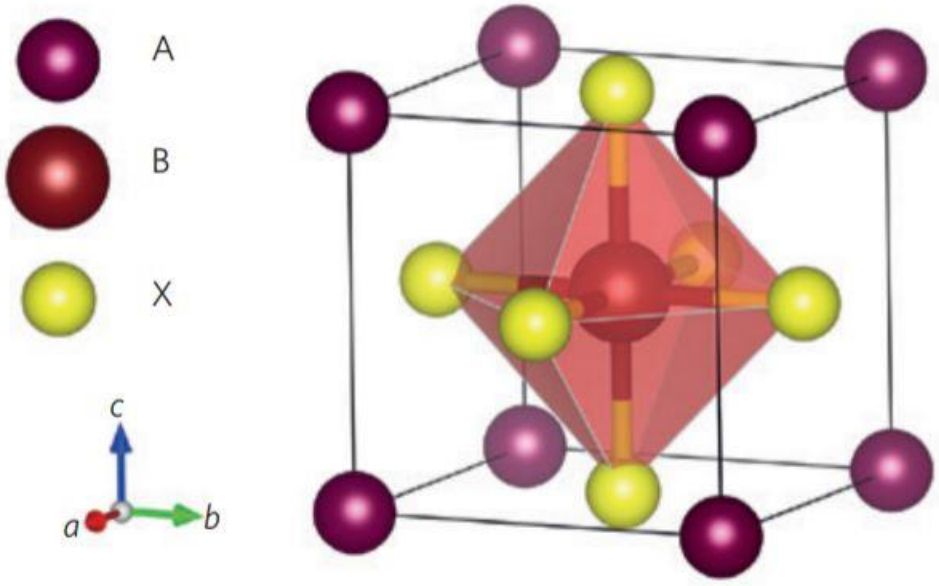

Figure 1.3: Perovskite ABX_3 crystal structure where typically A = $CH_3NH_3^+$, $CH(NH_2)_2^+$, B = Pb^{2+}, Sn^{2+} and X = I^-, Br^-, Cl^-, or mixtures thereof.

1.4 PEROVSKITE CLASSIFICATION

The perovskite system has been classified into two broad categories, which are inorganic oxide perovskite system and halide perovskite system (Fig 1.4). PSC can be produced by methylammonium oxide which has the high open-circuit voltage and the thickness range of the material can be well absorbed with the carrier-based diffusion length. The inorganic perovskite system can be further classified into intrinsic and doped perovskite system. The power conversion efficiency of the intrinsic perovskite system is high when compared to other systems. Because of the high-conversion efficiency the stability of the material is very high and long lifetime of more than 72 hours. The properties of PSC will depend upon the crystal structure of perovskite compound. Therefore doping the perovskite by using lead or halide will increase the power conversion efficiency, stability, and also increase the diffusion length of ions. Therefore the wavelength absorption limit of the compound was improved. Halide perovskite material is one of the key factors in the area of heterostructure-based optoelectronics and microelectronics. This type of material will provide a very high performance with low cost. Halide perovskite system can be further divided into alkali halide perovskite and organometal perovskite system. Alkali halide perovskite has low energy loss, which will lead to increase in power conversion efficiency and high open circuit for improved response. Alkali halide perovskite cell provides wider bandgap, which will provide cost-effective solution for the modules that have high efficiency. Organometal PSC is one of the innovative technology developed in recent years because of its light absorption coefficient and direct bandgap, which will increase the carrier mobility and power conversion efficiency of the system [14].

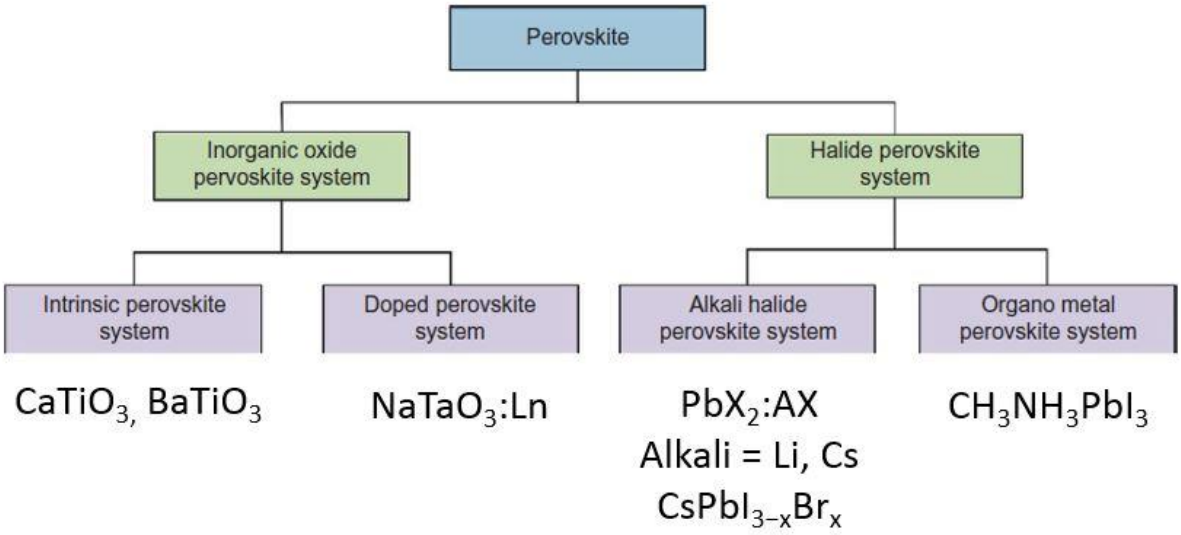

Figure 1.4: Classification of perovskite.

1.5 ORGANIC METAL PEROVSKITE STRUCTURE

Hybrid organic-inorganic metal halide perovskites (metal halide perovskites) represent a class of materials with the stoichiometry ABX_3, whereas A, B and X denote an organic cation with the charge +1, for example, $CH3NH3^+$ (methyl amine), an inorganic cation with the charge +2, for example, Pb^{2+}, and an halide ion with the charge -1, i.e. I-, Br- or Cl-, respectively. The valence and conduction bands of metal halide perovskites are formed by states in the BX_6 octahedra which share the X- corners with neighbored octahedra in perovskite crystals. The structure of the perovskite crystal and the charge are balanced by the organic cations. The bonding in a PbX_3^- anionic framework is mixed ionic/covalent interactions (heteropolar). In the case of organo lead halide perovskite, the composition of $CH_3NH_3PbI_3$ perovskites shows that the formal oxidation state of Pb (+2) and I (-1) are a good estimation of the chemical specie. However, the quantification of partial charge is ill defined due to the collective nature of the periodic electronic wave function. The value of born effective charge of Pb can exceed four in the organo lead halide perovskites due to high ionicity. In $CH_3NH_3PbI_3$ perovskites, lead has

sp^3d^2 hybridization with octahedral framework involving $6s^2$ $6p^o$ $5d^o$ orbitals of lead and $5p^6$ orbitals of iodide ions forming the electronic band structure. The upper valence bond is formed by 5p orbital of iodine and 6s and 6p orbitals of lead form the lower conduction band [15].

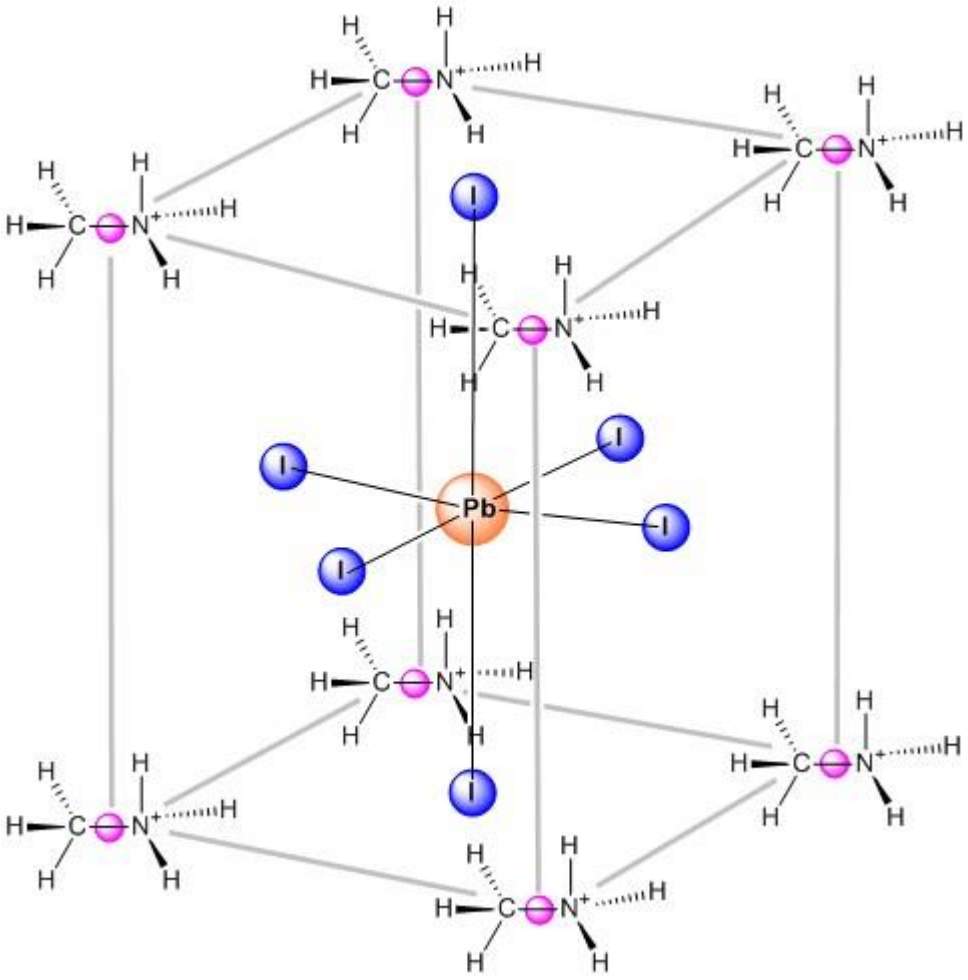

Figure 1.5: Methylammonium cation ($CH_3NH_3^+$) is surrounded by PbX_6 octahedral.

1.6 WHY PEROVSKITE

Perovskites have pulled in a large amount of consideration for PV devices attributable to having a high light absorption coefficient and high carrier mobility. Also the perovskite components can be blended from reasonable sources, demonstrating high performance and cheap solar cells are attainable. Its high charge carrier mobility (2 – 66 $cm^2\ V^{-1}\ s^{-1}$). High quality films have high diffusion length of 0.1–1.9μm, low trap state density ~1010 cm^{-3}, and a carrier lifetime of ~270 ns which coupled with their low binding energy ≤5meV makes them an ideal candidate for solar cells [16].

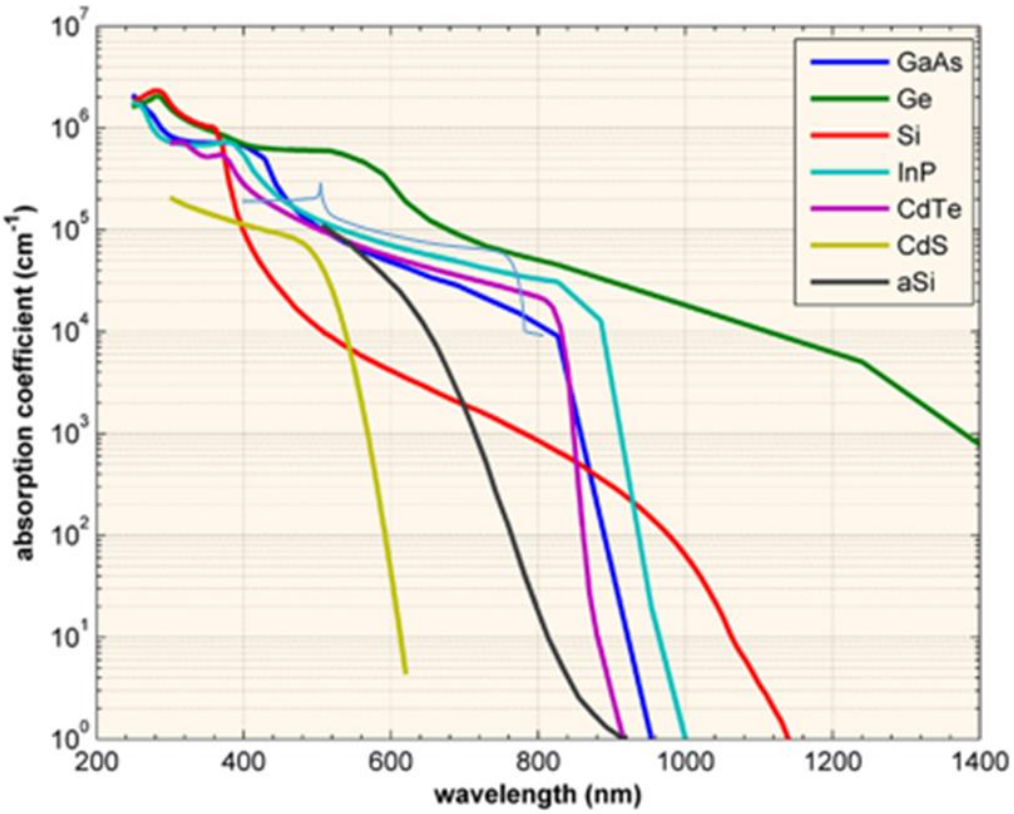

Figure 1.6: The absorption coefficient, α, in a variety of semiconductor materials at 300K as a function of the vacuum wavelength of light.

Band gap has vital importance in photovoltaic related applications. Hybrid 3D perovskites have direct band gap low band gap such as $CH_3NH_3PbI_3$ is a strong absorbance in the visible region and has high absorbance coefficients shows band gap of about 1.55 eV. The band

gap in hybrid perovskites can be tuned by tuning the geometry of perovskites. The tuning of geometry can be done by changing temperature and substituting A, B, and X components of perovskite. The band gap of $CH_3NH_3PbI_3$ hybrid perovskites decreases from 1.61 eV to 1.55 eV with decrease in temperature from 300 K to 150 K.

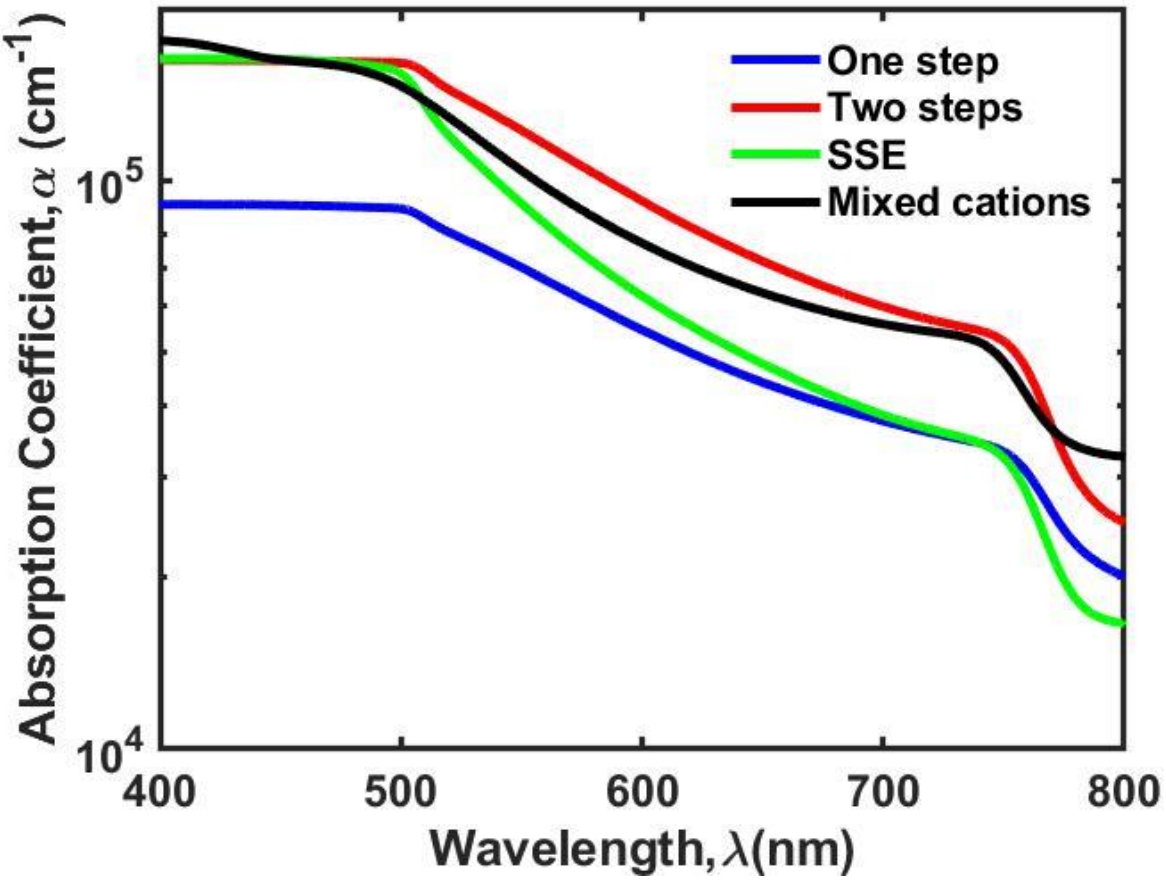

Figure 1.7: Absorption coefficient Vs Wavelength for various perovskite deposition techniques

In the perovskites of stoichiometry, I-II-VII, the substitution of A site organic cations does not directly affect the electronic structure of organic-inorganic perovskites, in fact it changes the crystal geometry. The organic cations regulate the band gap by changing the bond distance between metal and halide. The smaller molecular cation decreases the band gap. For $CH_3NH_3PbI_3$ the band gap is 1.55 eV, for $CH_3NH_3^+$ cation whereas band gap reduces to 0.3 eV when $CH_3NH_3^+$ is replaced by NH_4^+ cation in the perovskites. Similarly, the band gap of $HPbI_3$

less than 0.3 eV due to the smallest cation (H^+). However, too small A site in perovskites leads to instability by tilting of octahedral networks which can change the electronic properties. The NH_4^+ and H^+ cations from the layered perovskites due to small size to fit in the perovskites inorganic networks and produces the deformation in geometry and reduces the band gap. The shape of A site cations also deforms the geometry and help in tuning the band gap of perovskites. The formamidinium are asymmetric molecular ions, produces the distortion of geometry, and provides a fundamental reason for band gap tuning. On the other hand, large A sized cations also forms layered perovskites (2D,D) with high band gap as compared to 3D perovskites. Based on above discussion, it can be concluded that size and shape of A site organic cations tunes the band gap of hybrid perovskites.

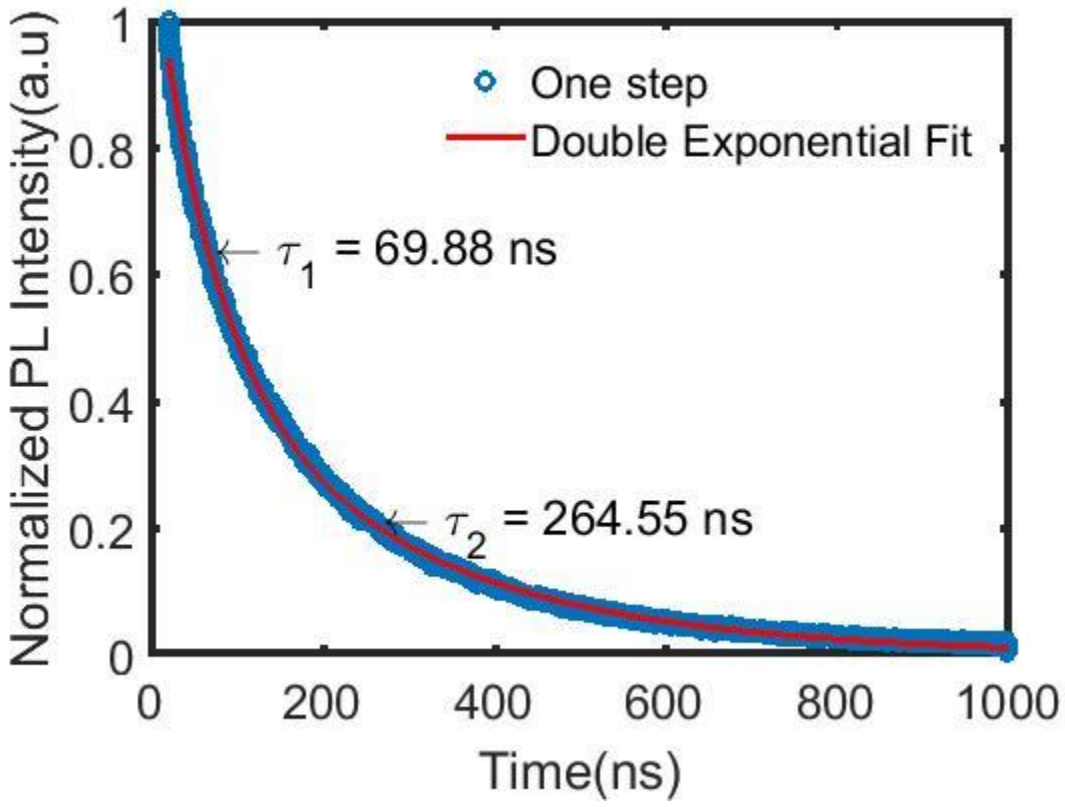

Figure 1.8: Time-Resolved Photoluminescence (TRPL) shows long carrier lifetime for perovskite.

On the other hand, B site metal cations in the perovskite directly amend the conduction band. Therefore, it has been observed that the band gap of the perovskites increases when metal on the B site of perovskite lies higher in group of periodic table. It has been reported that the replacement of lead (Pb) in MAPbI3 by an isovalent tin (Sn) shows increase in band gap from 1.55 eV to 1.7 eV. Similarly, germanium can also be substituted but these metals (Sn, Gn, etc.) oxidized to IV oxidation state and leads to instability in octahedral framework.

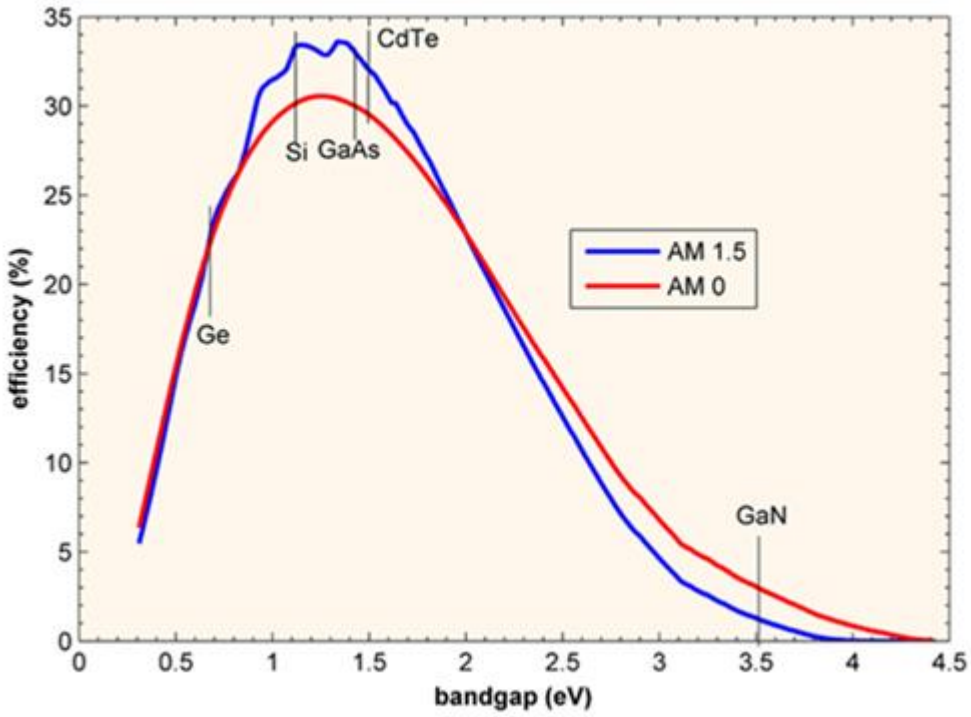

Figure 1.9: Limiting solar cell efficiency as a function of the material bandgap for one-sun illumination.

However, in the hybrid halide perovskites, the mixed isovalent metal halide hybrid perovskites have been reported with band gap low as compared to singe metal halide hybrid perovskites. For $CH3NH3Sn_{1-x}Pb_xI_3$ where x = 0 to 1, the band gap reaches to 1.18 eV, depending upon the composition of perovskites. The anions (X sites) in the organic-inorganic perovskites are more effective candidates that control the band gap. The substitution of halide ions produces more shifts in the band gap of perovskites as compared to the substitution of

organic cations. The change in band gap is related to the electronic state of anions, the valence band composition changes from 3p to 4p to 5p for Cl, Br, and I, respectively. Therefore, electron binding energies decreases from Cl to I. In $CH_3NH_3PbX_3$, the change in X site from I to Cl varying the band gap from 1.55 eV to 3.0 eV. The mixed halide-based hybrid perovskites are the potential candidates for band gap tuning. Changing the I-Br ratio tune the band gap with increasing thermal stability because of their comparable ionic sizes. On the other hand, the change in I-Cl ratio in perovskites does not produces significant change in band gap due to large difference in size ratio.

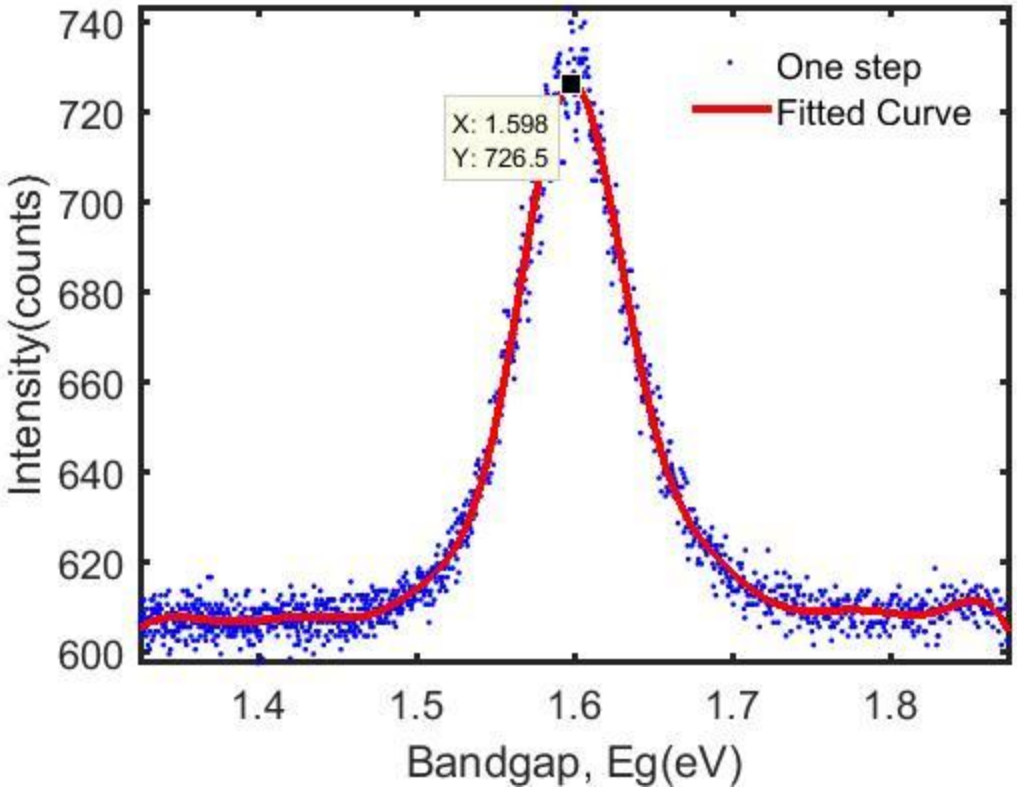

Figure 1.10: Photoluminescence (PL) shows 1.6eV bandgap for one step deposition

1.7 PEROVSKITE PHOTOVOLTAIC TECHNOLOGY

The most preferred technology in PV market is the wafer-based technology and more than 85% of the world PV market uses this type of cells. Crystalline silicon is one of the forms of wafer-based technology. Crystalline silicon is also called as the first-generation PV technology where the wafer-based crystalline silicon is used as the active material. Crystalline silicon is further classified into monocrystalline and polycrystalline silicon. The theoretical efficiency of single-junction solar cells are of 27% and around 25% of practical efficiency has been achieved. The crystal structure of monocrystalline silicon is homogenous, which means the lattice parameter, electronic properties, and the orientation remains constant throughout the process. To improve the power conversion efficiency crystal structure solar cell has been used in this technology. Monocrystalline silicon requires more expensive wafers compared to other technologies and also able to produce more energy. This type of silicon is used in rooftop and space applications. Polycrystalline silicon is composed of a number of small crystals of lowgrade silicon, which results in low cost and efficiency when compared to monocrystalline silicon. Polycrystalline silicon is the key technology for the manufacture of conventional silicon-based solar cells. More than half of the global supply of PV technology has been done through polycrystalline cell in 2006. Thin-film solar cell comes under the category of the second-generation solar cell, which can be formed by combining one or more layers of plastic, glass, or metal. It is the most used technology for commercial applications throughout the world. Thin-film solar cells are always very cheap compared to silicon solar cells and the efficiency is also very less but significant research has been carried out over the years to improve the performance of the thin-film solar cells.

The amount of active material used in thin-film technology is very less compared to silicon. The light absorption capacity of the thin film is 100 times efficient than silicon that allows the material to absorb very few microns of thickness. Copper Indium Gallium Diselenide (CIGS), Cadmium Telluride (CdTe), and amorphous silicon (a-Si) are some of the materials used

in the commercial thin-film technologies. The theoretical efficiency of CdTe is very high among the semiconductors available today for single-junction configuration. CdTe PV technology has installed worldwide capacity of 15 GW because of its thermal and chemical stability results in the enormous increase of efficiency compared to other technologies. It is ideally suited for utility-scale applications to reduce the cost of electricity per watt. Similar to CdTe, Cadmium Indium Diselenide (CIS) also has very high absorption coefficient and high efficiency because of its wide spectrum and the cost of CIS PV technology is very low compared to other technologies. The power conversion efficiency of CIS has already crossed over 20%. CIS PV technology is ideally suited for building integrated PV applications because of their flexible property and lightweight.

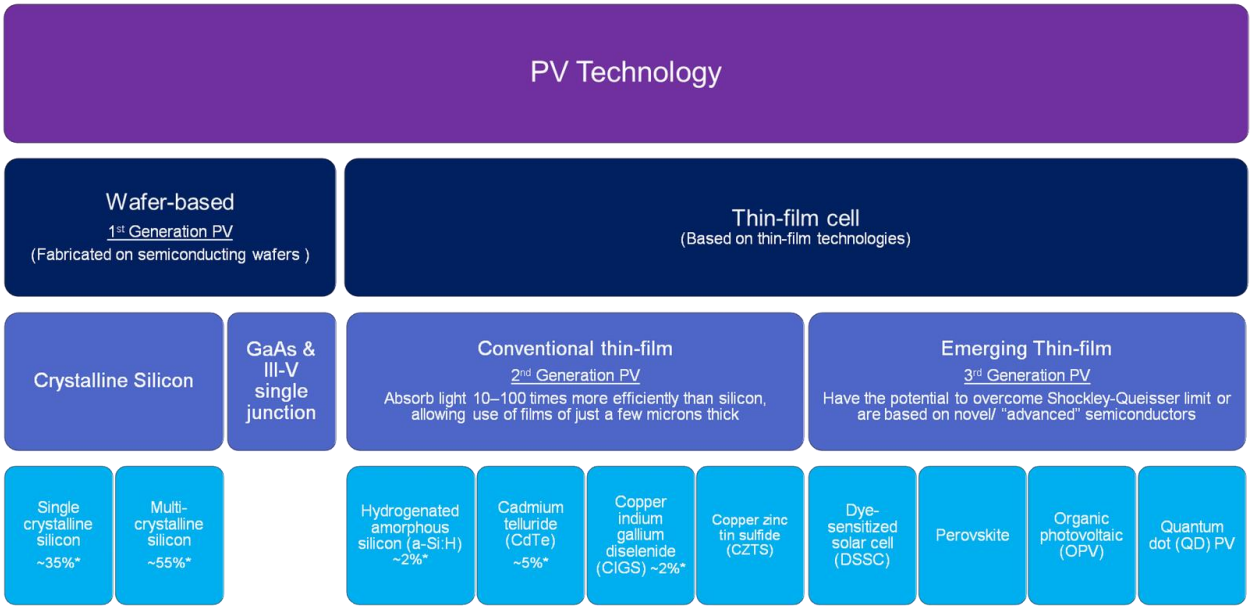

Figure 1.11: Classification of photovoltaic technology.

Emerging thin-film generation comes under the category of third generation solar cells most of the materials in this category have not yet been commercially applied and most of the materials are still in research or under development phase. In emerging thin-film technologies the production process of solar cell has been carried out through different steps namely active

material synthesis and deposition. But in conventional thin-film technology all the process has been done in a single step. Therefore emerging thin-film solar cells used in flexible applications and lightweight materials. This technology includes Quantum Dot, Dye Sensitized, Organic PV, and perovskite. For the design of quantum dot solar cell this technology uses quantum dot for the absorption of PV material. Therefore the materials like silicon, CdTe, CIS can be replaced by quantum dot and it has a high bandgap that is used to tune different range of energy levels. Even though the efficiency of the quantum dot as low as 9% it has attracted the researchers because of its versatile property, low cost, and lightweight. Dye-sensitized solar cell (DSSC) is produced based on the semiconductor formed between the electrolyte, photosensitized anode and a photo electrochemical system. Even though the theoretical power conversion efficiency of DSSC is very less due to its performance ratio and price it can be used as a viable option for an electric generator for grid integration. The stability of DSSC under illumination is limited and the absorption coefficient is low in the infrared region are the key challenges in this technology.

Organic solar cell uses organic polymers to absorb light and transport the charge into electricity from sunlight through PV effect. The production cost of an organic solar cell is low because the molecules that are used in this process are very cheap. The main drawbacks of the organic solar cells are low stability, low efficiency, and low strength when compared to silicon cells. Perovskite solar cell (PSC) includes the perovskite-structured material as an active layer based on the solution processed by tin or halide. It is a very attractive option for commercial applications because this type of cells is very cheap during the scale-up process. Perovskite solar cell has emerged as one of the most standout cell in terms of efficiency. Therefore the researchers have shown tremendous interest in Perovskite solar cell. Flexibility, lightweight, and semitransparency are some of the valuable proportion of perovskite.

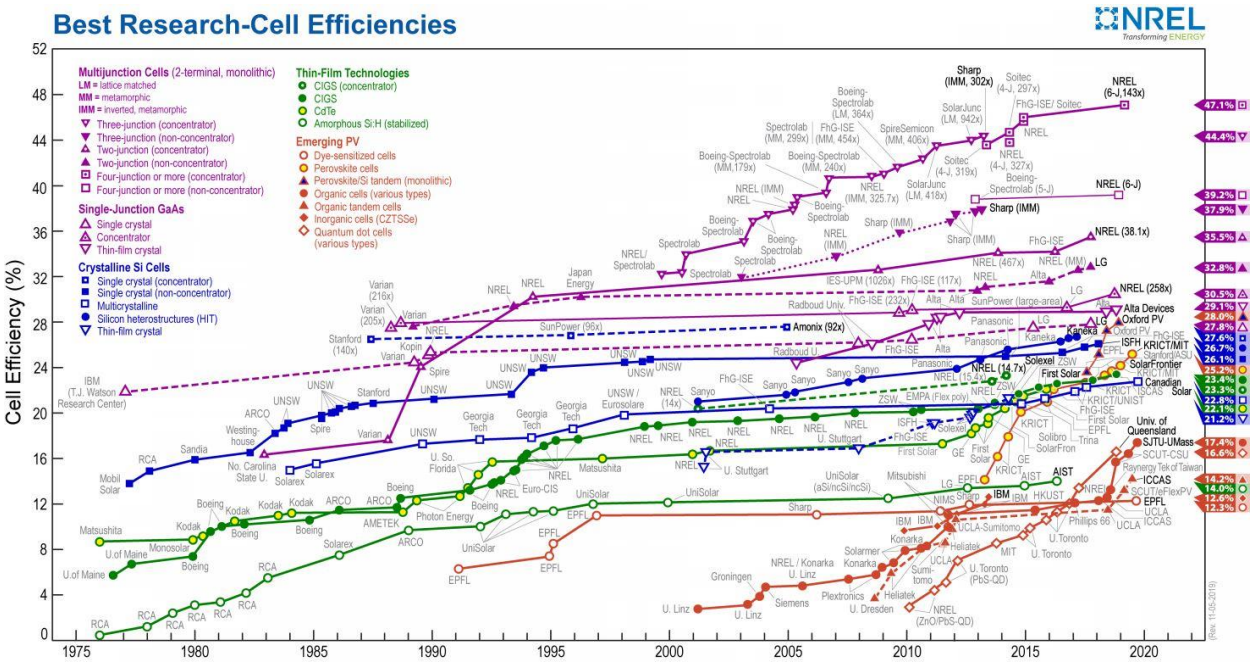

Figure 1.12: Best Research-Cell Efficiency Chart

1.8 STATE OF ART

Organometal halide perovskites were first used as a light absorbing material in dye-sensitized solar cells (DSSCs) in 2009. Miyasaka et al. prepared $CH_3NH_3PbI_3$ ($MAPbI_3$) and $CH_3NH_3PbBr_3$ ($MAPbBr_3$) perovskite-based DSSCs and reported power conversion efficiencies (PCEs) of 3.8% and 3.1%, respectively [5]. In 2011, the PCE of $MAPbI_3$ was increased considerably to 6.5% by optimizing a thinner TiO2 film as well as the perovskite precursor solution and electrolyte composition [17]. In 2012, liquid electrolyte was replaced with 2,2',7,7' tetrakis (N,N-p-dimethoxy-phenylamino)-9,9'-spirobifluorene (spiro-MeOTAD) as a hole-transport material [18,19]. Park et al. proposed an architecture that resembles a solid-state DSSC in which the $MAPbI_3$ nanocrystals are deposited on mesoporous TiO_2 (mp-TiO_2) instead of the dye. The $MAPbI_3$-sensitized solid-state solar cell demonstrated a PCE of 9.7% based on a 0.6 µm-thick mp-TiO_2 film. The organometal mixed halide of $MAPbI_{3-x}Cl_x$ deposited on the mesoporous Al_2O_3 film formed on a compact TiO_2 (cp-TiO_2) layer has been reported to demonstrate a PCE of 10.9% upon contacting spiro-MeOTAD.

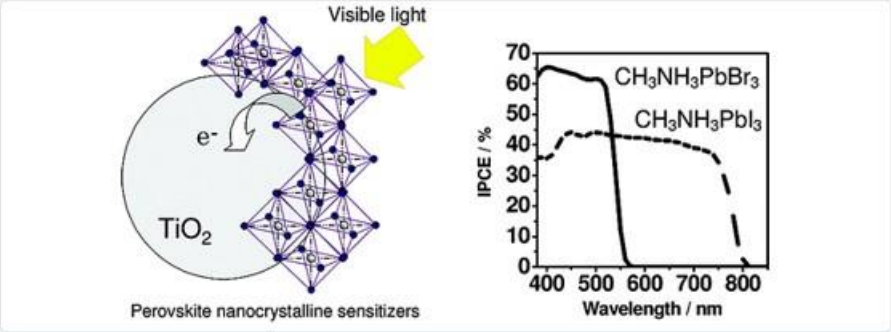

perovskite sensitizer on TiO_2	J_{sc} (mA/cm^2)	V_{oc} (V)	FF	η (%)
$CH_3NH_3PbBr_3$	5.57	0.96	0.59	3.13
$CH_3NH_3PbI_3$	11.0	0.61	0.57	3.81

Figure 1.13: Photovoltaic Characteristics of Perovskite-Based Cells

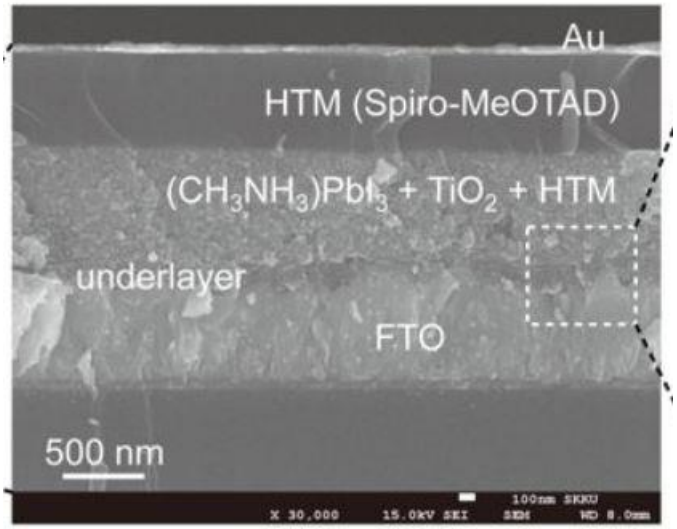

Figure 1.14: Cross-sectional SEM image of the device

However, such mesoporous devices require high-temperature sintering that could increase the processing time and cost of cell production. Methylammonium-based perovskites have been found to have long charge-carrier diffusion lengths (100 nm for $CH_3NH_3PbI_3$ and 1000 nm for $CH_3NH_3PbI_{3-x}Cl_x$) [20, 21]. Further studies demonstrated that perovskites exhibit

ambipolar behavior, indicating that the perovskite materials themselves can transport both electrons and holes between the cell terminals. All these results indicate that a simple planar structure is feasible, and the first successful demonstration of a planar structure was the perovskite/fullerene structure reported by Jeng, [22] showing a 3.9% efficiency. Eperon et al. [23] then optimized the film formation of the $CH3NH3PbI_{3-x}Cl_x$ perovskite by controlling the atmosphere and annealing temperature, and they achieved a PCE of 11.4% with J_{sc} 20.3mA/cm2 and V_{oc} 0.89V. The breakthrough of the planar perovskite structure was achieved using a dual-source vapor deposition that achieved an efficiency [24] of 15.4% with V_{oc} 1.07V. Yang's group pushed the efficiency of the planar structure to over 19% through interface engineering and by controlling the morphology of the perovskite film [25].

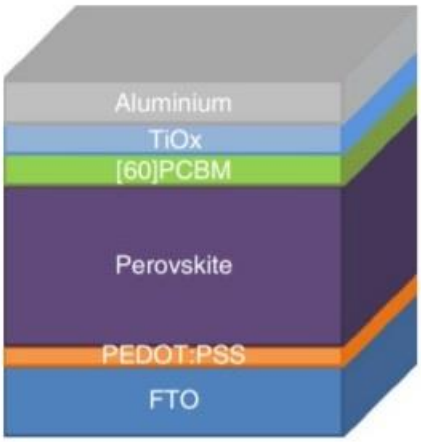

Figure 1.15: Inverted planar-heterojunction perovskite device.

Anaraki et al. proposed a solution-processed technological approach for depositing SnO_2 layers and achieved V_{oc} 1214mV at a bandgap of 1.62 eV and a PCE of 20.7% [26]. A high quality perovskite film is essential for determining the photovoltaic (PV) performance and reproducibility of a perovskite solar cell (PSC). Besides the excellent PV performance of organometal halide perovskites, the latter is also attractive because of its versatility in fabrication techniques. Numerous deposition techniques have been developed for fabricating uniform and dense perovskite layers for planar configurations.

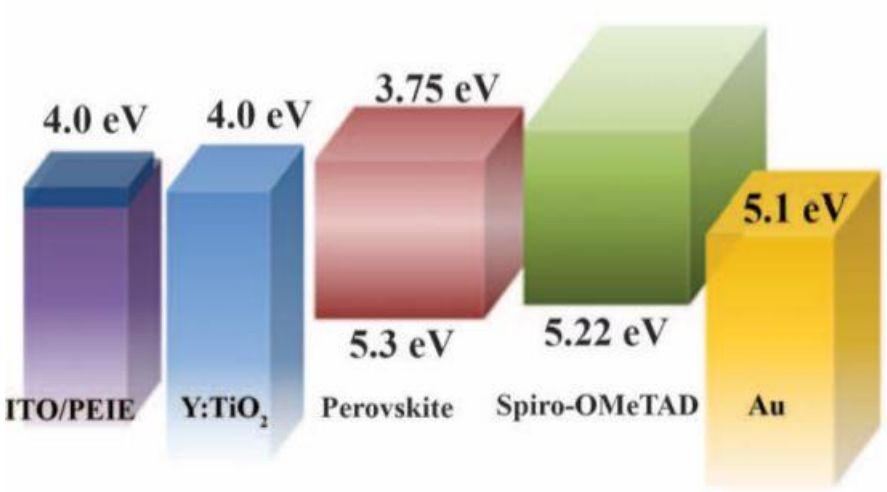

Figure 1.16: Diagram of energy levels (relative to the vacuum level) of each functional layer in the device.

The most popular thin-film deposition method for PSCs is one-step deposition because of its obvious simplicity. Kim et al. reported on solid-state mesoscopic heterojunction solar cells; using nanoparticles of methyl ammonium lead iodide as light harvesters, they generated large photocurrents (J_{sc}) exceeding 17mA/cm^2, an open-circuit photovoltage (V_{oc}) of 0.888V, and a fill factor (FF) of 0.62, thereby yielding a PCE of 9.7%.3 Wojciechowski et al. optimized the formulation and demonstrated an efficiency of 15.9% in a solar cell processed at low temperature [27]. A room-temperature solvent-to-solvent extraction (SSE) concept was developed for depositing hybrid perovskite thin films over large areas. Instead of adding the antisolvent during spin coating, the coated substrate using a novel perovskite precursor solution is immersed immediately in a bath of antipolar solvent (e.g., diethyl ether) at room temperature. Zhou et al. reported that planar PSCs based on the SSE method delivered PCEs up to 15.2% and most notably an average PCE of 10.1% for PSCs with sub-100 nm semitransparent perovskite thin films [28]. Nie et al. proposed a solution-based hot-casting technique for growing continuous pinhole-free thin films of organometallic perovskites with millimeterscale crystalline grains with almost 18% efficiency for the planar configuration [29]. Compositional engineering has been demonstrated to reduce the material photoinstability [30] and shows that incorporating $MAPbBr_3$ into $FAPbI_3$ stabilizes the perovskite phase of $FAPbI_3$ and improves the PCE of the solar cell

[31]. The effects of moisture and other factors on the stability of PSCs are reduced by partial substitution of I with Br ions [32]. Anaraki et al. proposed a solution-processed technological approach for depositing SnO_2 layers and achieved an efficiency of 20.7%. The FA/MA-Cs mixed cation perovskite had been used for the absorber layer.

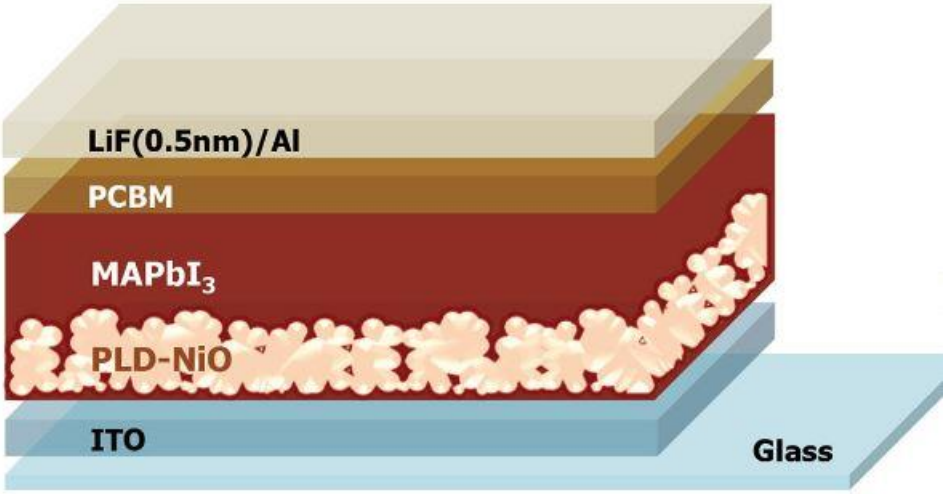

Figure 1.17: Diagram of the device configuration.

1.9 MOTIVATION AND STRATEGIES

Film crystallography, morphology, stoichiometry, and degradation are influenced by the deposition techniques, and each technique requires its own settings for film optimization. The main motivation of the present work is to investigate material characterizations among various deposition techniques based on only one solvent N, N-dimethylformamide (DMF) so that characterization results can be compared. Investigations by XPS, X-ray diffraction (XRD), and scanning electron microscopy (SEM) have been undertaken to better understand the oxidation of core elements of perovskites, film crystallography, morphology, and stoichiometry when using different deposition techniques of perovskites. Time resolved photoluminescence (TRPL) and photoluminescence (PL) allow us to clearly interpret the lifetime and the bandgap of perovskite material. UV-Vis spectrophotometer results help us to investigate the influence of various

deposition techniques on optoelectronic properties of perovskite. In the present work, four different deposition techniques—(i) one-step deposition, (ii) two steps deposition, (iii) room-temperature solvent-to-solvent extraction (SSE), and (iv) solution processing using FA/MA mixed cations—are considered. Besides, planar heterojunction PSCs are fabricated by using the best deposition technique based on the results of XPS, XRD, and SEM. To optimize the electron-transport layer, we investigate systematically how the thickness of the compact TiO_2 layer affects the device performance by using different spin speeds to fabricate this layer. In addition, we compare the device performance between the well-studied TiO_2 and low-temperature solution-processed nanocrystalline SnO_2 as the electron-transport layer.

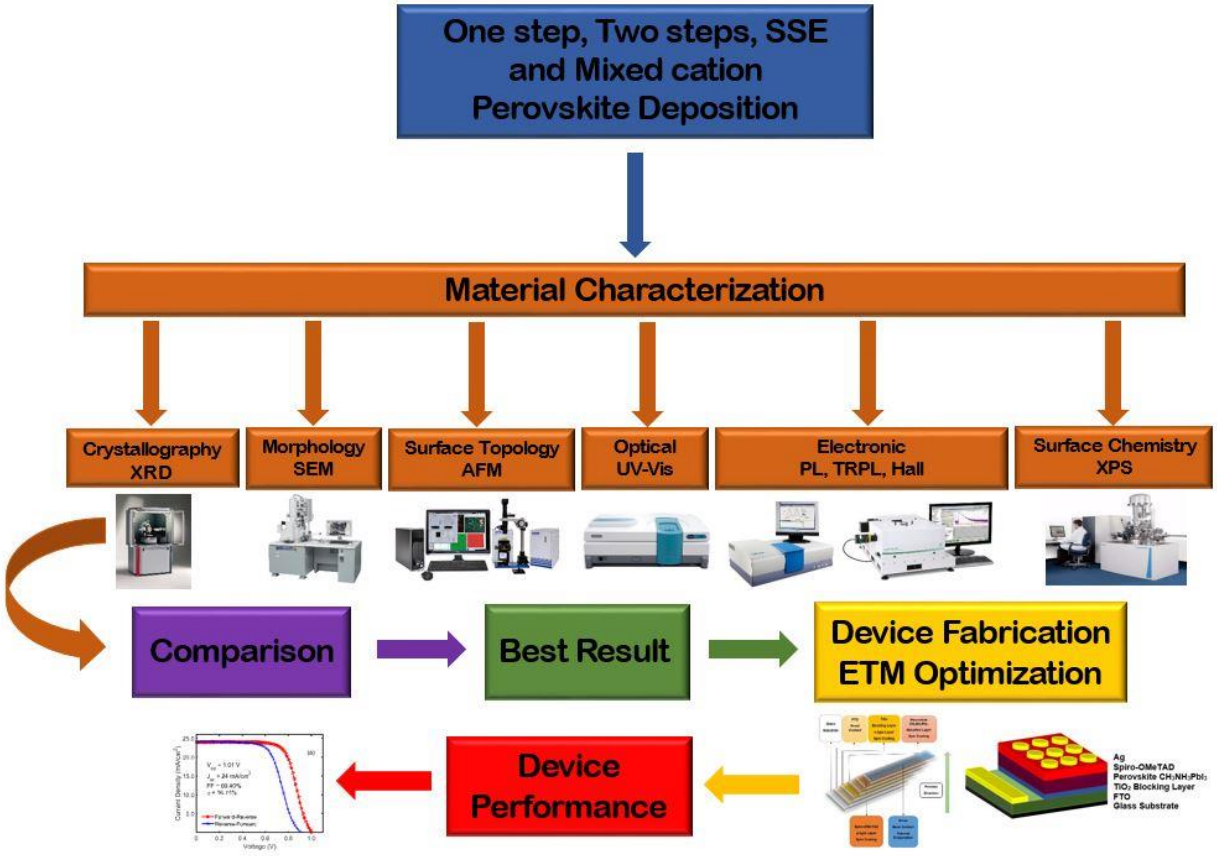

Figure 1.18: Research flow chart.

Chapter 2: Experimental Methods

2.1 INTRODUCTION

FTO-coated glass substrates with a sheet resistance of 7 Ω/sq were obtained from Sigma-Aldrich. All solutes for perovskites such as PbI_2 (beads, 10 mesh, 99.999% trace metal basis), $PbBr_2$ (99.999% trace metal basis), formamidinium iodide (FAI) (98%, H-NMR), methylammonium bromide (MABr) (98%), and methylammonium iodide (MAI) (98%) were purchased from Sigma-Aldrich. N,N-dimethylformamide (DMF) (anhydrous, 99.8%), dimethyl sulfoxide (DMSO)(anhydrous, 99.9%), and diethyl ether were purchased from Sigma-Aldrich. The main material for the TiO_2 layer is Ti-nanoxide (BL/SC). It was purchased from Solaronix. All necessary materials for the SnO_2 layer [Tin (II) chloride dehydrate ((99.995% trace metal basis), Tin (IV) chloride pentahydrate (98%), isopropyl alcohol, urea, and mercaptoacetic acid ((99%)] were purchased from Sigma-Aldrich except HCL. HCL (37wt%) was obtained from Fisher Scientific. Spiro-MeOTAD (99%,HPLC), chlorobenzene (anhydrous, 99.8%), bis(trifluoromethylsulfonyl)imide lithium salt (Li-TFSI), acetonitrile (anhydrous,99.8%), 4-tert-butylpyridine (TBP), and tris(2-(1H-pyrazol-1-yl)-4-tert-butylpyridine)-cobalt(III)tris(bis(trifluoro methylsulfonyl)imide) (FK 209 Co(III)TFSI salt) were purchased from Sigma-Aldrich. The thermal evaporation material, silver (Ag) pellets, was purchased from Kurt J. Lesker Co.

2.2 ONE STEP DEPOSITION

$CH_3NH_3PbI_3$ can be fabricated by mixing two compounds (PbI_2, CH_3NH_3I). CH_3NH_3I was synthesized by mixing Methylamine (27.86 ml, 40% in methanol) and hydroiodic acid (30 ml, 57 wt.% in water) at 0°C and stirred for 2 h. The precipitate was recovered by evaporation at 50°C for 1 h. The product was washed with diethyl ether three times and then finally dried at 60°C in vacuum oven for 24 h.

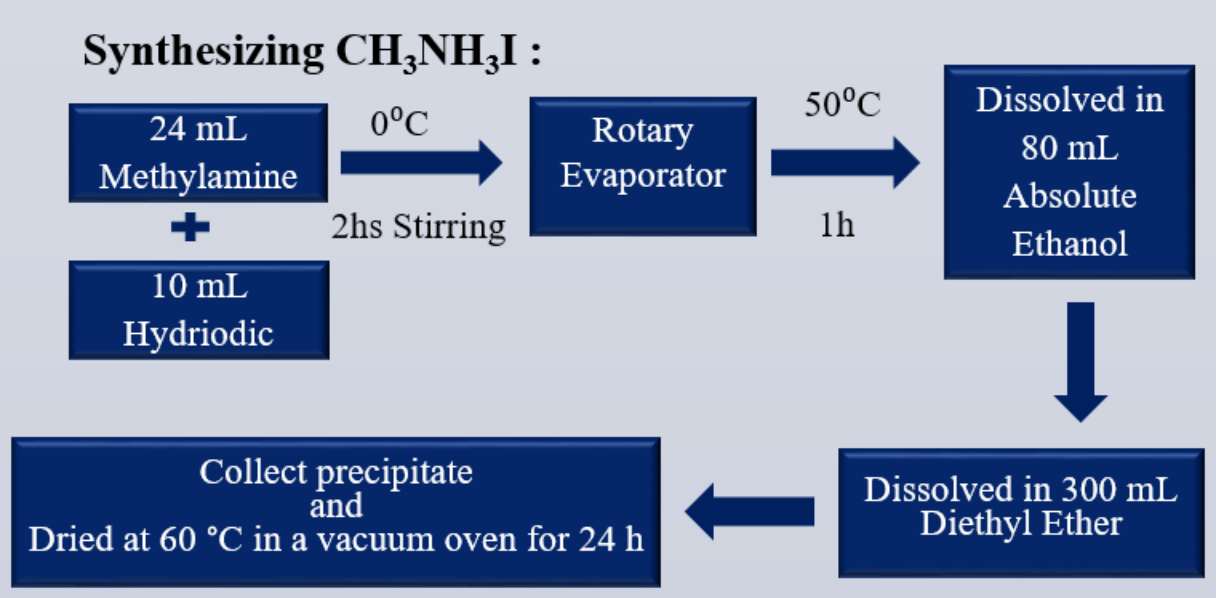

Figure 2.1: Flow chart of synthesizing MAI.

To prepare the perovskite, we mixed CH_3NH_3I (0.395g) and PbI_2 (1.157 g) in DMF at 60°C. The perovskite film was formed by spin coating at 3000 rpm for 30 s, and the coated layer was heated at 100°C for 1 h [33].

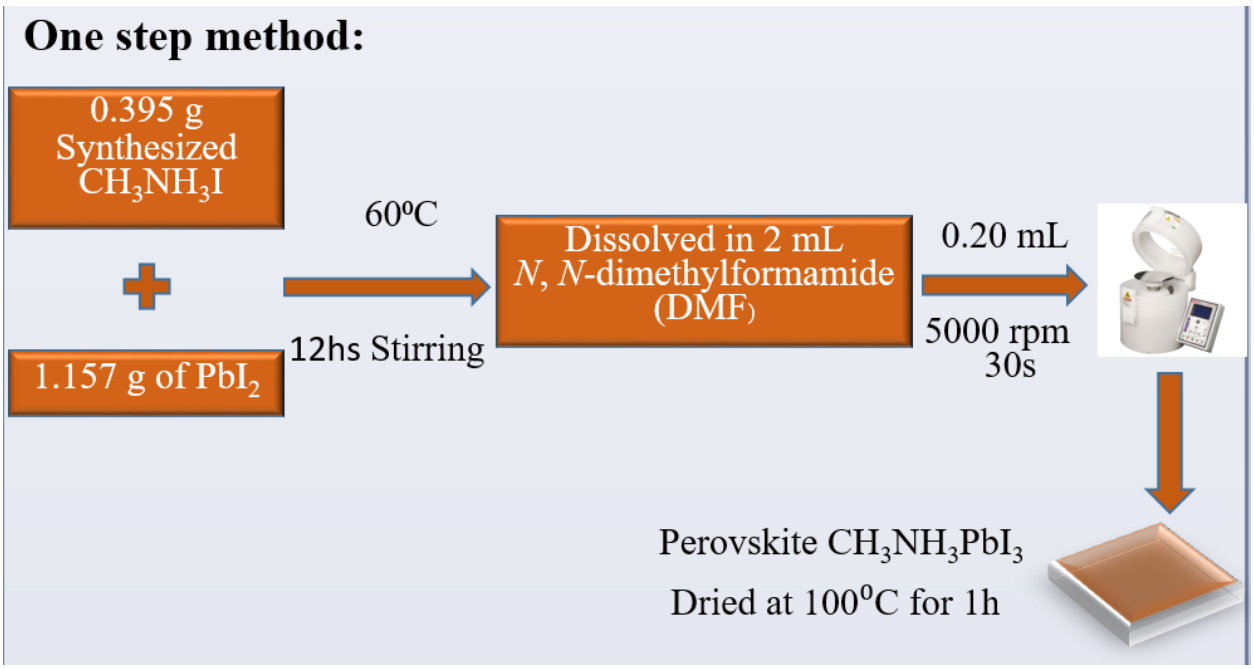

Figure 2.2: Flow chart for one step deposition.

2.3 TWO STEPS DEPOSITION

In 1 ml DMF, 462 mg PbI2 was dissolved at 70ºC to make 1M PbI2 solution. Twenty microliters PbI2 solution was spin coated at 3000 rpm for 20 s, which was dried at 40◦C for 3 min and 100◦C for 5 min consecutively. One hundred microliters of 0.063M CH3NH3I solution in 2-propanol (10 mg/ml) was loaded on the PbI2-coated substrate for 20 s, which was spun at 4000 rpm for 20 s and then dried at 100 ◦C for 5 min [34,35].

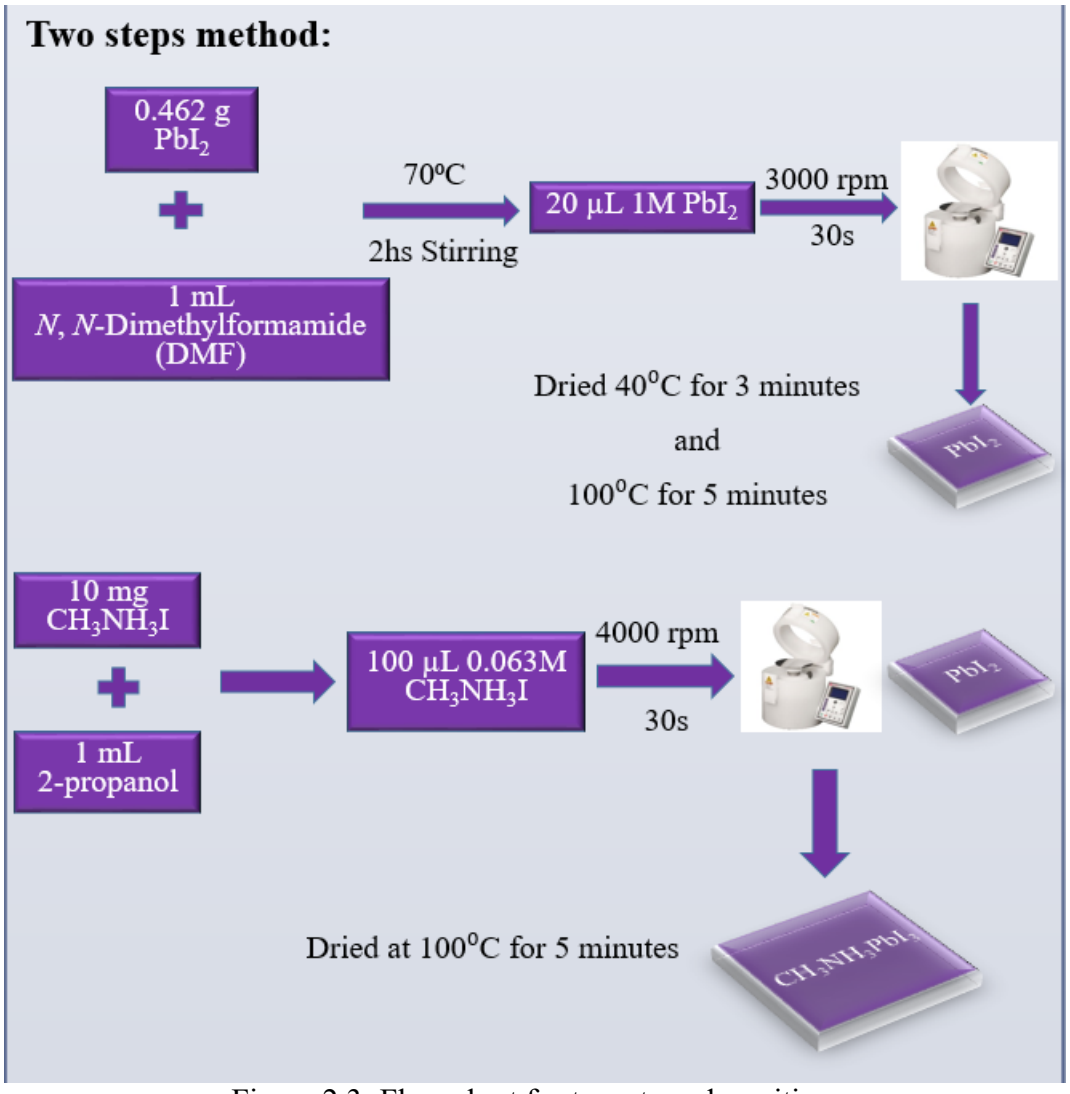

Figure 2.3: Flow chart for two steps deposition.

2.4 SOLVENT TO SOLVENT EXTRACTION

A solution of PbI_2 and MAI (molar ratio 1:1) in DMF was spin coated at 3000 rpm for 30 s, whereupon the solution-coated substrate was dipped immediately in a 50ml anhydrous diethyl ether bath. The substrate was kept immersed until the color of the film changed to brown. The substrate was then taken out of the bath and blow dried rapidly at room temperature using nitrogen gas [28].

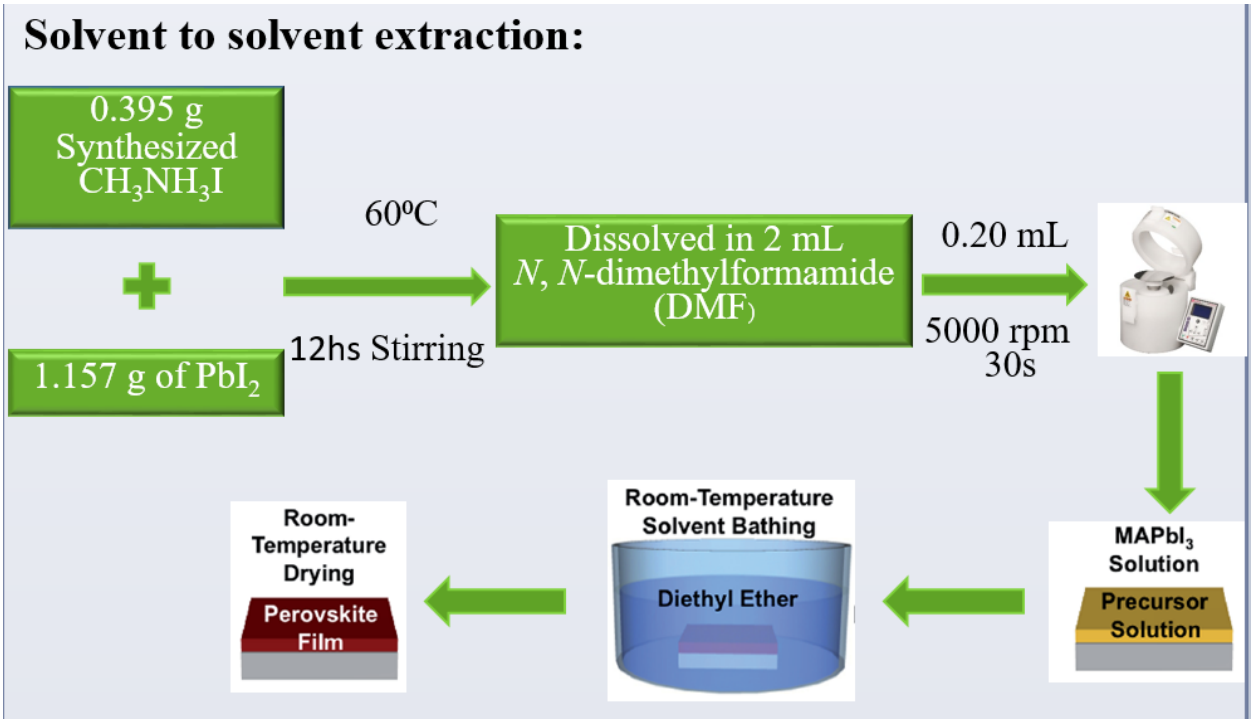

Figure 2.4: Flow chart for solvent to solvent extraction deposition.

2.5 MIXED CATION SOLUTION PROCESSING

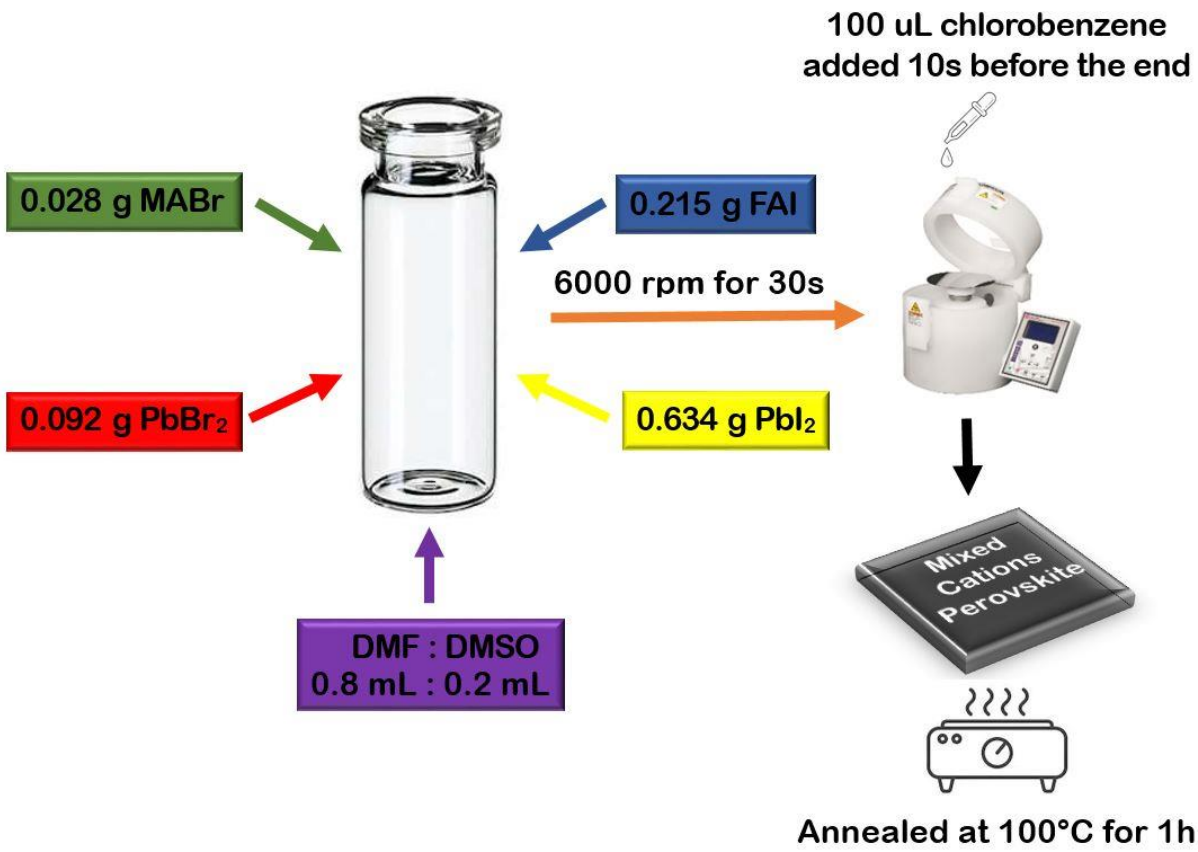

Figure 2.5: Flow chart for mixed cation solution processing.

A mixed-cation perovskite solution was prepared from a precursor solution made of FAI (1 M), PbI_2 (1.1 M), MABr (0.2 M), and $PbBr_2$ (0.2 M) in a 4:1 (v:v) mixture of anhydrous DMF:DMSO. The solution was spin coated at 3000–6000 rpm for 30 s, with chlorobenzene as an antisolvent being added dropwise for 5–10 s before the end. The perovskite layers were annealed at 100°C for 1 h [26].

2.6 SUMMARY

One step deposition is a low cost spin coating technique, easy to process, low temperature required (less than 150°C) to process and it produces bigger crystal grains with appropriate

processing temperatures and solvent. Two steps method has better control over the film morphology and higher reproducibility. SSE avoids the thermal annealing potentially suitable for roll to roll manufacturing. Mixed cation solution processing has relatively high stability with low fabrication cost compared to conventional single phase ABX_3 perovskites, extremely dense perovskite layer and lower band gap.

Chapter 3: Material Characterizations

3.1 Introduction

Elemental analysis, chemical bonding, and identification of the oxidation states were studied by X-ray photoelectron spectroscopy (XPS). Ambient-pressure photoelectron spectroscopy (AP-PES) was used for surface chemical analysis via core-level photoelectron spectroscopy. The photon energy range of the beamline was from 250 eV to 2 keV, covering the O 1s, N 1s, and C 1s core levels as well as many transition-metal core levels. An X-ray diffraction (XRD) diffractometer (D8 Discover; Bruker) with Cu Kα radiation (λ = 1.5406A˚) was used for the XDR study. Also a scanning electron microscope (SEM) (S-4800; Hitachi) was used to study the film morphology. TRPL measurements were conducted by silicon-based photon counting detectors (400-1100nm range) for time-resolved two-color and polarization photoluminescence imaging, and an Acton SP2750-Pixis100 spectrograph-CCD system was used for micro-PL spectroscopy (400-1100nm range). Park NX-20 atomic force microscope was used for surface imaging at ambient conditions at room temperature. It provides capabilities for standard contact and non-contact AFM operation, as well as Lateral Force Microscopy (LFM), Scanning Capacitance Microscopy (SCM), Magnetic Force Microscopy (MFM), Scanning Tunneling Microscopy (STM) and Nanolitography, among others. The absorption profiles are measured by using Cary 5000 UV-Vis Spectrophotometer. Mobility, conductivity were measured by HMS-3000 Hall Measurement System.

3.2 Crystallography: XRD

The XRD results show that the main diffraction peaks of (110), (200), (211), (202), (220), (312), (224) and (314) for perovskite are obtained at diffraction angles of 14.077º, 20.21º, 23.59º, 24.47º, 28.354º, 31.768º, 40.48º, and 43.09º respectively, for all the samples. The two steps deposition and SSE show a diffraction peak of (001) for PbI_2 at a diffraction angle of

12.78°, indicating a secondary phase. One step deposition and mixed cations do not have any secondary phase.

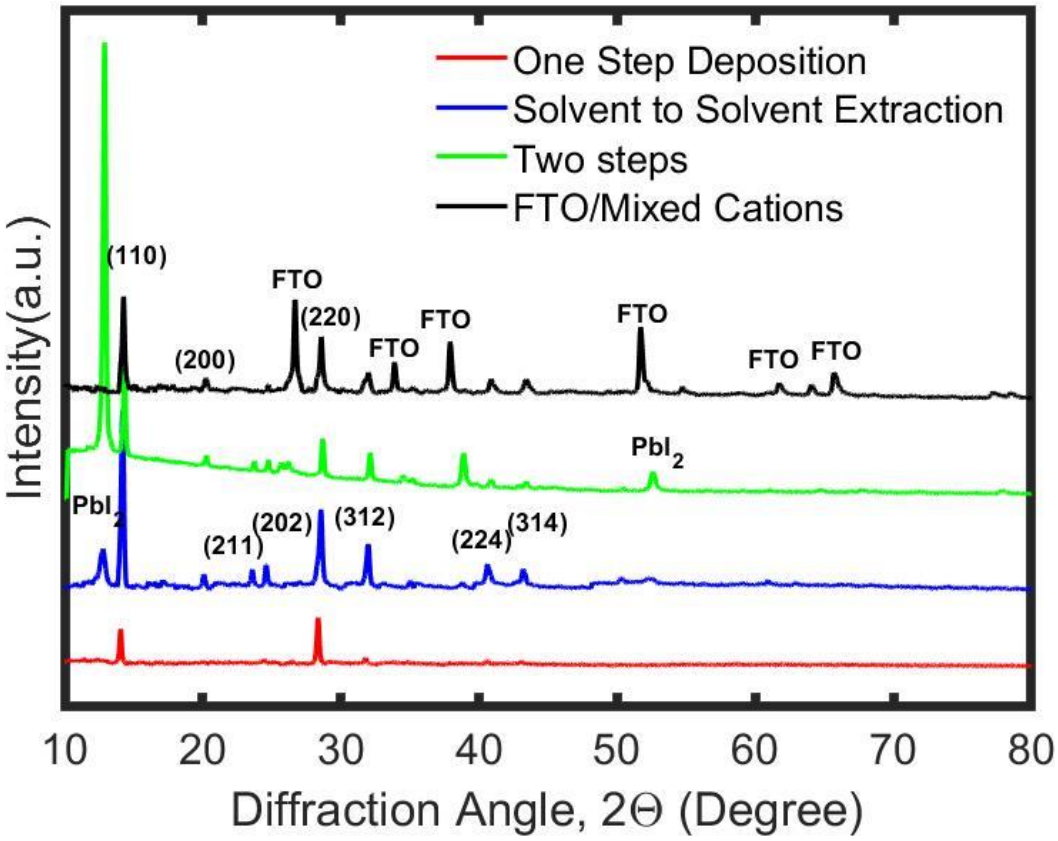

Figure 3.1: XRD profiles of perovskites show the main diffraction peaks.

Crystallite size was calculated by scherrer equation [36]. One step deposition has the highest crystallite size among all samples.

$$Scherrer\ equation, D = \frac{0.9 \times \lambda}{B \times \cos\theta} \tag{3.1}$$

Here,

D = Crystallite size (nm)

λ = The wavelength of the X-ray irradiation (0.154056 nm)

B = The line width at half maximum for (110) (radians)

θ = Diffraction angle (2θ) / 2 (radians)

Table 3.1: Crystallite size of perovskite using the Scherrer equation for the (110) peak, calculated from XRD patterns obtained under ambient conditions.

Methods	Crystallite size, D (nm)
One step	40.02129
Two steps	33.36122
SSE	27.60507
Mixed cations	38.12419

3.3 MORPHOLOGY: SEM

The film morphologies of perovskites are crucial for achieving high-performing devices. This is because pinhole formation and incomplete coverage of perovskites give rise to low-resistance shunting paths and loss of light absorption in the solar cell. We used SEM to analyze the morphologies, pinhole formation, and incomplete coverage of the perovskite films. Figure 3.2 shows that in the one-step deposition, the grains are loosely packed and the perovskite films exhibit pinhole formation and incomplete coverage. By contrast, the two steps deposition, SSE and mixed-cation samples have smaller grains than one step deposition sample and have closely and neatly packed films with minimum pinhole formation and good coverage area.

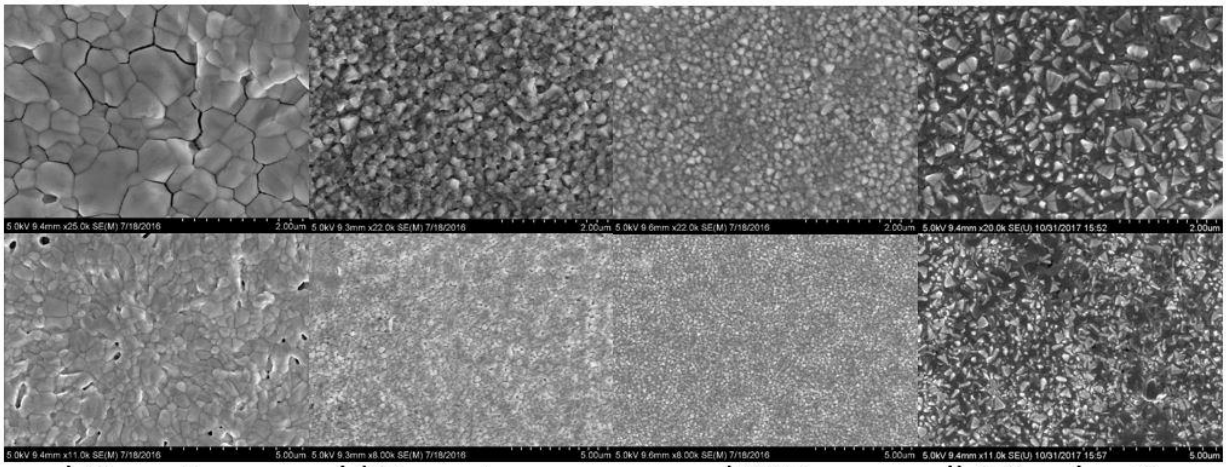

Figure 3.2: Low- and high-magnification SEM micrographs of the top surface of perovskite films deposited on a glass substrate.

Average grain diameters were calculated by using the following equations [37]. Results show one step deposition has the highest average grain diameter.

$$Magnification, M = \frac{Print\ width}{Real\ width} \tag{3.2}$$

$$\#\ of\ grain\ intercepted = Whole\ grains + Partial\ grains \tag{3.3}$$

$$Total\ true\ length = \frac{Length\ of\ lines}{M} \tag{3.4}$$

$$Average\ grain\ diameter = \frac{Total\ true\ length}{\#\ of\ grains\ intercepted} \tag{3.5}$$

Table 3.2: Average grain diameter of perovskite calculated from SEM image.

Methods	Average grain diameter (nm)
One step	373.26
Two steps	157.89
SSE	144.51
Mixed cations	244.74

3.4 SURFACE TOPOLOGY: AFM

AFM characterization investigated the mean roughness of the surface of perovskite. Mean roughness depth, R_z = 541.631 nm, 525.95 nm and 338.103 nm were achieved for one step, two steps and SSE methods respectively. Even though SSE has small grain size but it has minimum surface roughness among all tree samples.

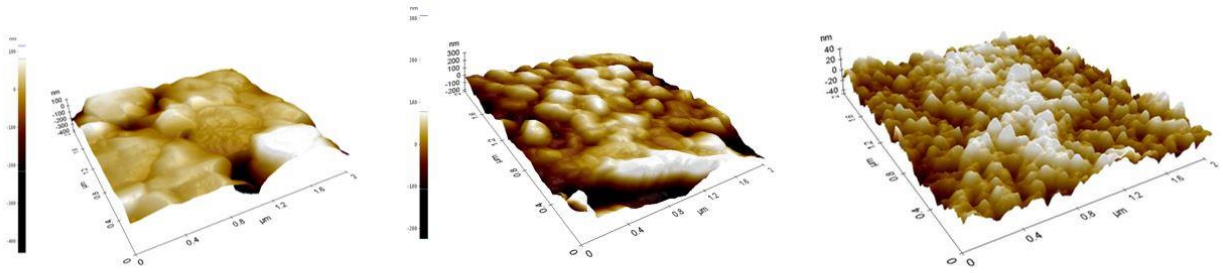

a) One step b) Two steps c) SSE

Figure 3.3: AFM topographic 3D images of the surface of 2µm × 2µm films.

3.5 OPTICAL PROPERTIES: UV-VIS

Figure 3.4 shows mixed cation has broader optical absorption into the red light wavelength which is better to enhance solar light harvesting compare to other samples. Using the absorbance data from the UV-Vis spectra, absorption coefficient can be determined. Figure 3.5 shows all samples have higher (10^5 cm^{-1}) absorption coefficient that Si (1.5×10^4 cm^{-1}) at the wavelength of 550 nm.

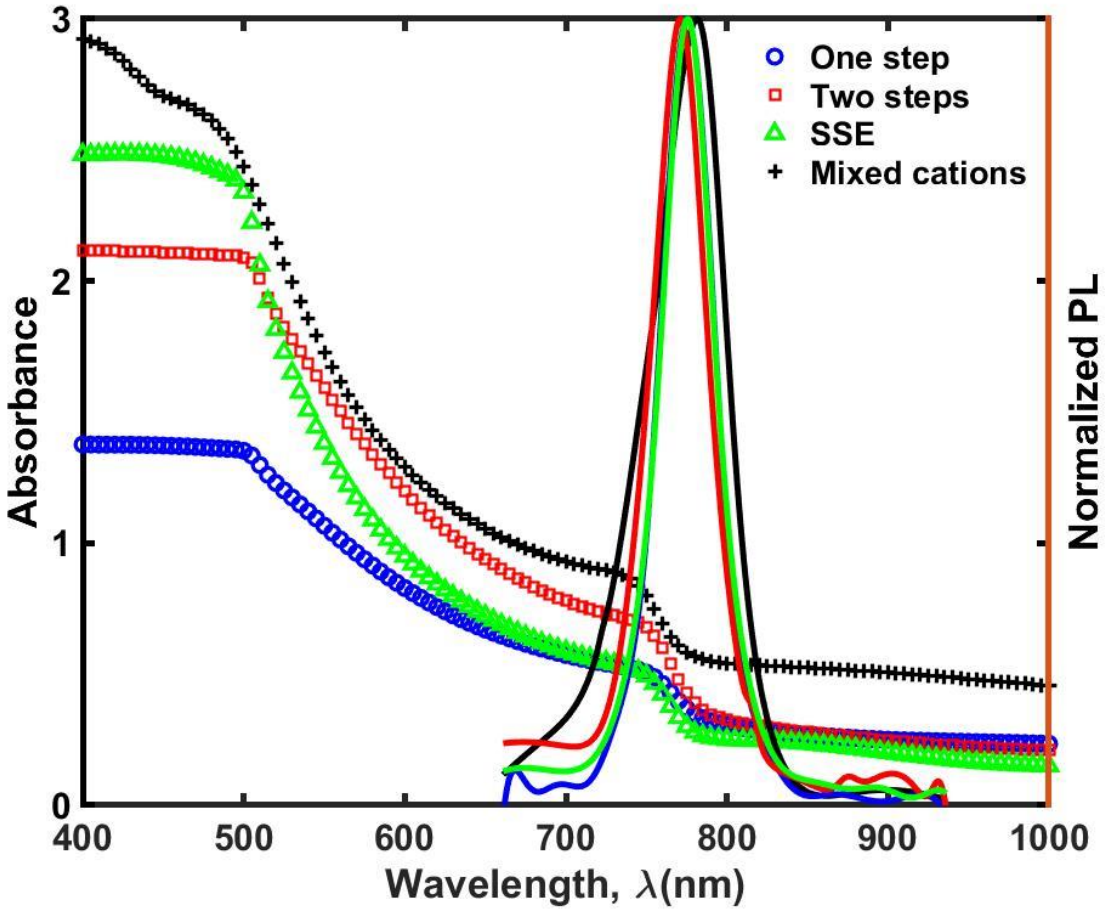

Figure 3.4: UV-vis absorbance and PL spectra of perovskite thin films.

$$Absorption\ coefficient, \alpha = \frac{2.303 \times A}{t} \tag{3.6}$$

Here,

A = absorbance and t = The thickness of the sample (nm)

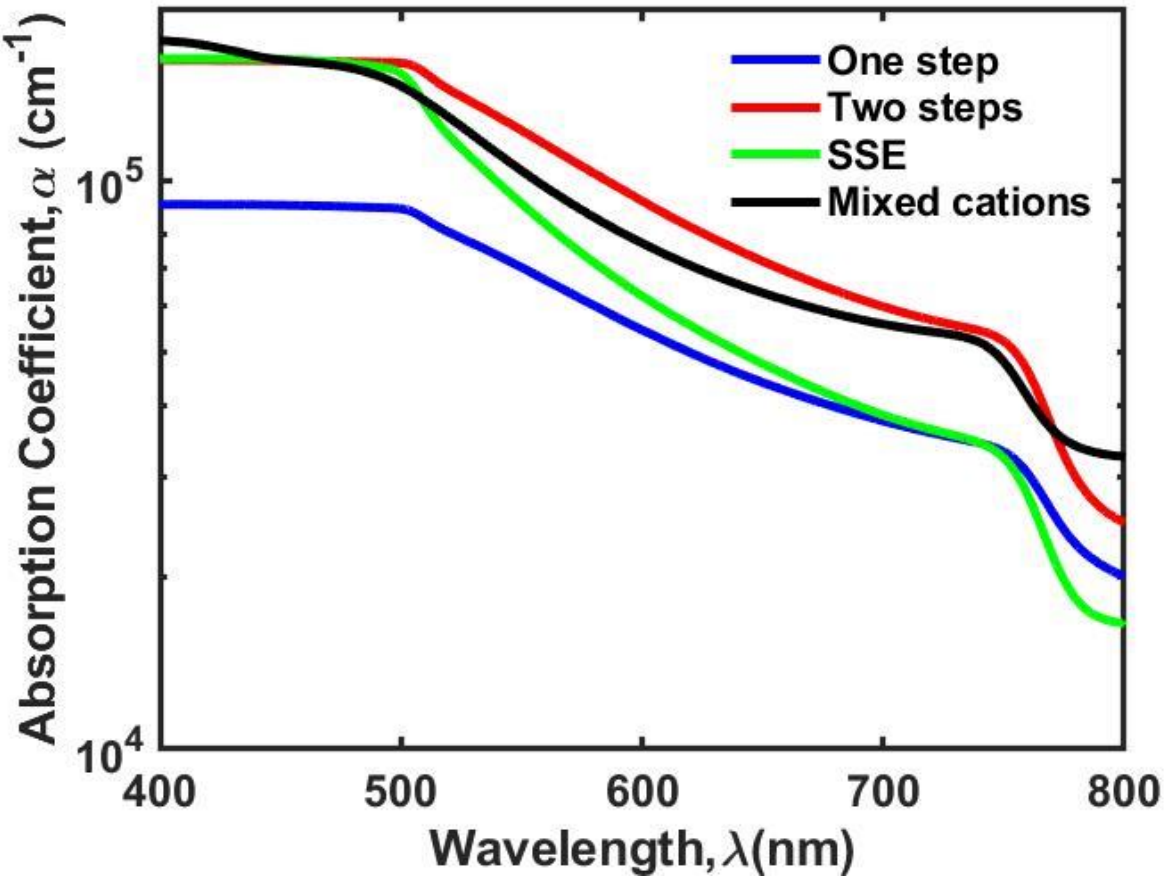

Figure 3.5: Absorption coefficient (α) as a function of wavelength for perovskite.

$$Lambert - Bree\ Law, I(d) = I_0 e^{(-\alpha d)} \tag{3.7}$$

Here,

I_0 = Intensity of light transmitted through the sample (W/m^2)

I = Intensity of light striking a sample through which light can be transmitted (W/m^2)

d = The thickness of the sample (nm)

α = Absorption Coefficient (cm^{-1})

Light intensity decreases exponentially [38]. High α sets the thickness of the absorber layer thinner which is around 300 nm to 500 nm thickness range for 1.6 eV bandgap. This

thickness can be calculated by taking the reciprocal of absorption coefficient, known by absorption depth or skin depth. Absorber layer thickness should be less than diffusion length to avoid the recombination.

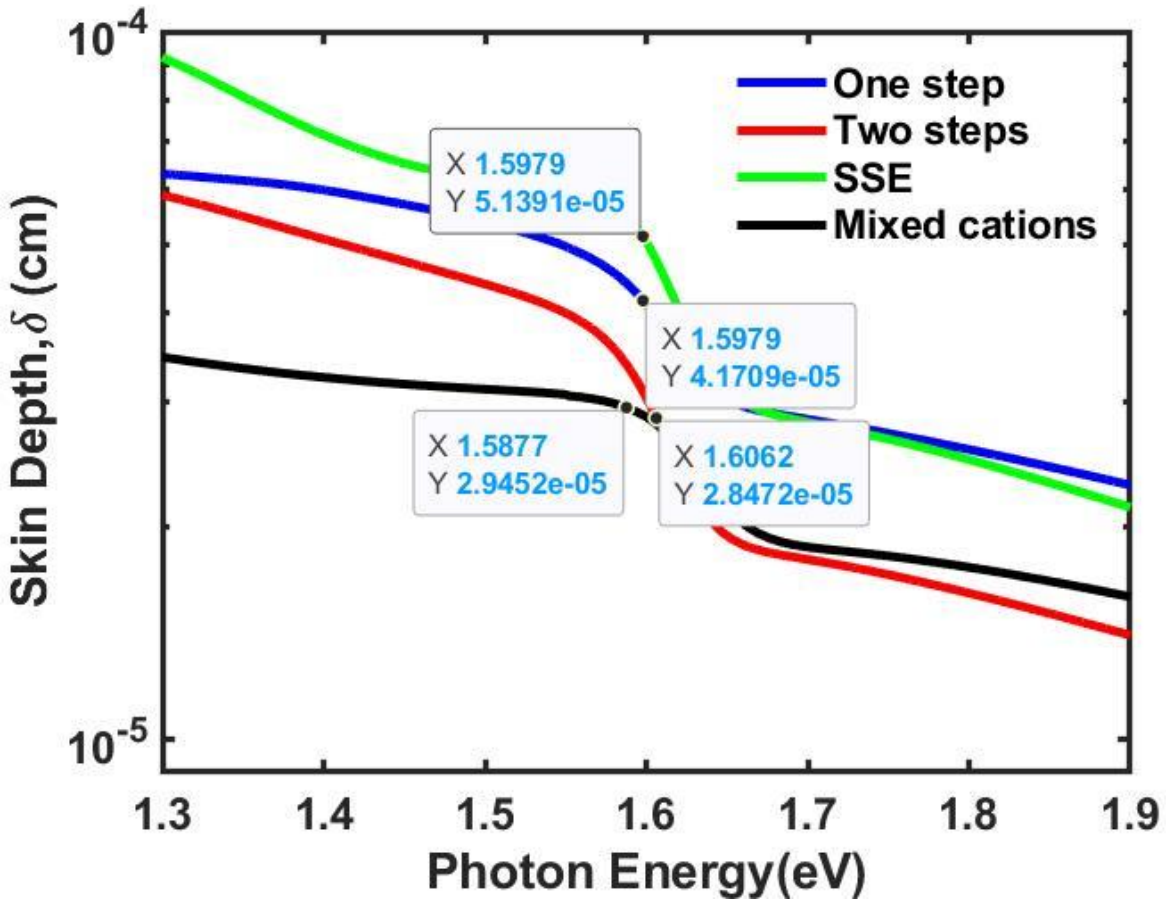

Figure 3.6: The Dependence of the skin depth upon the photon energy of perovskites.

$$Optical\ density, OD = \alpha \times t \tag{3.8}$$

Here,

α = Absorption coefficient (cm^{-1})

t = The thickness of the sample (nm)

Optical density was calculate by equation 3.8. A higher optical density indicates how much slower the wave travels through that material. Mixed cation has higher optical density among all samples. Optical density is the indicator of refractive index for the material.

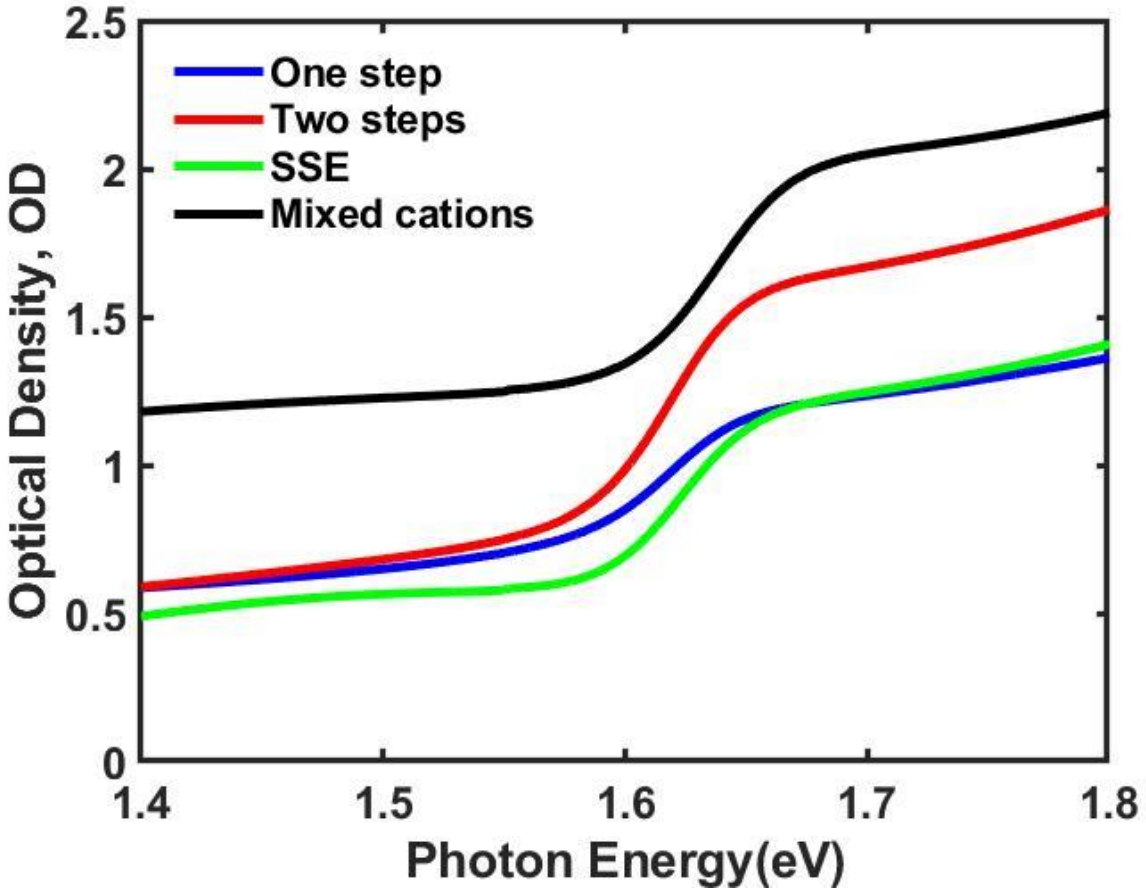

Figure 3.7: Variation of the optical density, OD as a function of the photon energy for perovskites.

$$Absorption\ coefficient, \alpha = \alpha_0 \exp\left(\frac{h\nu - E_g}{E_u}\right) \quad (3.9)$$

Here,

α_0 = Constant (cm^{-1})

$h\nu$ = photon energy (eV) and

E_u = The energy of the band tail or Urbach energy (eV)

Along the absorption coefficient curve and near the optical band edge there is an exponential part called Urbach tail. This exponential tail appears in the low crystalline, poor crystalline, the disordered and amorphous materials because these materials have localized states which extended in the band gap. Urbach energy is governed by the structural disorder, imperfection in stoichiometric and passivation at the surface. Urbach energy also indicates the disorder of phonon states in the film. Urbach energy Eu is found below absorption band edge of compound. The generation of absorption edge at the band gap energy is due to exciton phonon interaction or may be due to electron phonon interaction. This can be estimated from steepness parameter. The band bending causes reduction in optical band gap. The higher Eu defines the high disorder of phonon states, lattice distortions and high defect densities. It has been suggested that the manifestation of traps in hybrid perovskites is influenced by their composition and fabrication method. Figure 3.8 shows mixed cation has higher urbach energy which is the indication of high disorder of phonon states, lattice distortions and high defect densities [39].

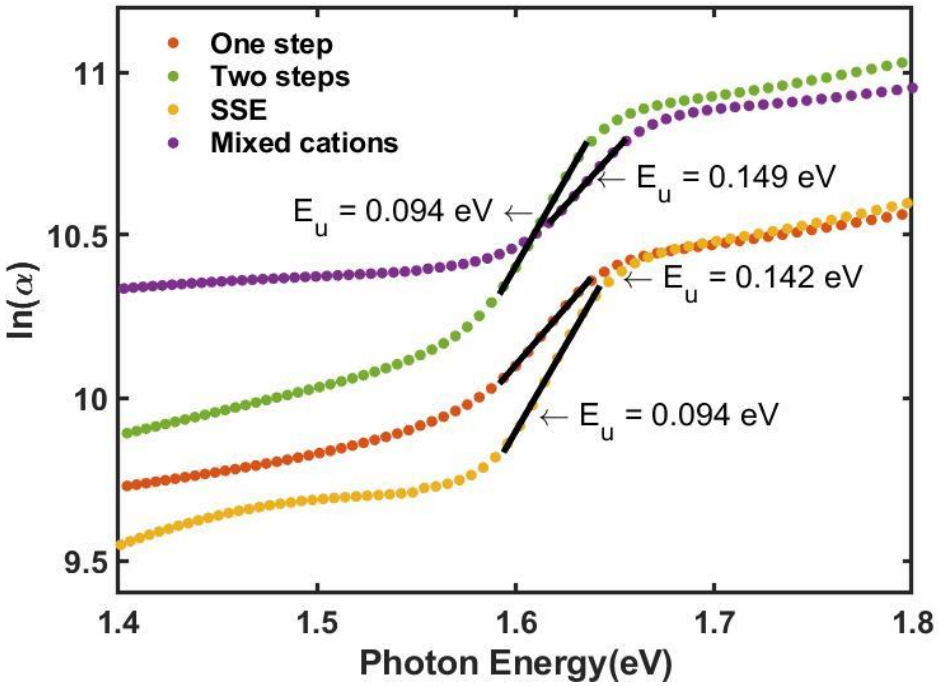

Figure 3.8: Urbach energies extracted from absorbance measurements (UV-Vis) plotted against the bandgap.

To determine the urbach energy, we have to take both side natural log of equation 3.9 to find out the slopes. The inverse of the slope gives us the urbach energy.

3.6 ELECTRONIC PROPERTIES: PL, TRPL, HALL

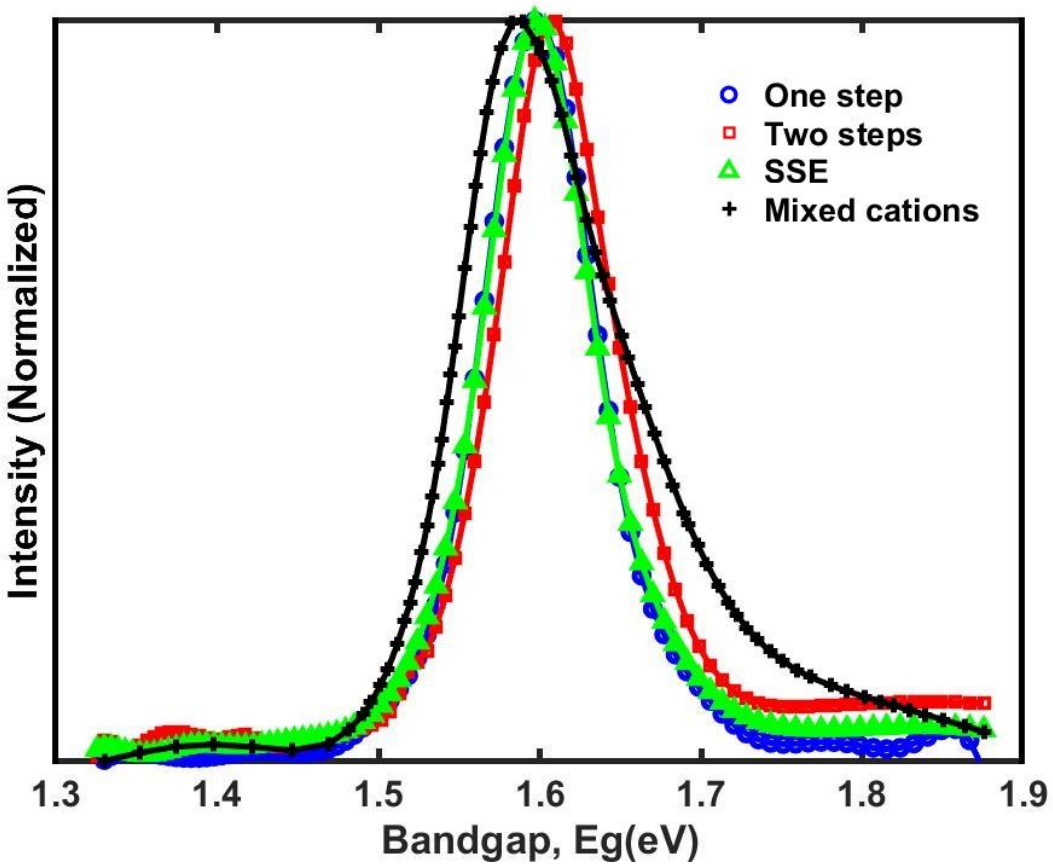

Figure 3.9: PL spectra of the perovskite films.

PL spectra give us the exact band gap of perovskite. One step, two steps and SSE have a bang gap of 1.6 eV and mixed cation has 1.58 eV.

Lifetime profile was obtained by the results of TRPL. TRPL output gave us a decay curve. We used double exponential model to fit the decay curves. Double exponential model gave us amplitude components and lifetime components [40]. Finally, by using amplitude

weighted average lifetime equation we can achieved the average lifetime of perovskite layers [41].

Table 3.3: Extracted bandgap of perovskites from PL spectra.

Method	Bandgap, E_g(eV)
One step	1.5989
Two steps	1.6075
SSE	1.5986
Mixed cations	1.5866

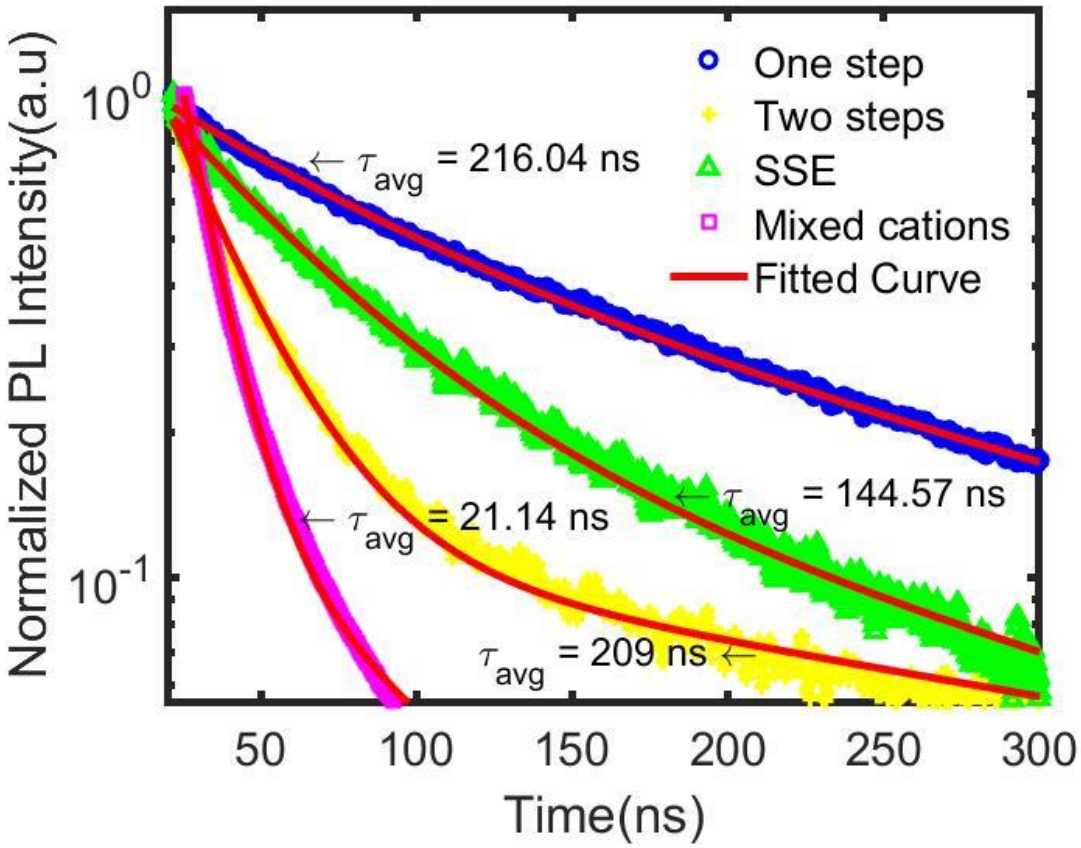

Figure 3.10: Time resolution photoluminescence (TRPL) analysis of perovskite films.

$$\frac{I(t)}{I_0} = A_1 \exp\left(\frac{-t}{\tau_1}\right) + A_2 \exp\left(\frac{-t}{\tau_2}\right) \quad (3.10)$$

Here,

A_1 = Amplitude of component 1

τ_1 = Lifetime of component 1

A_2 = Amplitude of component 2

τ_2 = Lifetime of component 2

$$Amplitude\ weighted\ average\ lifetime, \tau_{average} = \frac{\sum_{i=1}^{n} A_i \times \tau_i^2}{\sum_{i=1}^{n} A_i \times \tau_i} \quad (3.11)$$

Here,

n = 2

A = Amplitude of component and

τ = Lifetime of component

Table 3.4: Extracted the fitting decay lifetimes of τ_1, τ_2 and the average lifetime τ_{avg} from TRPL.

Method	τ_1 (ns)	τ_2 (ns)	τ_{avg} (ns)
One step	69.88	264.55	216.04
Two steps	25.13	386.7	209
SSE	49.58	229.78	144.57
Mixed cation	11.55	81.3	21.14

Table 3.4 shows one step method has the highest lifetime among all samples. Mixed cation has the lowest lifetime among all samples. Even though it has good average grain size but has higher urbach energy which means it has higher disorder of phonon states, lattice distortions

and high defect densities. It cause a high recombination so the lifetime of mixed cation is very low.

Hall measurement reported that two steps deposition has higher mobility than one step deposition. Richness of PbI_2 helps two steps method to acquire higher mobility [42].

Table 3.5: Mobility (μ), Bulk Concentration (N_b), Resistivity (ρ), Conductivity (σ) at room temperature.

	Electronic Properties			
	Mobility, μ (cm^2/V-s)	Bulk Concentration, Nb (cm^-3)	Resistivity, ρ (Ω-cm)	Conductivity, σ (1/Ω-cm)
One step S1	5.27	5.91E+12	2.00E+05	5.00E-06
One step S2	7.17	4.50E+12	1.93E+05	5.17E-06
Average	6.22	5.21E+12	1.97E+05	5.08E-06
Two steps S1	75.12	6.06E+11	1.37E+05	7.29E-06
Two steps S2	55.20	5.72E+11	1.98E+05	5.06E-06
Average	65.16	5.89E+11	1.67E+05	6.17E-06

MAI-rich and PbI_2-rich perovskite films are p and n self-doped respectively. From Table 3.6, one step has lower CH_3NH_3I than PbI_2 on the other hand, two steps has higher CH_3NH_3I than PbI_2 [43, 44].

Table 3.6: Type of semiconductor depends on the quantity of MAI and PbI_2.

	CH_3NH_3I	PbI_2	Type Semiconductor
One step	0.395g	1.157g	n
Two steps	100μL	20μL	p

3.7 SURFACE CHEMISTRY: XPS

To determine the elemental composition of the perovskite layers, XPS spectra were recorded in the binding energy range of 0–1100 eV. The identified elements in the samples are lead, iodine, bromine (in only the mixed-cation sample) oxygen, nitrogen, and carbon. In here only I 3d5/2, and Pb 4f7/2 were shown in figure 3.11.

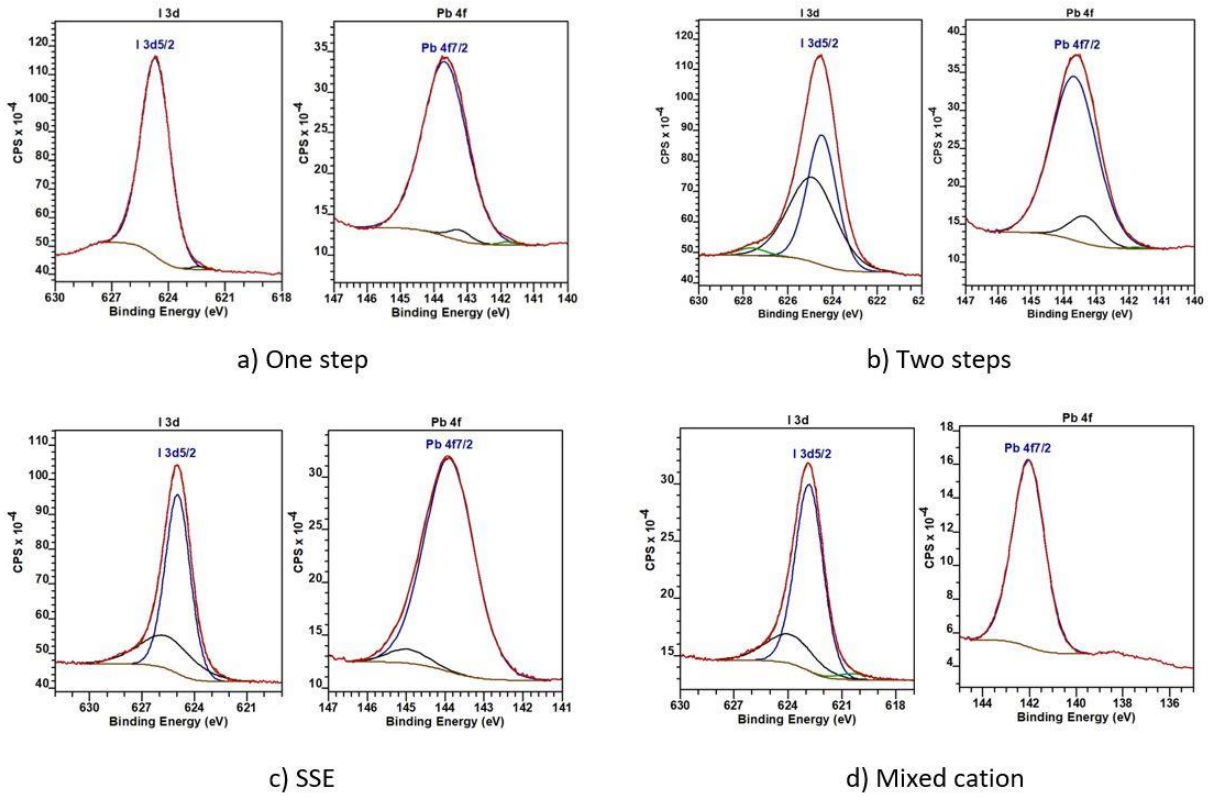

Figure 3.11: X-ray photoelectron spectroscopy (XPS) survey spectra of perovskite films documented for I 3d5/2, and Pb 4f7/2.

In all the samples, the iodine 3d5/2 peak shifts from the actual position of a binding energy of 619.3 eV [45]. For one-step deposition, the 3d5/2 peak was shifted by 5.2 eV (from 619.3 to 624.5 eV). Shifts of 5.7 eV (from 619.3 to 625 eV) and 4.2 eV (from 619.3 to 623.5 eV) were observed for the SSE and two steps samples. The mixed-cation sample exhibited a shift of 3.7 eV (from 619.3 to 623 eV), which is the smallest shift among all samples. The shifted peaks of all the samples are representative of the iodate IO_3^- group [46]. The core-level spectrum of lead has a distinct Pb 4f7/2 peak at 136.9 eV [45]. A close look at the high-energy peak of each sample indicates that binding-energy shifts of the distinct Pb 4f7/2 peak of 6.7 (from 143.6 to 136.9 eV), 7.1 (from 144 to 136.9 eV), 5.7 (from 142.6 to 136.9 eV), and 5.1 eV (from 142 to 136.9 eV) were calculated for the one-step deposition, SSE, two steps, and mixed-cation samples, respectively.

Table 3.7: Calculations of the atomic percentage of each element and the ratio of I:Pb for one step deposition.

Element	Main Peaks	Accurate R.S.F	Area 1	Area 2	Area 3	Total Area	NA (Normalized Area) = A/ Accurate R.S.F	Atomic Percentage = NA/∑ NA	Ratio	
Carbon (C)	1s	0.02228	129739	25234.4	3313.7	158286.8	7104434.47	0.27641229	I/Pb =	2.588
Nitrogen (N)	1s	0.03958	165775	24890.9	16920.7	207586.9	5244742.294	0.204057231		
Oxygen (O)	1s	0.06354	17866.4	341782	216072	575720.7	9060760.151	0.352527069		
Iodine (I)	3d5/2	0.44154	1357610	9428.3	0	1367038	3096068.08	0.120458746		
Lead (Pb)	4f7/2	0.311542857	359456	11021.5	2223.1	372700.4	1196305.393	0.046544664		
						Total =	25702310.39			

Table 3.8: Calculations of the atomic percentage of each element and the ratio of I:Pb for two steps deposition.

Element	Main Peaks	Accurate R.S.F	Area 1	Area 2	Area 3	Total Area	NA (Normalized Area) = A/ Accurate R.S.F	Atomic Percentage = NA/∑ NA	Ratio	
Carbon (C)	1s	0.02228	122077.1	14424.7	2812.6	139314.4	6252890.485	0.232093906	I/Pb =	2.478
Nitrogen (N)	1s	0.03958	195626.1	20243.3	13958.7	229828.1	5806672.562	0.215531252		
Oxygen (O)	1s	0.06354	385880.7	254987.7	0	640868.4	10086062.32	0.374373036		
Iodine (I)	3d5/2	0.44154	718386.9	750929.7	39397.2	1508713.8	3416935.725	0.126829337		
Lead (Pb)	4f7/2	0.311542857	383812.9	44385.1	1310	429508	1378648.202	0.051172469		
						Total =	26941209.3			

Table 3.9: Calculations of the atomic percentage of each element and the ratio of I:Pb for solvent to solvent extraction deposition.

Element	Main Peaks	Accurate R.S.F	Area 1	Area 2	Area 3	Total Area	NA (Normalized Area) = A/ Accurate R.S.F	Atomic Percentage = NA/∑ NA	Ratio	
Carbon (C)	1s	0.02228	159747.2	15994.6	2263.6	178005.4	7989470.377	0.290825368	I/Pb =	2.684
Nitrogen (N)	1s	0.03958	188828.5	22636.8	10215.2	221680.5	5600821.122	0.20387595		
Oxygen (O)	1s	0.06354	456137.8	120279.1	46461.8	622878.7	9802938.307	0.356837563		
Iodine (I)	3d5/2	0.44154	938094.5	373892.7	0	1311987.2	2971389.229	0.108161784		
Lead (Pb)	4f7/2	0.311542857	313635.3	31271.2	0	344906.5	1107091.664	0.040299335		
						Total =	27471710.7			

Table 3.10: Calculations of the atomic percentage of each element and the ratio of I:Pb for mixed cation solution processing.

Element	Atomic Number	Main Peaks	Accurate R.S.F	Area 1	Area 2	Area 3	Area 4	Total Area	NA (Normalized Area) = A/ Accurate R.S.F	Atomic Percentage = NA/∑ NA	Ratio	
Carbon (C)	6	1s	0.02228	38981.3	12783	0	0	51763.8	2323330.341	0.185596989	I/Pb	1.521027
Nitrogen (N)	7	1s	0.03958	26695.6	11761	2113	7968.8	48537.9	1226323.901	0.097963694		
Oxygen (O)	8	1s	0.06354	163994	130530	4326.2	1576.9	300426.7	4728150.771	0.377703735		
Bromine (Br)	35	3d5/2	0.040716	55195.7	53354	0	0	108549.3	2666010.905	0.212971693		
Iodine (I)	53	3d5/2	0.44154	321606	86146	11645	0	419397.1	949850.7496	0.075877905		
Lead (Pb)	82	4f7/2	0.311542857	194552	0	0	0	194552.3	624480.0532	0.049885983		
								Total =	12518146.72			

Calculations of the atomic percentage of each element and the ratio of I:Pb are shown above tables. We did not do C 1s calibration in casaXPS software. This is why all ration values are off to the desire value.

3.8 SUMMARY

The XRD results show a secondary phase of PbI_2 for the SSE and Two steps method. One step has the highest crystallite size of 40 nm besides mixed cations has 38 nm. The SEM

results confirm that the one-step deposition exhibited pinhole formation, loosely packed grains and incomplete coverage. The SSE, Two steps and Mixed-cations samples have small grains and closely and neatly packed films with minimum pinhole formation and a good coverage area. One step has the best average grain diameter of 373.26 nm however mixed cation has 244.74 nm. Mixed-cations sample exhibits the lowest shift in XPS results among all the samples. Mixed cation has higher optical absorption into the red to enhance solar light harvesting. All samples have high absorption co-efficient (10^5 cm^{-1}) and 300 nm to 500 nm thickness range for 1.58 to 1.6 eV bandgap. Mixed cations sample has the highest urbach energy, Eu = 149 meV. The higher Eu defines the high disorder of phonon states in the film. One step has the highest lifetime of 216.04 ns where mixed cations has 21.14 ns because of higher disorder of phonon states. In conclusion, based on the results, the mixed-cation sample shows the most promising results for a high performance planar structure perovskite solar cell.

Chapter 4: ETM, Absorber and HTM Layers Optimization

4.1 INTRODUCTION

The aim of using planar heterojunction PSCs is to reduce the complexity, and ultimately to do that, it is essential to eliminate the mesoporous scaffold without sacrificing the efficiency. The main advantage of such a PSC structure is that it is free of high-temperature steps such as the mesoporous TiO_2 layer, thereby requiring fewer steps to fabricate PSCs. Currently, the two popular perovskite configurations are the n-i-p mesoporous and planar heterojunction PSCs. In the present work, we focus on both structures by using one step method and mixed-cation perovskite as an absorber layer. Because of the extremely high absorption coefficient of perovskites, a layer that is less than 400 nm thick is generally sufficient for absorbing most of the sunlight, and planar-structure PSCs have also exhibited efficiencies of more than 17% []. In the present work, the thickness of the mixed-cation perovskite layer for planar heterojunction solar cells is less than 400 nm. It has been reported that a metal-oxide layer such as TiO_2 or ZnO [] can be used as the electron-transport layer for high-efficiency PSCs (15% efficiency). This electron-transport layer also serves as a hole-blocking layer to mitigate recombination at the interface. The lack of an existing porous scaffold has a dramatic effect on the coating and growth of the perovskite material, and so additional optimization is often necessary when converting a deposition method from mesoporous to planar structures. In the present work, to optimize the electron-transport layer, we investigate who give us good results between mesoporous and planar structure and also systematically how the thickness of the compact TiO_2 layer affects the device performance by using different spin speeds to fabricate this layer.

4.2 MESOPOROUS TiO_2

4.2.1 Deposition

The clean substrates was spin-coated with 0.15M and 0.3M titanium diisopropoxide bis(acetylacetonate) (Aldrich) at 3,000 r.p.m. for 30s subsequently. After drying at 125°C for 10

min, they were sintering at 550°C for 15 min in air. The substrate was immersed in 50 mM $TiCl_4$ (Aldrich) aqueous solutions for 30 min at 70°C and washed with distilled water and ethanol, followed by annealing at 550°C for 30 min in air to form a compact n-type layer of TiO_2(c-TiO_2) [47].

4.2.2 Characterization

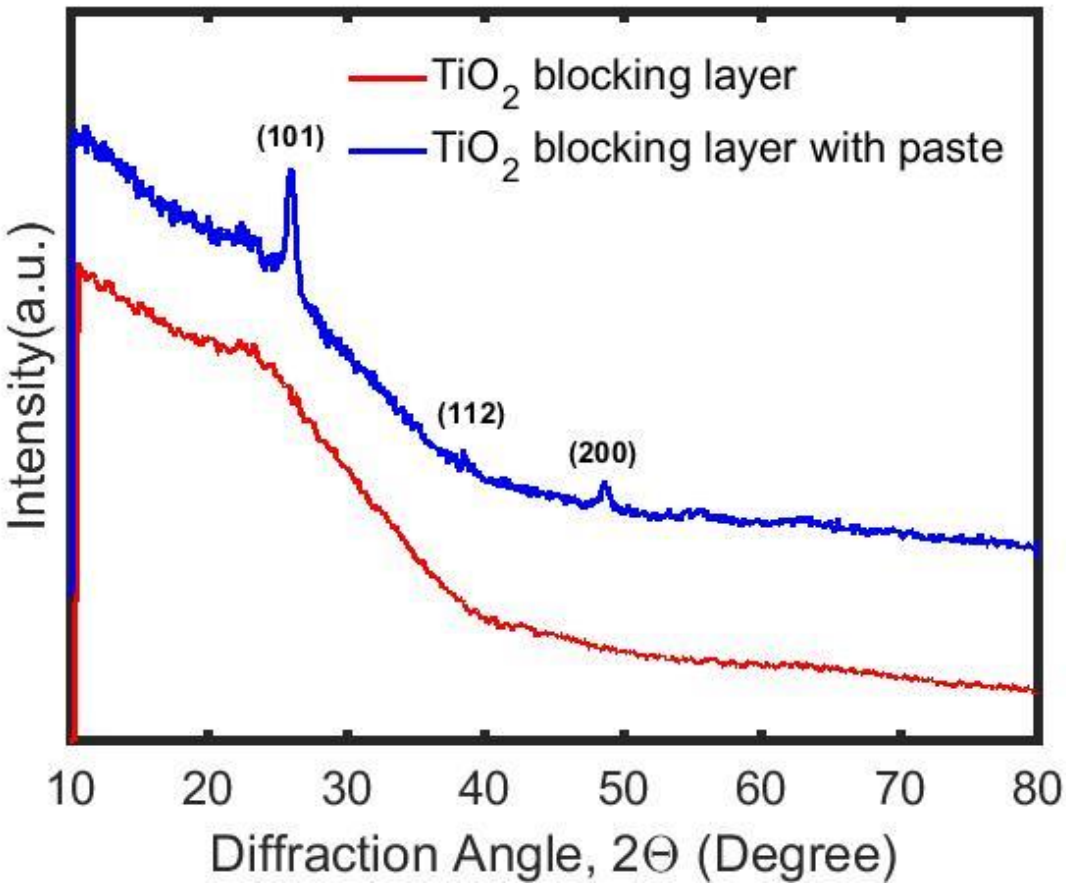

Figure 4.1: XRD patterns of TiO_2 anatase mesoporous film.

XRD results showed only few miller indices it means this mesoporous TiO_2 did not have exact stoichiometry.

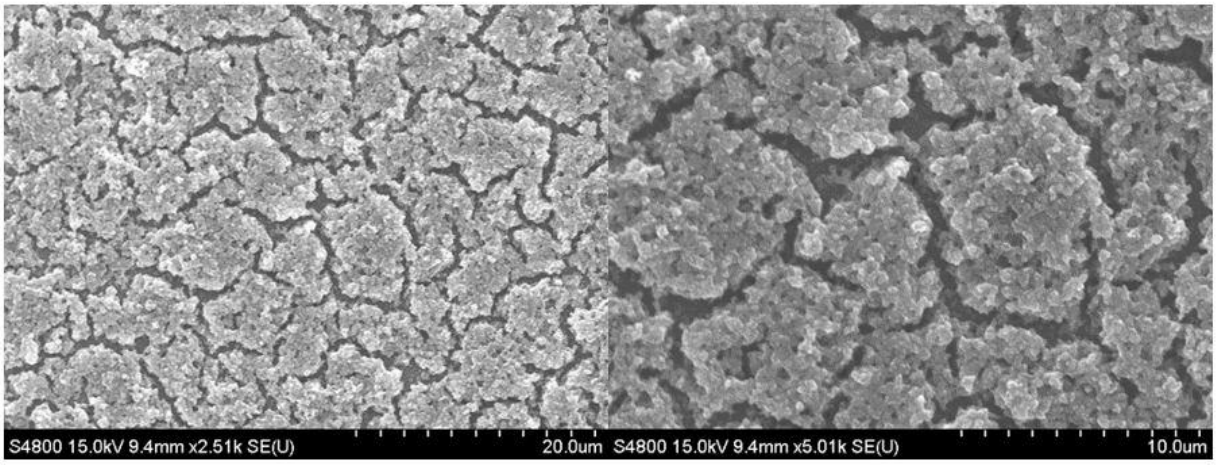

Figure 4.2: Low- and high-magnification SEM micrographs of the top surface of mesoporous TiO_2 films deposited on a glass substrate.

SEM images show us this layer of TiO_2 is very thick and bulky. It has big fractures when we deposited this layer. It indicates the quality of this layer is poor.

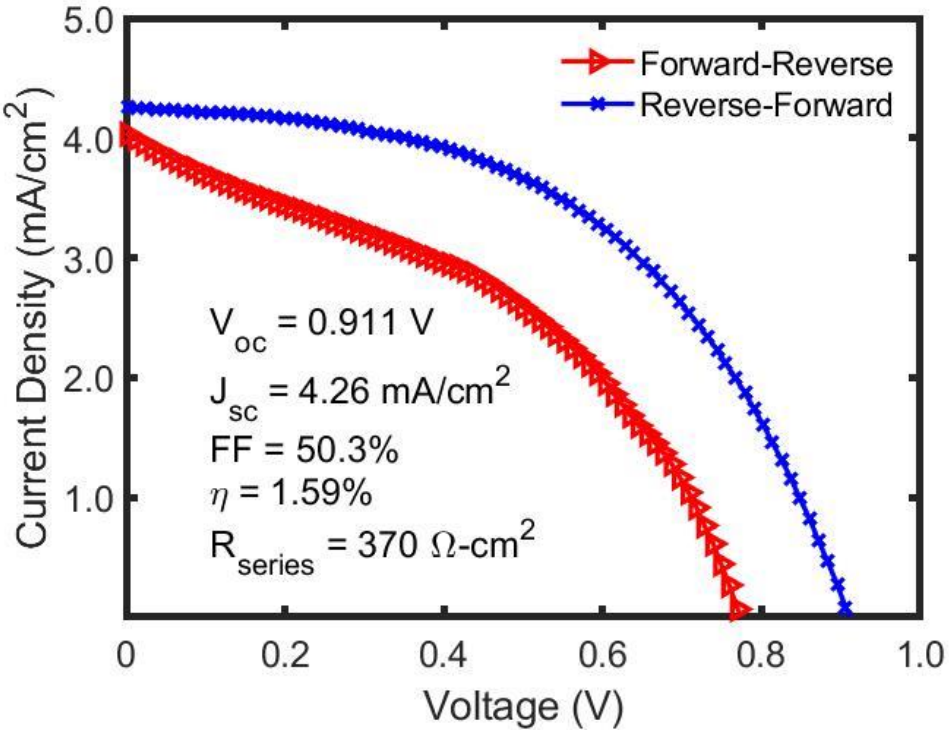

Figure 4.3: Current density vs voltage (J–V) curves from forward and reverse scans of mesoporous TiO_2 based one step deposition PSCs.

Poor quality of mesoporous TiO_2 layer increase the series resistance of a device. Increase of series resistance has higher recombination and it decreases the current and eventually we have a poor PV characteristic.

4.3 SOLARONIX TiO_2 BLOCKING LAYER

4.3.1 Deposition

A compact TiO^2 blocking layer was deposited on the cleaned FTO substrate by spin-coating the solution (at 5000 rpm/min for 30 s) and annealing the coated substrates at 550°C for 1 h.

4.3.2 Characterization

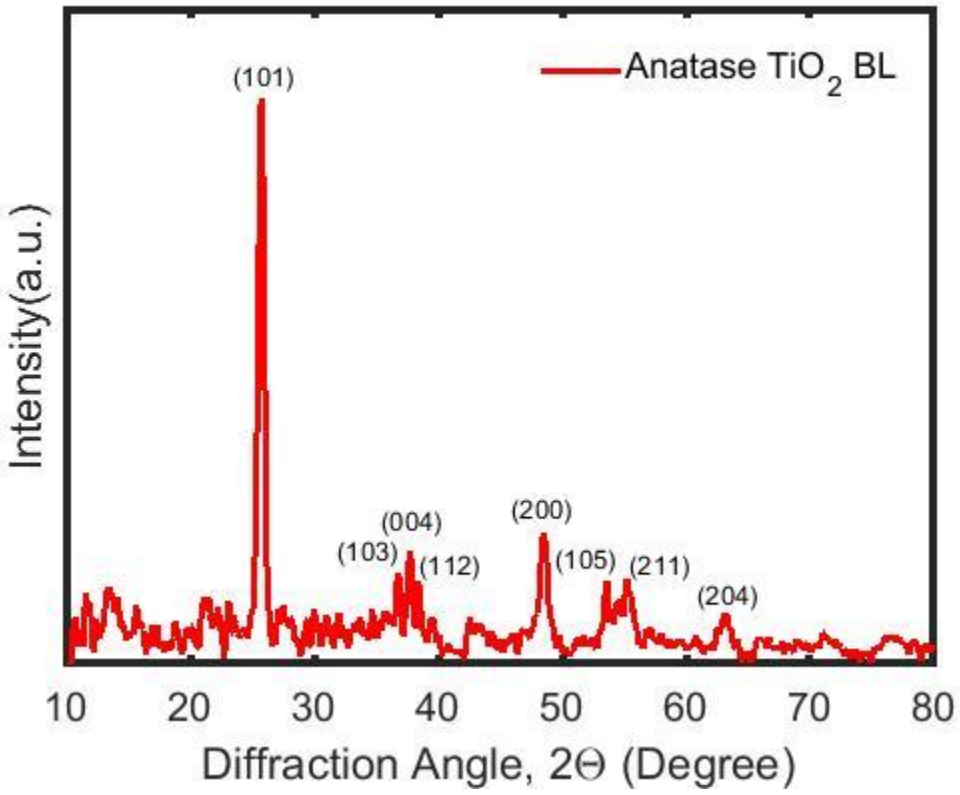

Figure 4.4: XRD patterns of TiO_2 anatase blocking layer film.

XRD results show all diffraction peaks and it indicates a good quality of anatase TiO_2 blocking layer.

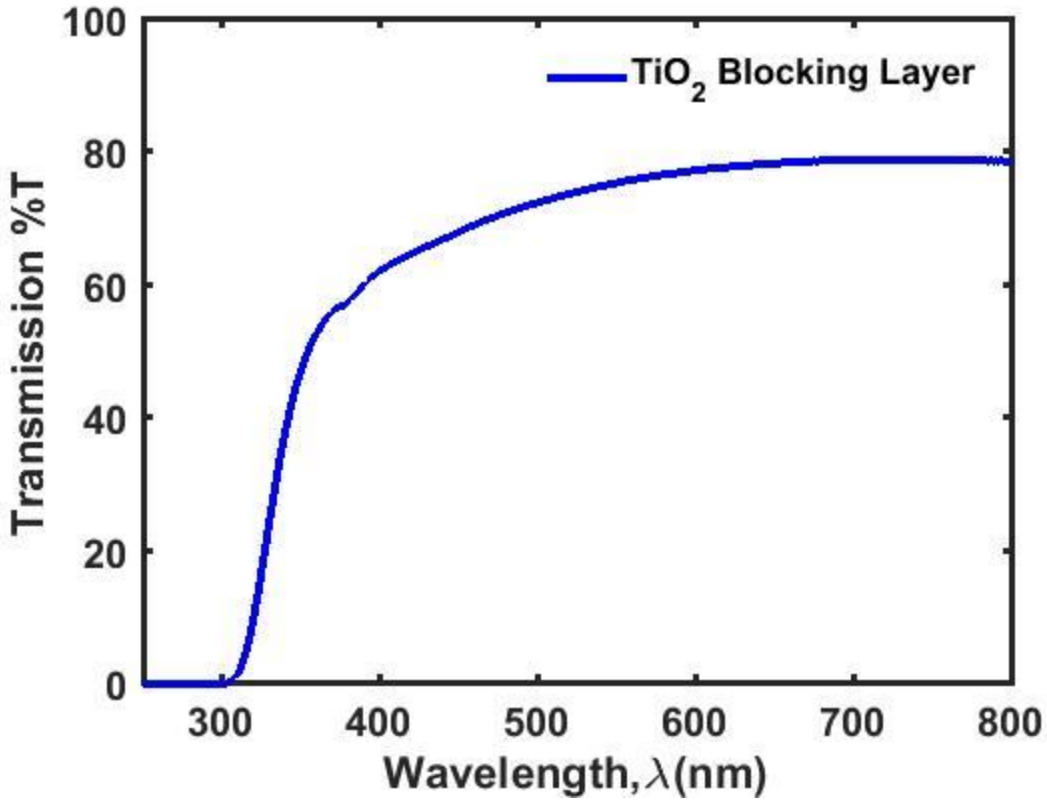

Figure 4.5: Optical transmission spectrum through anatase TiO_2 film.

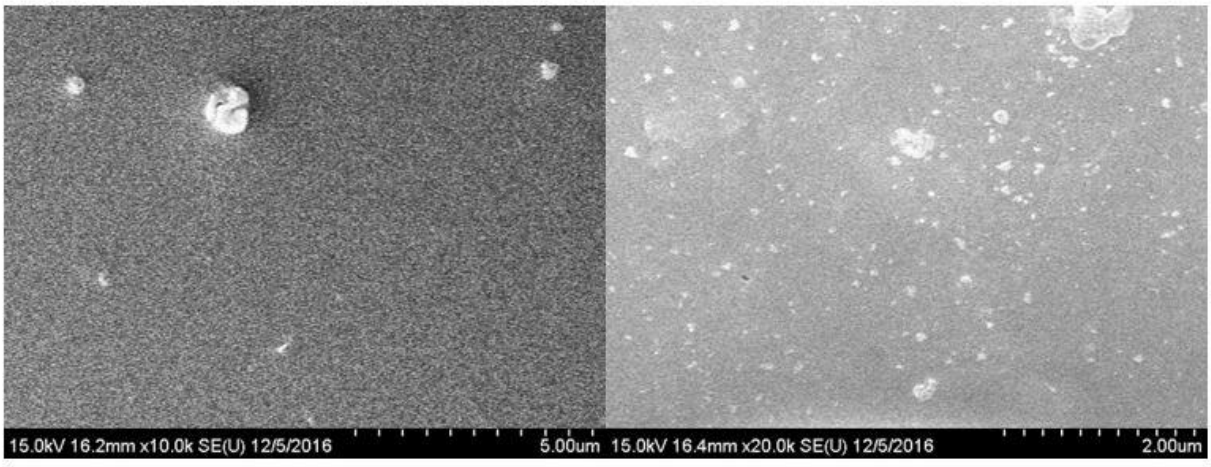

Figure 4.6: Low- and high-magnification SEM micrographs of the top surface of solaronix blocking layer TiO_2 films deposited on a glass substrate.

Transmission and SEM results show us promising results. 80% transmission was achieved and there are no fractures shown in SEM image. The grain size are small and it has a full coverage on samples.

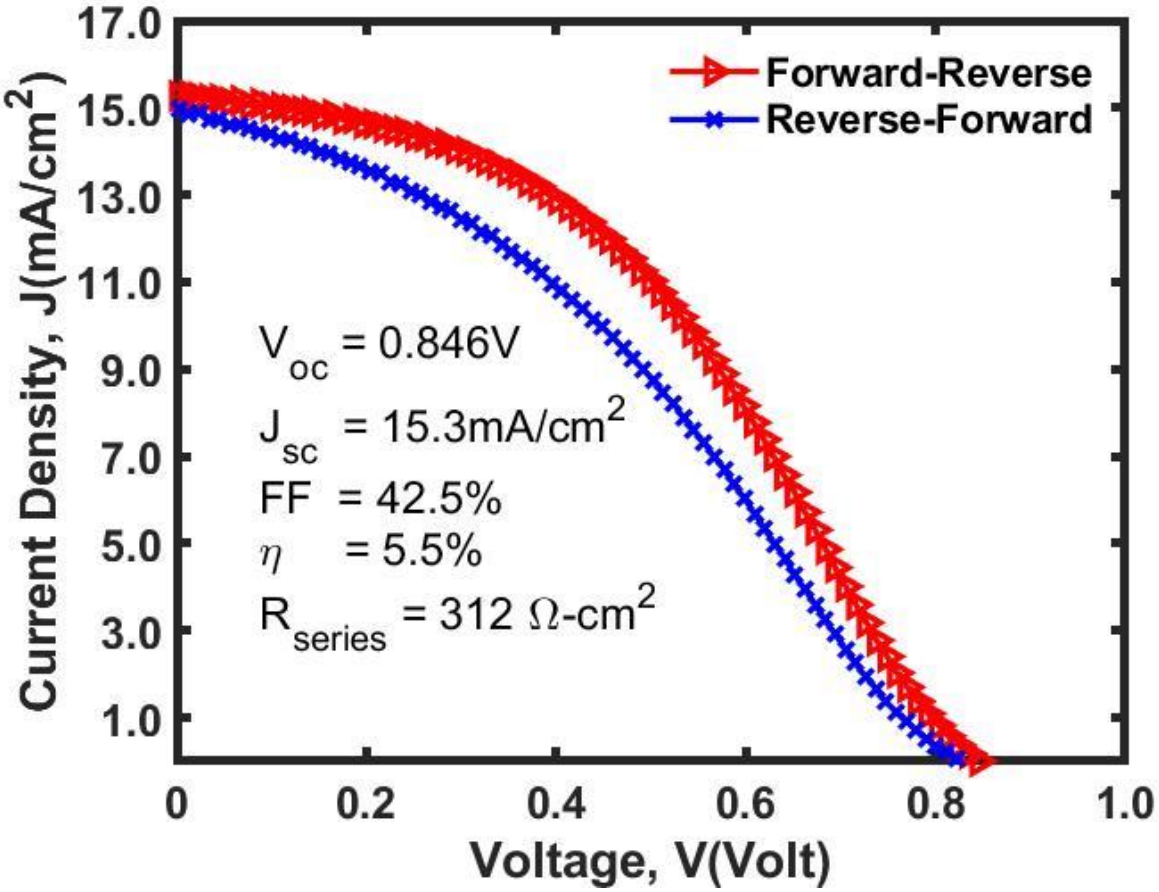

Figure 4.7: Current density vs voltage (J–V) curves from forward and reverse scans of solaronix blocking layer TiO_2 based one step deposition PSCs.

Comparatively good J_{sc} because of good quality of TiO_2 but still not in optimal condition.

4.4 Influence of temperature and thickness on ETM layer

Annealing shows us a significant change in mobility. Thicker TiO_2 layer achieved more mobility which should be a good sign for high efficiency solar cell.

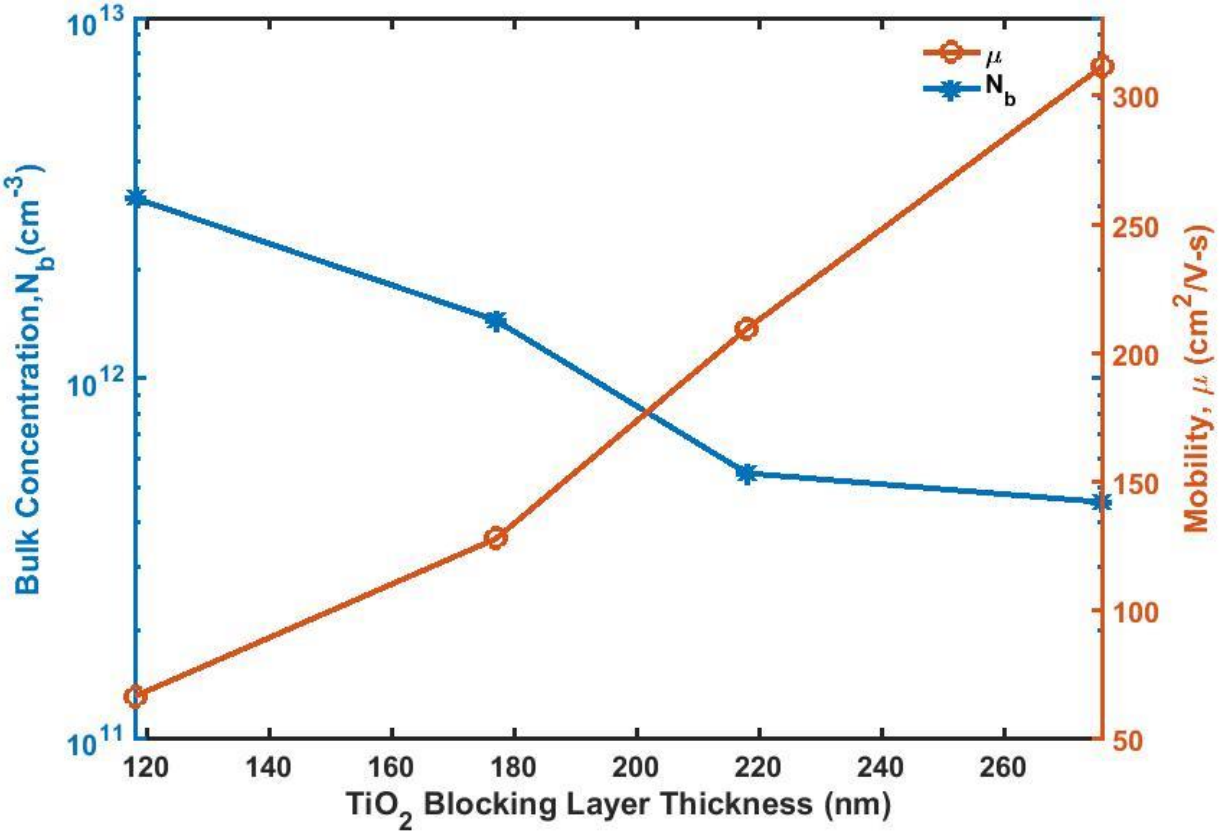

Figure 4.8: Effect on bulk concentration (N_b) and mobility (μ) by increasing the thickness of TiO_2 blocking layer.

Table 4.1: Effect on bulk concentration, mobility, resistivity and conductivity by annealing the TiO_2 blocking layer.

	No Annealing	Annealing
Mobility, μ (cm^2/V-s)	26.6	307.1
Bulk Concentration, N_b (cm^-3)	2.89E+12	2.58E+11
Resistivity, ρ (Ω-cm)	8.12E+04	7.89E+04
Conductivity, σ (1/Ω-cm)	1.23E-05	1.27E-05

4.5 BILAYER PEROVSKITE

ISO 4287			
Amplitude parameters - Roughness profile			
Rp	333	nm	Gaussian filter, 0.25 mm
Rv	277	nm	Gaussian filter, 0.25 mm
Rz	611	nm	Gaussian filter, 0.25 mm
Rc	217	nm	Gaussian filter, 0.25 mm
Rt	611	nm	Gaussian filter, 0.25 mm
Ra	70.3	nm	Gaussian filter, 0.25 mm
Rq	91.5	nm	Gaussian filter, 0.25 mm
Rsk	0.0493		Gaussian filter, 0.25 mm
Rku	3.49		Gaussian filter, 0.25 mm
Material Ratio parameters - Roughness profile			
Rmr	100	%	c = 1000 nm under the highest peak, Gaussian filter, 0.25 mm
Rdc	139	nm	p = 20%, q = 80%, Gaussian filter, 0.25 mm

Single layer

ISO 4287			
Amplitude parameters - Roughness profile			
Rp	68.1	nm	Gaussian filter, 0.25 mm
Rv	71.1	nm	Gaussian filter, 0.25 mm
Rz	139	nm	Gaussian filter, 0.25 mm
Rc	64.7	nm	Gaussian filter, 0.25 mm
Rt	139	nm	Gaussian filter, 0.25 mm
Ra	22.0	nm	Gaussian filter, 0.25 mm
Rq	28.0	nm	Gaussian filter, 0.25 mm
Rsk	0.0823		Gaussian filter, 0.25 mm
Rku	2.85		Gaussian filter, 0.25 mm
Material Ratio parameters - Roughness profile			
Rmr	100	%	c = 1000 nm under the highest peak, Gaussian filter, 0.25 mm
Rdc	43.3	nm	p = 20%, q = 80%, Gaussian filter, 0.25 mm

Double layer

Figure 4.9: Mean roughness depth (R_z) comparison between single layer and bilayer one step deposition.

After bilayer one step perovskite, we observed a remarkable change in mean roughness depth. Second layer acts like a passivation layer and it smooth the surface and prevent shunting the devices.

4.6 SPIRO-OMETAD IS BETTER HTM THAN P3HT

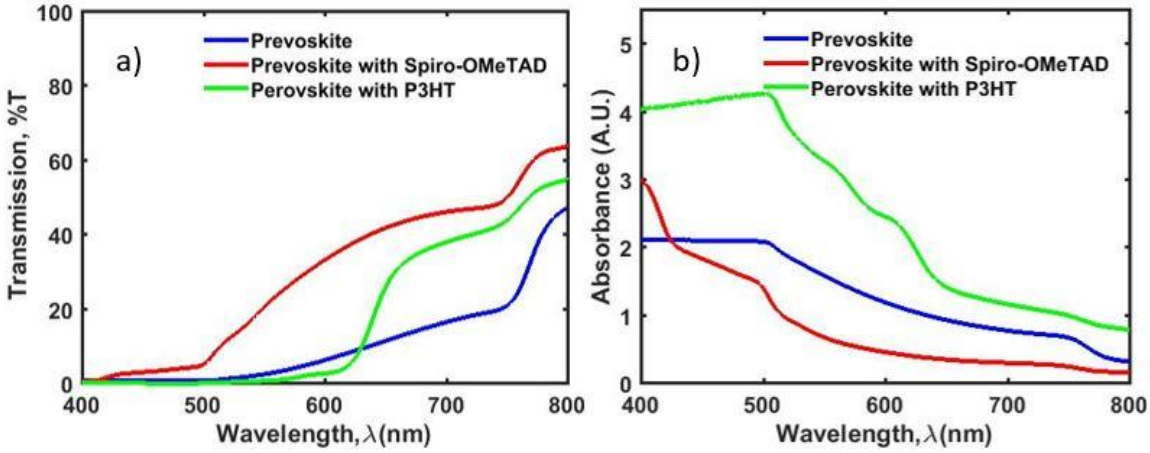

Figure 4.10: a) Optical transmission spectrum for perovskite, perovskite with Spiro-OMeTAD and perovskite with P3HT and b) Optical absorbance spectrum for perovskite, perovskite with Spiro-OMeTAD and perovskite with P3HT.

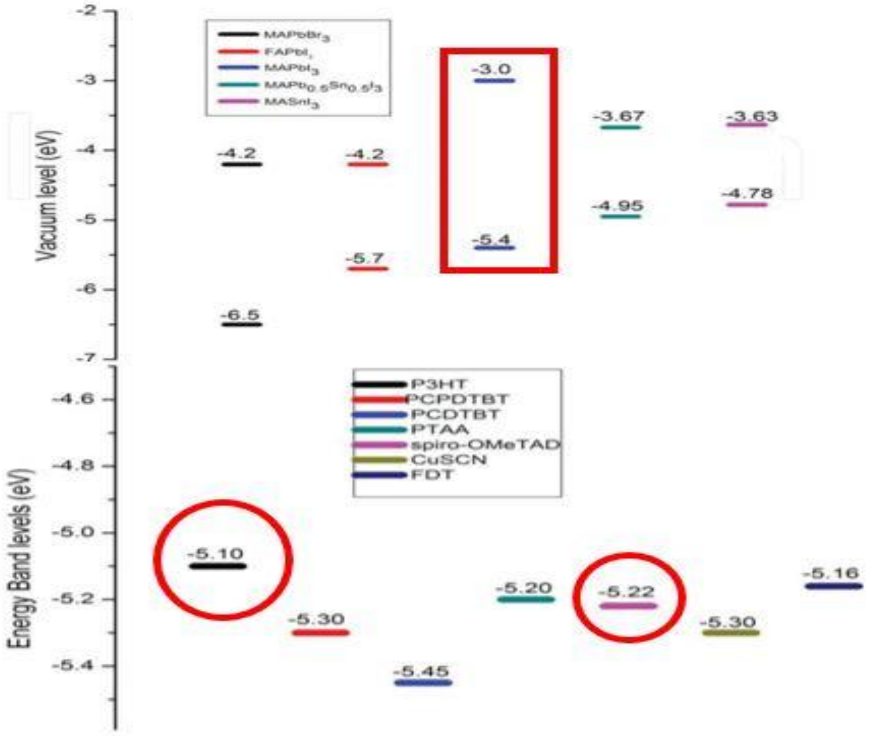

Figure 4.11: Energy bandgap diagram of hybrid perovskite materials.

UV-Vis results showed us perovskite with P3HT has more absorbance compare to perovskite with Spiro-OMeTAD. In that sense, P3HT is better than Spiro-OMeTAD. But energy band diagram shows us $\Delta E_{V,PVSK\text{-}P3HT} > \Delta E_{V,PVSK\text{-}Spiro\text{-}OMeTAD}$ and we have higher mobility with Spiro-OMeTAD and perovskite with Spiro-OMeTAD. Finally, we selected Spiro-OMeTAD as a HTM layer based on this characterization results [59].

Table 4.2: Effect on mobility of perovskite layer with Spiro-OMeTAD and P3HT.

	P3HT	PVSK with P3HT	Spiro-OMeTAD	PVSK with Spiro-OMeTAD
Mobility, μ (cm^2/V-s)	93.72	122.60	110.90	285.40

4.7 SUMMARY

One step bilayer decreases the surface roughness significantly. Solaronix TiO2 blocking layer shows better result in crystallography and morphology. Spiro-OMeTAD has higher mobility and lower ΔE_V compare to P3HT

Chapter 5: Device Fabrication

5.1 Introduction

The first OMHPs employed in PV were used as direct replacements for the dye sensitizers in the DSSCs. The typical DSSC structure employs a several-micron thick porous TiO_2 layer that is coated and penetrated with an absorber dye material. The electrode assembly is contacted by a liquid electrolyte containing a redox couple. In these devices, TiO_2 is used to collect and transport the electrons, while the electrolyte acts as a hole conductor. The original perovskite solar cells evolved from this same structure, with the OMHP materials acting simply as a dye replacement. Interest increased when the so-called mesoscopic device structure (Figure 5.1(a)) was formed by replacing the liquid electrolyte with a solid-state hole conductor. This advance created great interest in the PV community and drew in experts from the thin-film PV and OPV communities. As a result, planar device structures in which the OMHP absorber is sandwiched between electron and hole transporting materials (ETM and HTM) were developed. Depending on which transport material is encountered by the light first, these planar structures can be categorized as either the conventional n-i-p (Figure 5.1(b)) or the inverted p-i-n (Figure 5.1(c)) structures. Recently, a mesoscopic p-i-n structure (Figure 5.1(d)) has also been developed. Due to processing differences, the device architecture determines the choice of charge transport (ETM and HTM) and collection (cathode and anode) materials, the corresponding material preparation methods, and, consequently, the performance of the devices. To date, no perovskite devices with significant efficiency have been constructed on opaque substrates (e.g., Ti foils) because the conventional deposition technologies for transparent conducting oxides (TCO) may lead to decomposition of the surface of the OMHP [13].

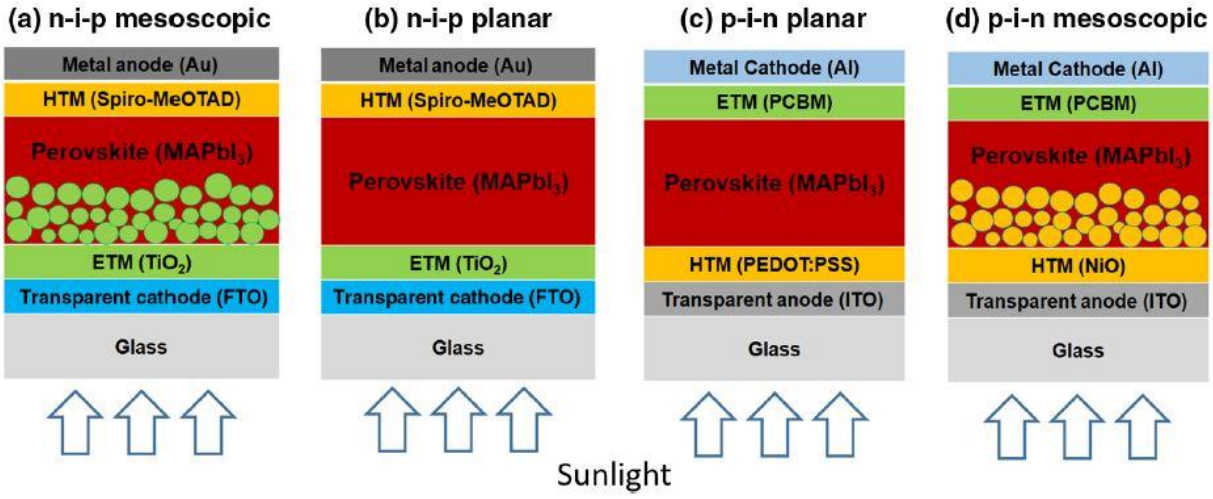

Figure 5.1: Schematic diagrams of perovskite solar cells in the (a) n-i-p mesoscopic, (b) n-i-p planar, (c) p-i-n planar, and (d) p-i-n mesoscopic structures.

In the present work, the planar PSC configuration comprised either (i) FTO-coated glass with a TiO_2 blocking layer or (ii) a nanocrystalline SnO_2 layer with perovskite/spiro-MeOTAD/Ag. There were nine separate solar cells in one sample, and each had an area of 0.159 cm^2. Besides, the planar PSC configuration with multilayer of TiO_2 blocking layer for one step deposition also fabricated to compare the results with others.

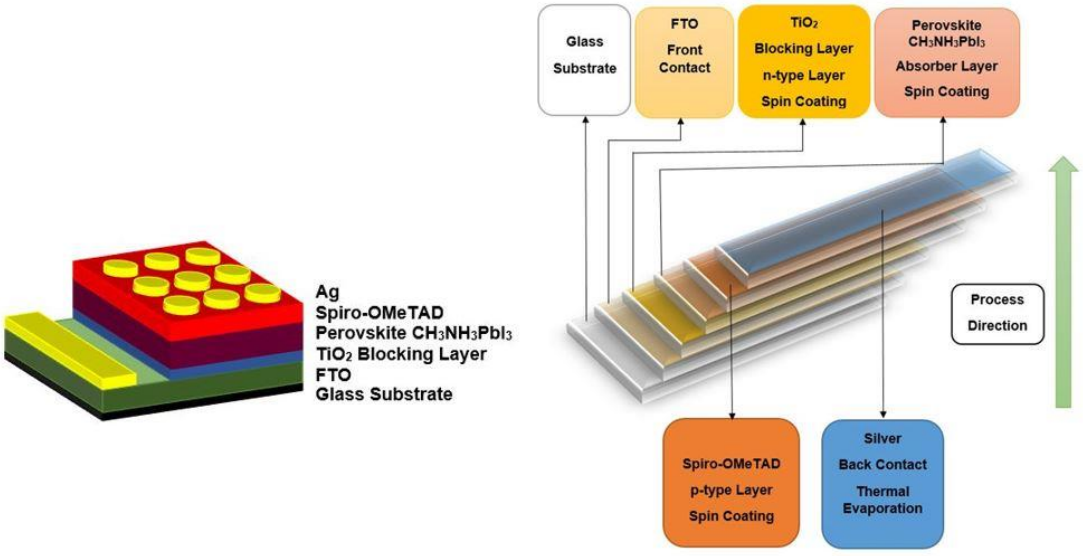

Figure 5.2: 3D structure and device fabrication processes of planar perovskite solar cell with one step deposition.

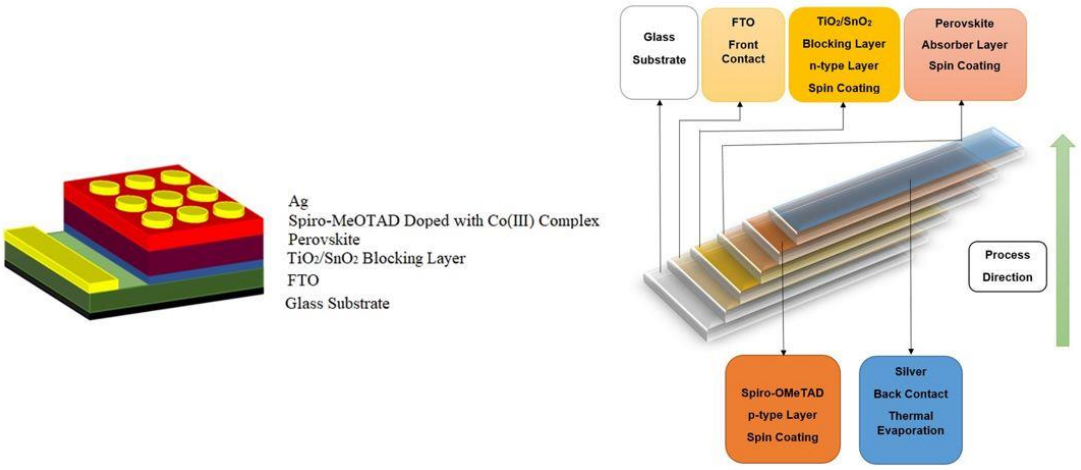

Figure 4.3: 3D structure and device fabrication processes of planar perovskite solar cell with mixed cation solution processing.

5.2 TRANSPARENT CONDUCTING OXIDE (TCO) LAYER

The FTO-coated glass was cut into 1 in × 1 in pieces. To remove hydrocarbons and other contaminants, each piece was cleaned for 30min in a sonication bath containing acetone, de-ionized water, and isopropyl alcohol and then dried with nitrogen gas.

5.3 ETM LAYER

A compact TiO_2 blocking layer was deposited on the cleaned FTO substrate by spin-coating the solution (at 5000 rpm/min for 30 s) and annealing the coated substrates at 550°C for 1 h.

A 0.05-M solution was prepared by dissolving $SnCl_4.5H_2O$ in isopropyl alcohol. After being stirred for 30min at room temperature, the solution was deposited on the cleaned FTO substrates at a spin rate of 3000 rpm for 30 s with a ramp of 200 rpm/s, followed by heat treatment at 180°C for 1 h. SnO_2 layers were grown by chemical-bath deposition on the spin-coated layer. We dissolved 0.5 g of urea in 40ml of de-ionized water and then added 10 µl of mercaptoacetic acid and 0.5 ml of HCl (37wt%). Finally, $SnCl_2.2H_2O$ was dissolved in the solution at 0.012M. The substrates were kept for 3 h at 70°C in a glass petri dish filled with the above solution and placed on a hot plate. The substrates were then rinsed in a sonication bath of

de-ionized water for 2 min to remove any loosely bound material, dried with nitrogen gas, and annealed for 1 h at 180°C [26].

5.5 HTM LAYER

The spiro-OMeTAD was dissolved in chlorobenzene (85mg/ml) supplemented with 20 µl/ml of Li-TFSI (500mg/ml in acetonitrile), 33 µl/ml of tBP, and 1 µl/ml of FK-209 Co (III) TFSI salt (100mg/ml in acetonitrile), and the solution was spin coated onto the films in a nitrogen-filled glovebox at 2000–4000 rpm for 20–30 s [48].

5.6 BACK CONTACT

A 100-nm-thick Ag layer was deposited on the hole-transport layer by thermal evaporation using a physical vapor deposition system (PRO Line PVD 75; Kurt J. Lesker Co.).

5.7 SUMMARY

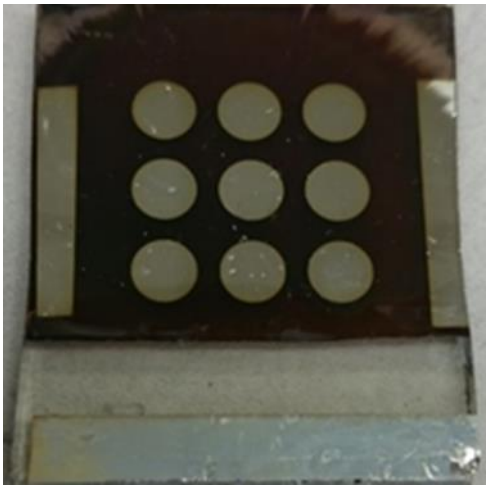

Figure 5.4: Top view after fabricate perovskite solar cells.

We varied the TiO_2 blocking layer thickness by adding multiple layers with one step perovskite. Thickness measurement indicated that 1BL = 118nm, 2BL = 177nm, 3BL = 218nm

and 4BL = 276nm. To make thinner we tried to speed up the speed of the spin coater while deposited the TiO_2 blocking layer with mixed cation perovskite. We changed the ETM layer by replacing TiO_2 with SnO_2.

Chapter 6: Device Characterization

6.1 Introduction

An I-V Measurement System (IV-5) from PV Measurements was used for J–V characterization. QEX10 Solar Cell Quantum Efficiency Measurement System was used for EQE characterization.

6.2 J-V Characterization

6.2.1 One Step Bilayer Deposition Based Planar Perovskite Solar Cells

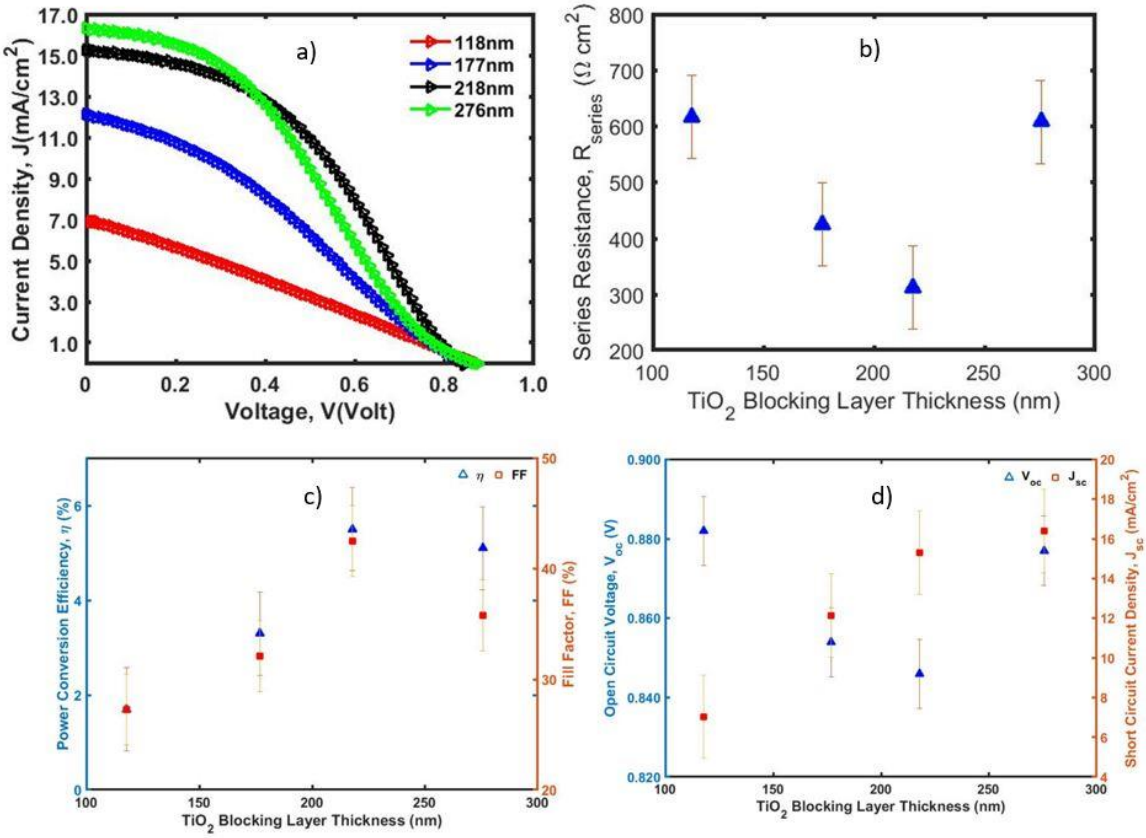

Figure 6.1: (a) Current density vs voltage (J–V) curves of one step planar perovskite solar cells (PSCs) under simulated one-sun AM 1.5G (100 mW/cm^2) illumination with different thicknesses of TiO_2 blocking layer, (b) effect of the TiO_2 film thickness on series resistance (R_{series}) of planar PSCs, (c) effect of the TiO_2 film thickness on open-circuit voltage (V_{oc}) and short-circuit current density (J_{sc}), and (d) effect of the TiO_2 film thickness on power conversion efficiency (PCE) and fill factor (FF).

The best PV performance is achieved when the thickness of the TiO_2 blocking layer is 218 nm, with a V_{oc} value of 0.846 V, a J_{sc} value of 15.3 mA/cm^2, an FF of 42.5%, a PCE of 5.5% and series resistance of 312 Ω-cm^2. Thicker TiO_2 blocking layer, poor quality of one step perovskite are the reason behind having low efficiency.

6.2.2 Mixed Cation Solution Processing Based Planar Perovskite Solar Cells

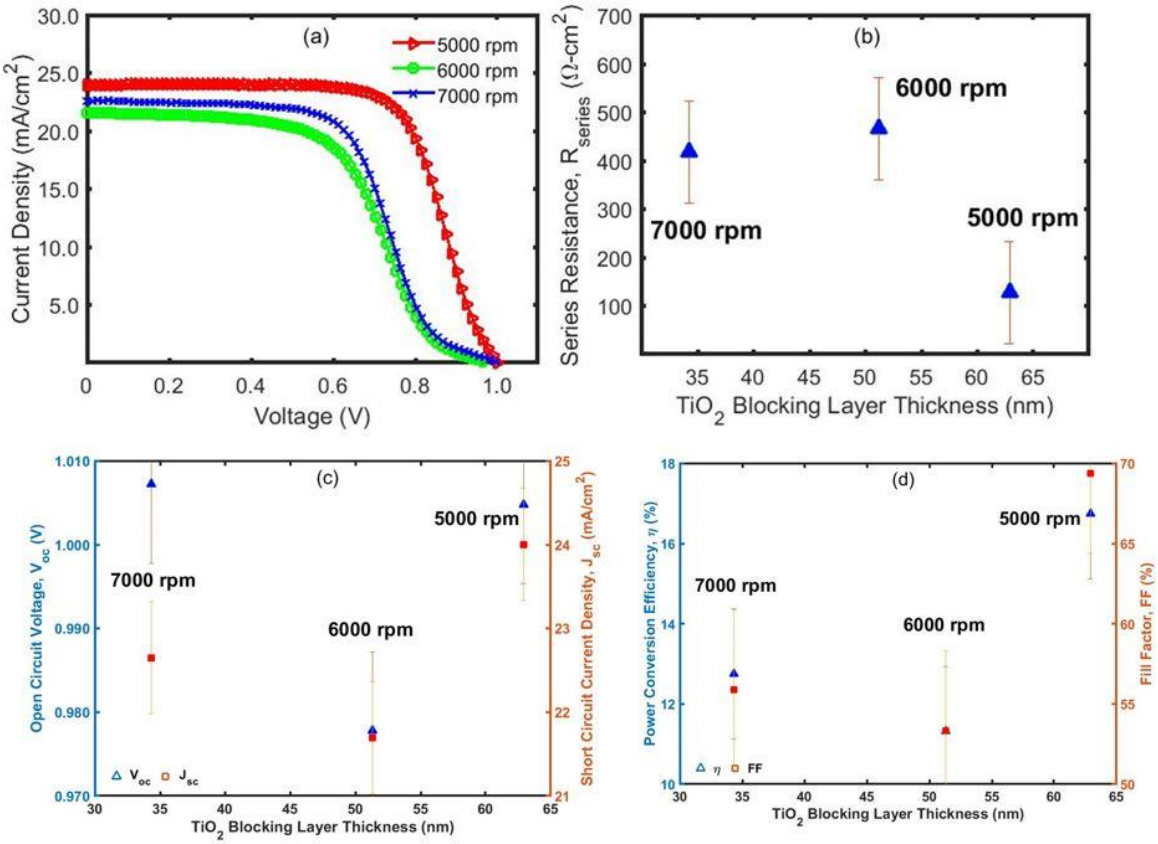

Figure 6.2: (a) Current density vs voltage (J–V) curves of mixed-cation planar perovskite solar cells (PSCs) under simulated one-sun AM 1.5G (100 mW/cm^2) illumination with different thicknesses of blocking layer, which are achieved by varying the speed (5000 rpm, 6000 rpm, and 7000 rpm) of the spin coater while depositing the TiO_2 layer, (b) effect of the TiO_2 film thickness on series resistance (R_{series}) of planar PSCs, (c) effect of the TiO_2 film thickness on open-circuit voltage (V_{oc}) and short circuit current density (J_{sc}), and (d) effect of the TiO_2 film thickness on power conversion efficiency (PCE) and fill factor (FF).

The best PV performance is achieved when the thickness of the TiO_2 blocking layer is 60–65nm, with a V_{oc} value of 1.01V, a J_{sc} value of 24mA/cm^2, an FF of 69.40%, and a PCE of

16.74%. As a blocking layer, the compact TiO_2 film inhibits electron–hole recombination at the interface between the FTO and the perovskite. Reducing the thickness of the compact TiO_2 layer is a simple strategy for improving electron transport to the transparent conductive oxide layer by shortening the pathway within the low-conductive TiO_2 layer. To be an efficient electron-transport layer, the compact TiO_2 layer should be as thin as possible while retaining its hole-blocking effectiveness. However, a too thin TiO_2 blocking layer corresponds to a large series resistance (Rseries) and low FF (Figure 6.2). Figure 6.2(a) shows the current density vs voltage (J–V) curves of mixed-cation planar perovskite solar cells (PSCs) under simulated one-sun AM 1.5G (100 mW/cm^2) illumination with different thicknesses of blocking layer. In addition, a significant reduction of short circuit current J_{sc} is observed for thinner TiO_2 blocking layers.

6.3 DARK J-V CHARACTERIZATION

6.3.1 One Step Bilayer Deposition Based Planar Perovskite Solar Cells

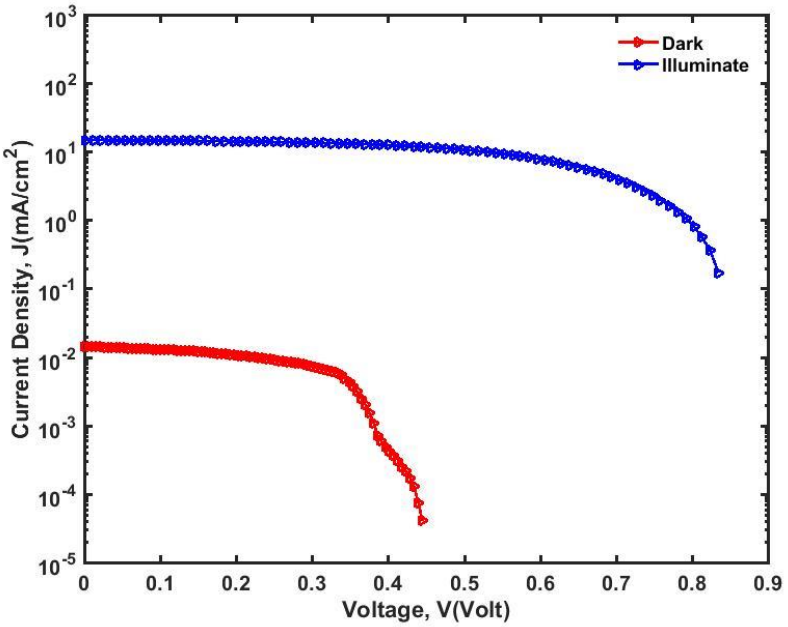

Figure 6.3: Illuminate and dark current density-voltage (J-V) curves of one step deposition based perovskite solar cells.

Figure 6.1(a) shows a double diode behavior. To explore the origin of this feature, we investigated the dark J-V characteristics of PSCs. Figure 6.3 shows in the depletion region electron hole pairs recombination occur twice. It decrease the lifetime of electron hole pairs and eventually decrease the efficiency. Illuminated current is 1000 times higher than dark current.

6.3.2 Mixed Cation Solution Processing Based Planar Perovskite Solar Cells

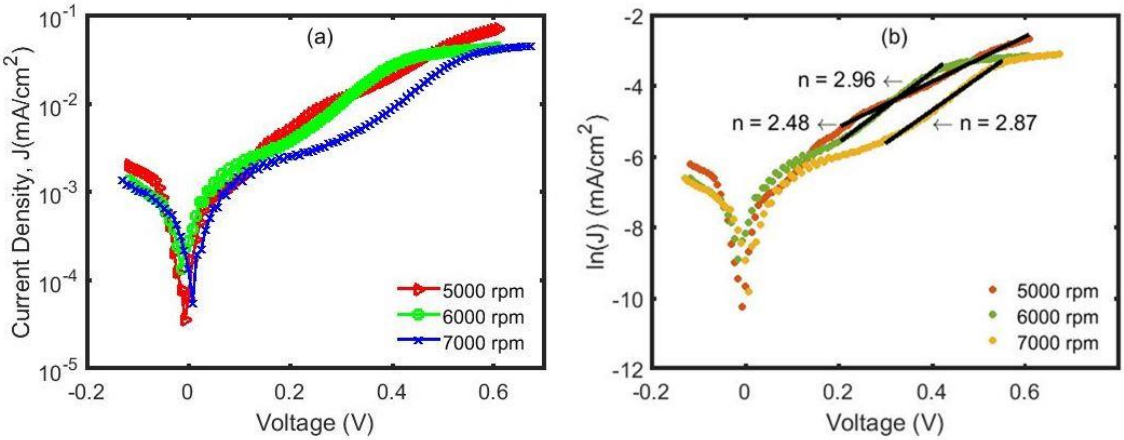

Figure 6.4: Current density vs voltage (J–V) curves in the dark for different thicknesses of blocking layer with (a) semi logarithmic scale to identify the recombination mechanism and (b) natural-log scale to calculate the diode ideality factors (n) (the lines are fitted to the Shockley diode equation).

$$Shockley\ diode\ equation, J = J_0[\exp\left(\frac{qV}{nKT}\right) - 1] \quad (6.1)$$

Here,

J_0 = The dark saturation current density (mA/cm^{-2})

V = Applied bias (V)

Q = Elementary charge (c)

n = Ideality factor of the diode

K = Boltzmann's constant (eV) and

T = Absolute temperature (K)

$$\ln(J) = \ln(J_0) + \frac{qV}{nKT} \tag{6.2}$$

Figure 6.2(a) shows a double diode behavior. To explore the origin of this feature, we investigated the dark J-V characteristics of PSCs. Figure 6.4(a) shows the current density vs voltage (J–V) curves in the dark for different thicknesses of blocking layer with a semi-logarithmic scale. Analysis of the dark current from these devices confirms the qualitative analysis of the illuminated J–V measurement. The dark current is dominated by carrier recombination in perovskites for a low bias regime. The high bias current is limited by space-charge effects. The recombination takes place during exciton diffusion. Exciton diffusion takes place during the geminate recombination, and the charge collection is dominated by recombination and space charge effects. Both types of recombination processes cause the charge carrier loss in the device. Due to these losses, the ideality factor of the device increases beyond unity, sometimes greater than 3 [49]. Increasing values of the ideality factor have been considered the signature of increased recombination loss or increased disorder in the electronic states. Trap assisted non radiative recombination via defect states in the bandgap is of high importance since the greatest proportion of carriers is often lost in this way. The ideality factor of the cell is derived from the slope of the linear fitting results of dark current density-voltage curves. The dark current is governed by a low parasitical leakage current at very low voltages, with a transition to a steep increase of the current above approximately 0.2 V. The steep increment of the current results from a diffusion-dominated current, typically described by the Shockley diode equation Eq. (6.1). The thicker TiO_2 based PSC has the lowest ideality factor of n = 2.48, which is the lowest recombination among the three samples. As the ideality factor increases, the device series resistance also increases. A linear characteristic is observed in the high bias regime, thus confirming space charge limiting current. The “-1” term can be ignored for V > 50 - 100 mV and taking the natural log of both sides of Eq. (6.1) gives Eq. (6.2).

According to Eq. (6.2), the ideality factor of the cell is derived from the slope of the linear fitting results of dark current density-voltage curves. Lines are indicating the slopes for the ideality factor.

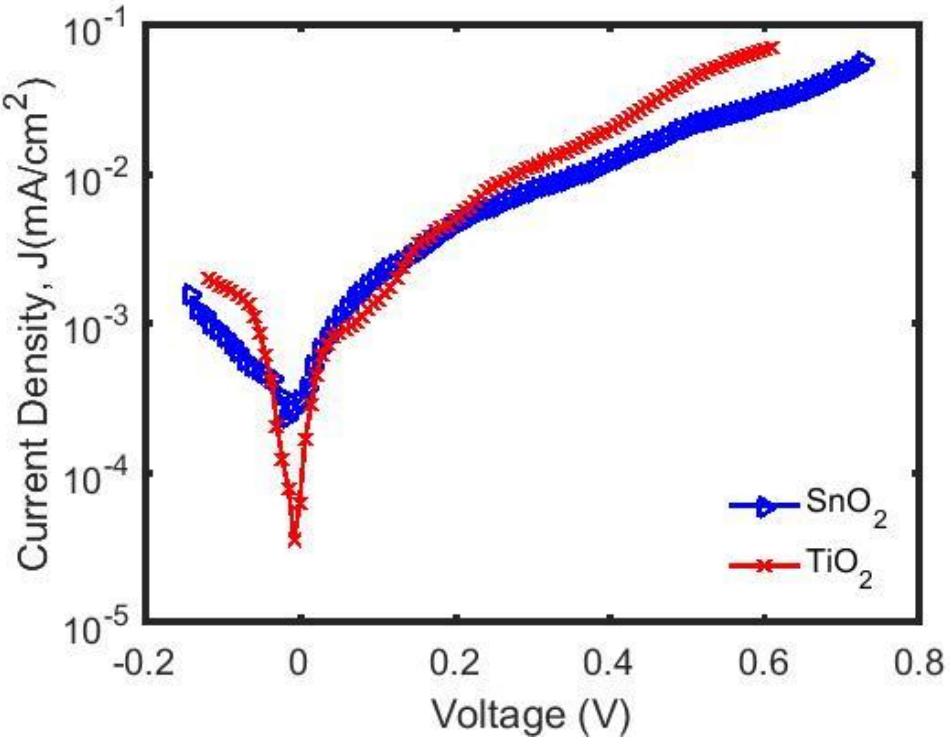

Figure 6.5: Current density vs voltage (J–V) curves in the dark for different electron transport layers with the semi logarithmic scale to identify the recombination mechanism.

Figure 6.5 shows current density vs voltage (J–V) curves in the dark for TiO_2 and SnO_2 based PSCs with a semi logarithmic scale. In the high voltage region, the SnO_2 based PSC has lower dark current density. The lower dark current indicates that it could prevent current leakage, which is beneficial for the improvement of J_{sc} and FF which are observed in Figure 6.2(a) and 6.2(b). In a PSC, the quality of a junction and the carrier recombination mechanism can be represented by the values of the ideality factor. There is no double diode behavior observed for the SnO_2 based PSC. However, the Shockley-Read-Hall (SHR) band to band (low level injection) recombination does occur in this device. The TiO_2 based PSC has a high ideality factor because depletion region (junction) recombination and trap-assisted nonradiative recombination

have taken place. In a dark condition, the SnO_2 based PSC (Rsh = 2.58×10^4 Ω-cm^2) has larger shunt resistance than the TiO_2 based PSC (Rsh = 9.19×10^3 Ω-cm^2). The better quality of the junction and the enhancement of R_{sh} can decrease the current leakage, which is observed in Figure 6.5.

6.4 J-V COMPARISON BETWEEN TiO_2 AND SnO_2 BASED PLANAR PEROVSKITE SOLAR CELLS

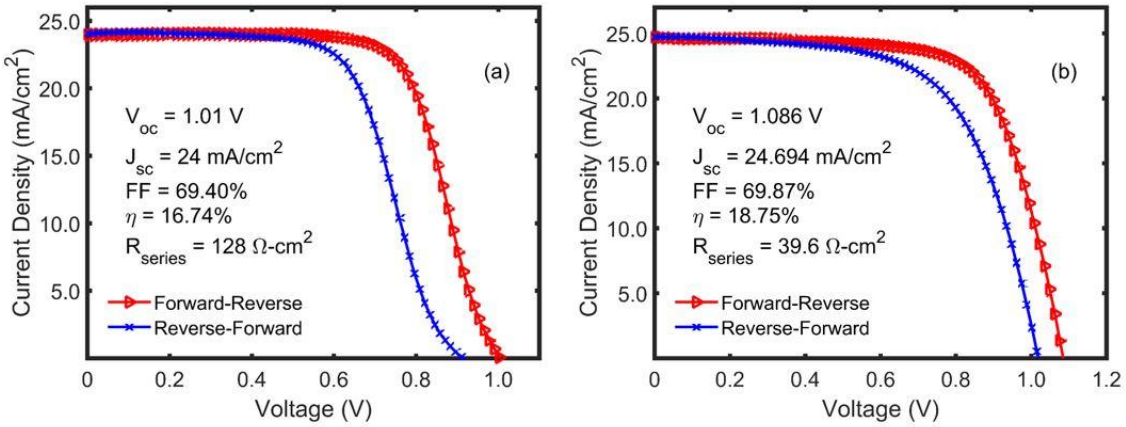

Figure 6.6: Current density vs voltage (J–V) curves from forward and reverse scans of mixed-cation planar PSCs based on (a) spin-coated TiO_2 with a thickness of 60–65 nm and (b) spin-coated SnO_2 as an electron-transport layer.

SnO_2 has a high mobility, wide bandgap, and deep conduction band and valence band. SnO_2 shows better optical and electric properties, band alignment to perovskite, and stability than the traditional TiO_2. Its excellent optical transparency in the visible region is highly desired to fabricate highly efficient PSCs. SnO_2 has 100 times higher electron mobility (up to 240 cm^2/V s) [50]. This high electron mobility of SnO_2 helps it to extract electrons from the perovskite effectively. The SnO_2 layer has a favorable conduction band (CB) alignment with the perovskite, whereas the TiO_2 layer possessed a mismatch CB alignment with the perovskite. The good band alignment of SnO_2 with the perovskite layer ensures a high quality of the p–n heterojunction. Juan Pablo Correa Baena et al. showed that by transient absorption measurements, the mixed $(FAPbI_3)_{0.85}(MAPbBr_3)_{0.15}$ perovskite materials extract charges efficiently into SnO_2 but not into TiO_2 for conduction band misalignment at the TiO_2/perovskite interface [51]. A barrier-free

charge transport across the SnO_2/perovskite interface gives rise to high and stable current densities. To investigate the influence of different ETLs on charge transfer and charge recombination of the device, they measured the transient photocurrent decay under the short circuit condition and photo voltage decay under the open-circuit condition. TiO_2 decays faster than SnO_2 in both cases. The results clear indicate a barrier free charge transport across the perovskite/SnO_2 in contrast to the perovskite/TiO_2 interface. Studies showed that higher built-in-potential of the SnO_2/perovskite heterojunction could be obtained, compared to TiO_2 based devices, which then retarded charge recombination and thus increased both the V_{oc} value and the fill factor (FF) [52]. Figures 6.6(a) and 6.6(b) show that SnO_2 based PSC has 76mV and 0.47% higher V_{oc} and FF, respectively. The high quality of the SnO_2/perovskite heterojunction implies improved electric parameters such as series resistance (R_s). The improvement in R_s from 128 Ω-cm^2 to 39.6 Ω-cm^2 is a sign of suppression of carrier recombination at the SnO_2/perovskite interface, leading to an apparent increase in V_{oc} of the SnO_2 devices. Liangbin Xiong et al. showed that the photoluminescence (PL) quenching is expected to originate from the charge-carrier extraction across the interface [53]. The PL quantum yield is reduced when the perovskite is interfaced with SnO_2 and TiO_2 electron transport layers (ETLs). The lowest PL peak for SnO_2/perovskite suggests the highest quenching efficiency and thus the highest electron extraction efficiency. The Time-Resolved Photoluminescence (TRPL) decay of the SnO_2/perovskite interface is shorter than the TiO_2/perovskite interface, indicating that charge carriers within the perovskite layer can be separated more effectively and faster extraction and transfer by SnO_2 compact layers. That is why the SnO_2-based PSC has better photovoltaic performance than the TiO_2 based PSC.

$$Hysteresis\ index, HI = \frac{J_{RS}(0.8V_{OC}) - J_{FS}(0.8V_{OC})}{J_{RS}(0.8V_{OC})} \tag{6.3}$$

Current density vs voltage (J-V) measurements [Figs. 6(a) and 6(b)] have shown that both compact-TiO_2(c-TiO_2)-based and SnO_2-based devices suffer from a hysteresis when scanned under forward and reverse bias conditions. The c-TiO_2-based devices also suffer significantly from low electron mobility, which leads to insufficient charge separation at the c-TiO_2/perovskite interface. The creation of surface charge traps adversely affects the charge transfer processes at the TiO_2/perovskite interface. Under short-circuit conditions, the traps may empty due to charge transfer directly to the p- and n-type contacts, resulting in poor operation until the traps are filled once again. The crystal size of the PSC and the thickness of TiO_2 films are responsible for influencing the JV hysteresis. Hysteresis index (HI) values are calculated with photovoltaic parameters depending on the scan direction. A J-V HI is defined by the equation of 6.3 where $J_{RS}(0.8V_{oc})$ and $J_{FS}(0.8V_{oc})$ represent the photocurrent density at 80% of V_{oc} for the RS (forward to reverse scan) and FS (reverse to forward scan), respectively [54]. 5000 rpm of the TiO_2 based PSC shows the smallest HI of 0.3155 among the three TiO_2 based samples. 0.8586 and 0.5277 HIs are calculated for 6000 rpm and 7000 rpm of TiO2 samples. In addition, the SnO_2 based PSC gives the lowest HI of 0.1437. High mobility, low trap states at the SnO_2/perovskite interface, faster charge extraction, and charge transfer are the main causes to get the lowest HI.

6.5 POWER CONVERSION EFFICIENCY (PCE) HISTOGRAMS

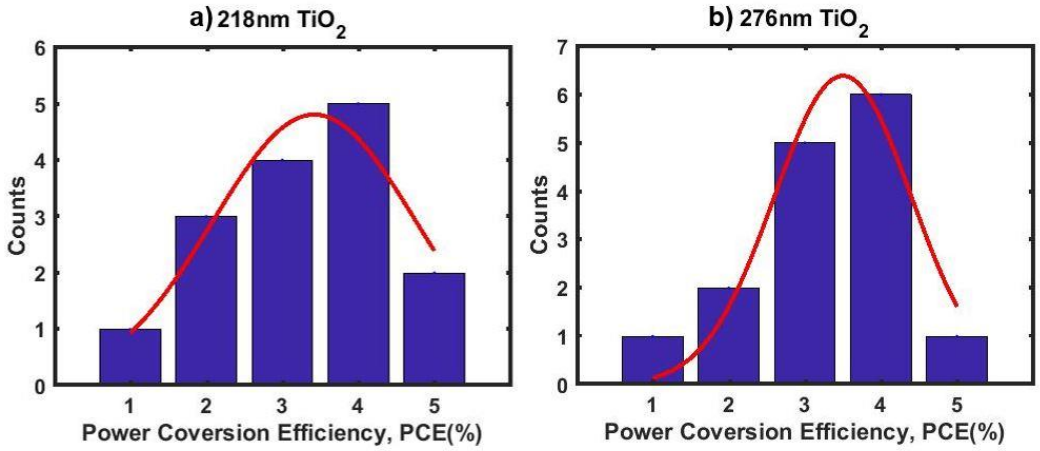

Figure 6.7: Histogram of PCE measured from 15 one step deposition based devices, which shows an average PCE of a) 3.5% with 3BL and b) 3.5% with 4BL.

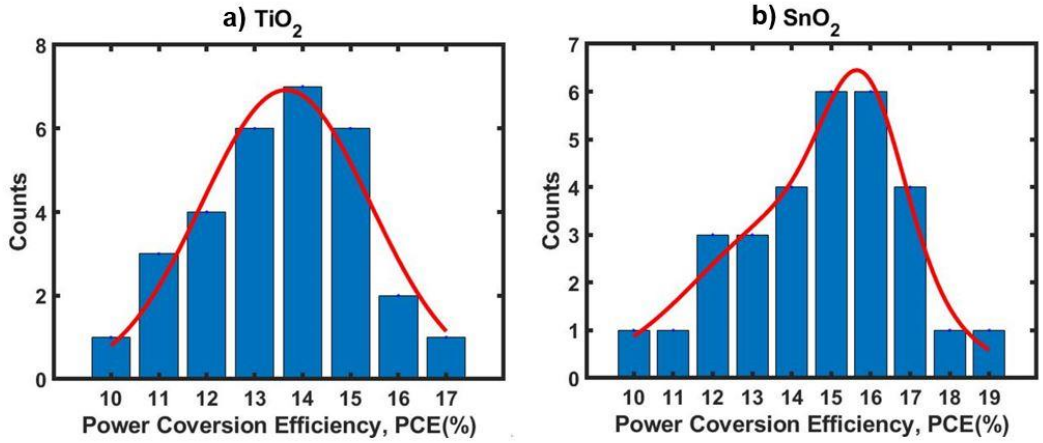

Figure 6.8: Histogram of PCE measured from 30 mixed cation based devices, which shows an average PCE of a) 13.5% with TiO_2 and b) 15.7% with SnO_2.

A better ETL and a comparatively good quality of FA/MA mixed cation perovskites achieved average PCE of 15.7% with SnO_2.

6.6 EXTERNAL QUANTUM EFFICIENCY (EQE)

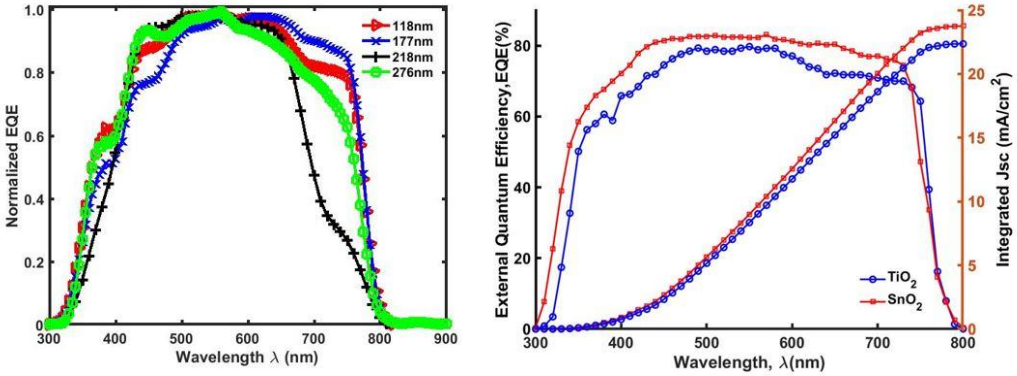

a) One step deposition b) Mixed cation solution processing

Figure 6.9: External quantum efficiency and the integrated current density of the perovskite solar cells

$$J_{SC} = -q \int_{300\ nm}^{800\ nm} EQE(\lambda) \times \Phi_{ph}^{AM\ 1.5}(\lambda) \times \frac{\lambda}{1240} \quad (mA/cm^2) \tag{6.4}$$

Here,

EQE = External Quantum Efficiency

$\phi_{ph}^{AM\ 1.5}(\lambda) =$ *spectral irradiance of AM 1.5 G spectrum at 1 sun solar intensity* $(W/cm^2/nm)$

λ/1240 = Wavelength (nm)/ 1240 (eV- nm)

Figure 6.9(a) shows surface recombination in the blue light wavelength region. Mismatch of conduction energy band between TiO_2 and one step perovskite is the reason behind it. Poor quality of perovskite decreases EQE after 600 nm wavelength mostly it was happed higher recombination and lower diffusion length. Figure 6.9(b) shows improved surface recombination and increased EQE compare to TiO_2 because SnO_2 is a better ETL and a comparatively good quality of FA/MA mixed cation perovskites. Integrated current density can be calculate by Eq. 6.4 [55]. Results shows both J_{sc} are almost close in values.

6.7 SUMMARY

The power conversion efficiency (PCE) of 16.74% is achieved when the thickness of the TiO_2 blocking layer is 63 nm with V_{oc} = 1.01 V, J_{sc} = 24 mA/cm^2, FF = 69.40%, and R_{series} = 128 Ω-cm^2. The best photovoltaic performance is achieved by SnO_2 based mixed cations perovskite solar cell with V_{oc} = 1.086 V, J_{sc} = 24.694 mA/cm^2, FF = 69.87%, PCE = 18.74% and R_{series} = 39.6 Ω-cm^2. There is no double diode behavior observed for the SnO_2 based PSC 63nm TiO_2 blocking layer sample has the lowest ideality factor of 2.48. Increased recombination loss or increased disorder in the electronic states and trap assisted nonradiative recombination via defect states in the bandgap are the main reason for high ideality factor. SnO_2 based PSC has the lowest hysteresis index of 0.1437 because of the high mobility of SnO_2, low trap states at the SnO_2/perovskite interface, faster charge extraction and charge transfer at the SnO_2/perovskite interface. PCE histograms for TiO_2 shows average of 13.5% PCE and SnO_2 shows average of 15.5% PCE among 30 perovskite solar cells. SnO_2 based PSC has lower front surface recombination and after 550 nm wavelength TiO_2 based PSC has significantly lower EQE because of low diffusion length and higher trap assisted nonradiative recombination via defect states in the bandgap.

Chapter 7: Degradation

7.1 Introduction

The first step towards improving perovskite solar cell stability is to understand the exact causes of their instabilities. Many things can cause the perovskite crystal to undergo degradation, and these factors can broadly be split into two categories - extrinsic and intrinsic factors. Ambient humidity can cause rapid degradation of perovskite films, especially in MAPbI3. The rate of deterioration will increase when high humidity is combined with UV light, high temperatures, or the application of an electric field. The organic cations used in perovskite solar cells are very hygroscopic means tending to absorb moisture from the air. It has been suggested that water molecules form weak hydrogen bonds with the cations and that this compromises the structural stability of the crystal. This can lead to the formation of a hydrated perovskite phase. This change is reversible. However, it has been suggested that with enough moisture penetration, the perovskite crystal decomposes. Shown below are a chain of reactions that could be responsible for non-reversible degradation in $MAPbI_3$ perovskites.

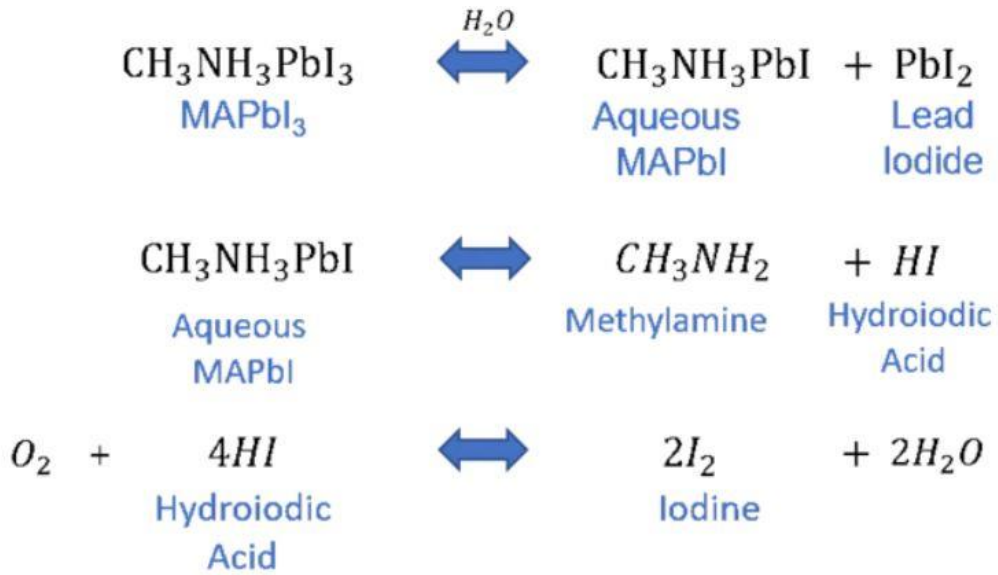

Figure 7.1: Chain of reactions from $MAPbI_3$ perovskites, catalyzed by water.

This illustrates the conversion of $MAPbI_3$ to an aqueous form of methylammonium lead iodide (MAI) and lead iodide (PbI_2). From this, hydroiodic acid (HI) and methylamine are

produced. In the presence of oxygen, more water is then produced. This creates a cyclic process leading to further moisture degradation. The presence of excess PbI_2 can also influence the formation of the perovskite active layer. One way to reduce this effect is to increase the strength of the bonds between the organic component and the metal halides. It is extremely important that active layers are deposited in an environment where humidity is controlled. Hydrophobic (means tending to repel or fail to mix with water interlayers) can also be introduced to help protect the perovskite from ambient moisture [56].

The effect of UV light on perovskite solar cell stability is most significant when combined with other factors (e.g. moisture or oxygen exposure). However, it has been shown that $MAPbI_3$ will degrade to PbI_2 under UV light without moisture or oxygen present.

Exposure to elevated temperatures can cause degradation. This is seen in both $MAPbI_3$ and $MAPbCl_xI_{(3-x)}$. It is thought that PbI_2 can form from $MAPbI_3$ at elevated temperatures. This can happen without oxygen or water present, but at a much slower rate (compared to when oxygen and water are present).

Another layer that has a huge impact on a solar cell's functionality is the hole-transport layer (HTL). Perovskite solar cells can have inorganic HTLs (e.g. P3HT) and organic HTLs (e.g. Spiro-OMeTAD). However, there is a trade-off between the two. Spiro-OMeTAD is an effective HTL, but it needs two additives to give it suitable HTL properties. It has been suggested that this doped Spiro-OMeTAD layer does not form the necessary barrier to protect the perovskite from external factors (air, moisture etc.). An alternative is the organic P3HT, which creates a more stable solar cell. Unfortunately, these cells have lower efficiencies. The impact of different transport layers on device performance is discussed more thoroughly in Wang et al.'s 2016 study [57].

During perovskite film formation, it is common that there are vacancies in the perovskite structure. These are defects and can encourage ion migration through the perovskite film. Ion migration within the perovskite layer can lead to the poor or fluctuating performance of a PV

device. For example, a reaction between hole-transport layer Spiro-OMeTAD and migrating iodine ions can reduce the HTL's conductivity. This quickly hampers the performance of the perovskite solar cell. It has been suggested that this ion migration can lead to the formation of a local electric field at the perovskite material interface. This can lead to deprotonation of the organic cations, and ultimate deterioration of the perovskite solar cell. Migration of perovskite material is not the only thing that causes problems. Ions from conductive contacts can migrate through the perovskite layer. This creates shunt pathways for electrons, short-circuiting the solar cell [57].

$$Tolerance\ factor, t = \frac{r_A + r_X}{\sqrt{2}(r_B + r_X)} \tag{7.1}$$

Here,

r_A = The radius of the A cation

r_B = The radius of the B cation and

r_X = The radius of the anion

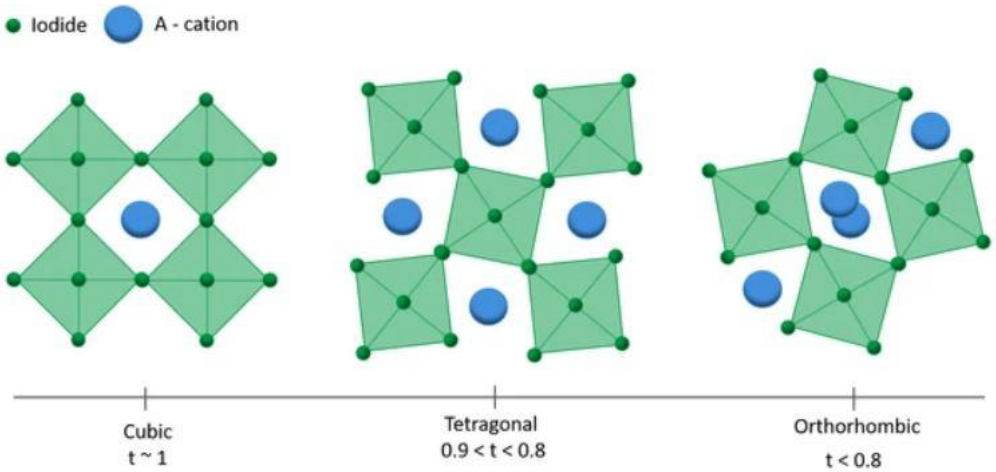

Figure 7.2: Possible crystal phases of perovskites depending on tolerance factor.

The organic cation has little impact on the electrical properties or band structure of the perovskite layer. Its main role is to balance charge within the crystal structure. However, the size

of the “A-cation” can have a noticeable effect on lattice structure. The subsequent size of the B-X bond can also affect the band gap and stability of a perovskite solar cell. Therefore, by varying the ratios of A-cations in the precursor, lattice qualities can be tuned/altered. The suitability of an A-cation for use in a perovskite structure is determined by its tolerance factor (t).

Different cation sizes can result in lead halide octahedral distortion and tilting. If this tilting is significant, it can shift the phase of the perovskite crystal into an undesirable state for photovoltaic activity. This is represented by the tolerance factor. If the tolerance factor is 1, then this produces a cubic perovskite structure. However, if the tolerance value falls between 0.7 and 0.9, then the tetragonal or orthombic phases can be induced. $MAPbI_3$ is tetragonal at room temperature. Formamidinium (FA) has been used as an alternative to MA since it is a similar size to methylammonium. However, due to its high tolerance factor, formamidinium lead iodide ($FAPbI_3$) exists in a non-perovskite hexagonal phase at room temperature. Although a black perovskite phase can be achieved by heating, this non-perovskite phase becomes more significant over time and limits the stability of a device. This can be compensated by introducing smaller inorganic cations into the perovskite, such as cesium (Cs) and rubidium (Ru). The addition of a small amount of Cs into FA-based perovskites assists the crystallisation of the “black perovskite” phase [58].

7.2 ONE STEP DEPOSITION

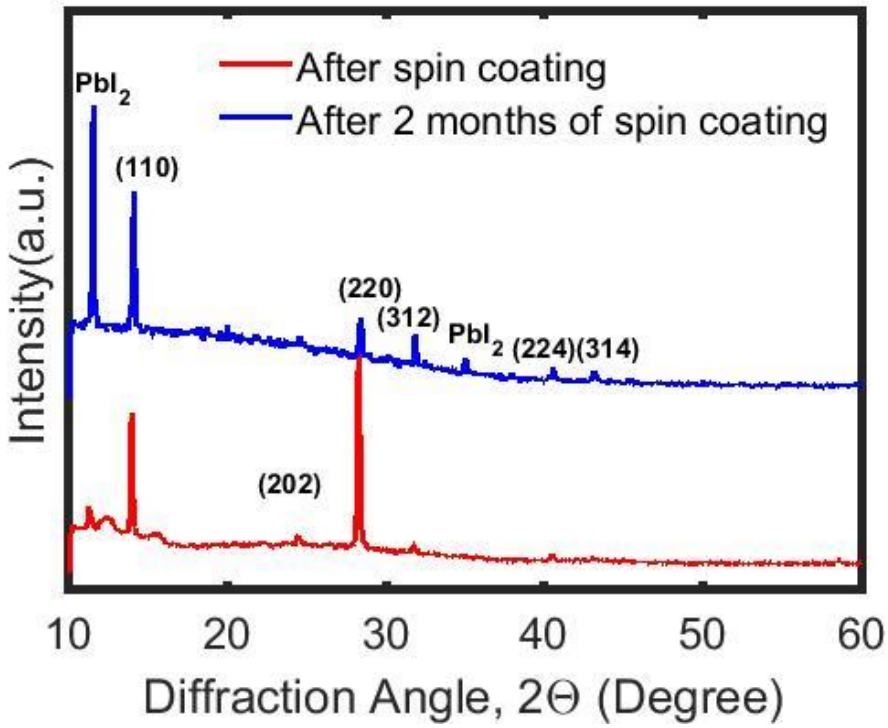

Figure 7.3: XRD patterns shows distinct peak of PbI_2 after two months of spin coating.

After two months, high intensity PbI_2 showed up which indicate the chain reaction was occurred in the presence of moisture.

7.3 TWO STEPS DEPOSITION

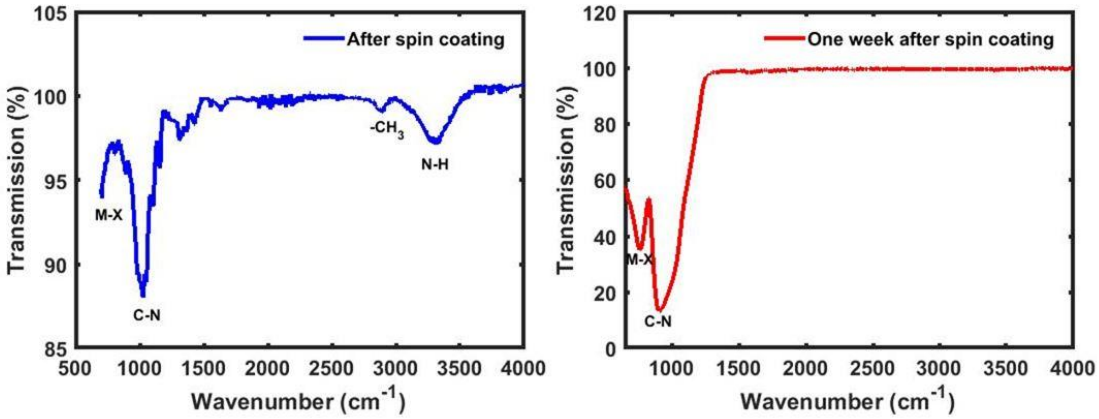

a) Fresh batch after spin coating b) One week after spin coating

Figure 7.4: FTIR spectra of the perovskite.

FTIR indicates that after one week the sample loosing C-H, N-H bonds due to moisture reaction which triggered the chain reaction and degrade the perovskite.

7.4 MIXED CATION SOLUTION PROCESSING

Table 7.1: Calculated degradation rate after 100 hours.

	Voc (V)	Jsc (mA/cm^2)	FF (%)	η (%)	Rserise (ohm-cm^2)	Degrade (%)	
Fresh	1.01	24	69.4	16.74	127.94	2.03	**TiO_2**
100 Hours	0.944	23.83	62.6	16.4	133.19		
Fresh	1.086	24.76	69.9	18.75	39.57	1.33	**SnO_2**
100 Hours	1.02	24.69	66.4	18.5	42.25		

Table 7.1 shows the percentage of degradation on PCE after 100 h. The TiO_2 based PSC degrades 2.03% PCE, whereas the SnO_2 based PSC degrades only 1.33%. A better ETL and a comparatively good quality of FA/MA mixed cation perovskites make a difference.

7.5 SUMMARY

One step degradation rate is slower than two steps. The TiO_2 based PSC degrades 2.03% PCE, whereas the SnO_2 based PSC degrades only 1.33%. To get an alpha phase perovskite we need tolerance factor 1 because it is more stable.

Chapter 8: Conclusion

In conclusion, the XRD results show a secondary phase of PbI_2 for the SSE and Two steps method. One step has the highest crystallite size of 40 nm besides mixed cations has 38 nm. The SEM results confirm that the one-step deposition exhibited pinhole formation, loosely packed grains and incomplete coverage. The SSE, Two steps and Mixed-cations samples have small grains and closely and neatly packed films with minimum pinhole formation and a good coverage area. One step has the best average grain diameter of 373.26 nm however mixed cation has 244.74 nm. Mixed-cations sample exhibits the lowest shift in XPS results among all the samples. Mixed cation has higher optical absorption into the red to enhance solar light harvesting. All samples have high absorption co-efficient (10^5 cm^{-1}) and 300 nm to 500 nm thickness range for 1.58 to 1.6 eV bandgap. Mixed cations sample has the highest urbach energy, Eu = 149 meV. The higher Eu defines the high disorder of phonon states in the film. One step has the highest lifetime of 216.04 ns where mixed cations has 21.14 ns because of higher disorder of phonon states. Finally, based on the results, the mixed-cation sample shows the most promising results for a high performance planar structure perovskite solar cell. The power conversion efficiency (PCE) of 16.74% is achieved when the thickness of the TiO_2 blocking layer is 63 nm with V_{oc} = 1.01 V, J_{sc} = 24 mA/cm^2, FF = 69.40%, and R_{series} = 128 Ω-cm^2. The best photovoltaic performance is achieved by SnO_2 based mixed cations perovskite solar cell with V_{oc} = 1.086 V, J_{sc} = 24.694 mA/cm^2, FF = 69.87%, PCE = 18.74% and R_{series} = 39.6 Ω-cm^2. There is no double diode behavior observed for the SnO_2 based PSC 63nm TiO_2 blocking layer sample has the lowest ideality factor of 2.48. Increased recombination loss or increased disorder in the electronic states and trap assisted nonradiative recombination via defect states in the bandgap are the main reason for high ideality factor. SnO_2 based PSC has the lowest hysteresis index of 0.1437 because of the high mobility of SnO_2, low trap states at the SnO_2/perovskite interface, faster charge extraction and charge transfer at the SnO_2/perovskite interface. PCE histograms for TiO_2 shows average of 13.5% PCE and SnO_2 shows average of 15.5% PCE

among 30 perovskite solar cells. SnO_2 based PSC has lower front surface recombination and after 550 nm wavelength TiO_2 based PSC has significantly lower EQE because of low diffusion length and higher trap assisted nonradiative recombination via defect states in the bandgap.

In future work, I want to do simulation work to find out new material which will be more stable and toxic free material. SCAPS (a Solar Cell Capacitance Simulator) will help me to optimize the thickness of the device to improve the efficiency. VASP (Vienna Ab initio Simulation Package) will help me to find out the nature of the crystallography and tolerance factor, DOS, optical and electronic properties of the material. TMM (Transfer Matrix Method) will give as the absorbance, transmittance and reflectance which can be used to find out the absorption coefficient. Finally, fabricate flexible solar cell with the new stable perovskite and do mechanical stability tests to find out the effects on it.

References

[1] Green, M. A., Emery, K., Hishikawa, Y., Warta, W., & Dunlop, E. D. (2015). Solar cell efficiency tables (Version 45). Progress in photovoltaics: research and applications, 23(1), 1-9.

[2] Taguchi, M., Yano, A., Tohoda, S., Matsuyama, K., Nakamura, Y., Nishiwaki, T., & Maruyama, E. (2013). 24.7% record efficiency HIT solar cell on thin silicon wafer. IEEE Journal of Photovoltaics, 4(1), 96-99.

[3] Yan, J., & Saunders, B. R. (2014). Third-generation solar cells: a review and comparison of polymer: fullerene, hybrid polymer and perovskite solar cells. Rsc Advances, 4(82), 43286-43314.

[4] Parisi, M. L., Maranghi, S., & Basosi, R. (2014). The evolution of the dye sensitized solar cells from Grätzel prototype to up-scaled solar applications: A life cycle assessment approach. Renewable and Sustainable Energy Reviews, 39, 124-138.

[5] Kojima, A., Teshima, K., Shirai, Y., & Miyasaka, T. (2009). Organometal halide perovskites as visible-light sensitizers for photovoltaic cells. Journal of the American Chemical Society, 131(17), 6050-6051.

[6] NREL, N. (2019). Best Research-Cell Efficiency Chart.

[7] Scott, V., Haszeldine, R. S., Tett, S. F., & Oschlies, A. (2015). Fossil fuels in a trillion tonne world. Nature Climate Change, 5(5), 419-423.

[8] Ginley, D. S., & Cahen, D. (Eds.). (2011). Fundamentals of materials for energy and environmental sustainability. Cambridge university press.

[9] Denholm, P., Kulcinski, G. L., & Holloway, T. (2005). Emissions and energy efficiency assessment of baseload wind energy systems. Environmental science & technology, 39(6), 1903-1911.

[10] Di, D., Musselman, K. P., Li, G., Sadhanala, A., Ievskaya, Y., Song, Q., & Friend, R. H. (2015). Size-dependent photon emission from organometal halide perovskite nanocrystals embedded in an organic matrix. The journal of physical chemistry letters, 6(3), 446-450.

[11] Xing, G., Mathews, N., Lim, S. S., Yantara, N., Liu, X., Sabba, D., & Sum, T. C. (2014). Low-temperature solution-processed wavelength-tunable perovskites for lasing. Nature materials, 13(5), 476.

[12] Kasap, S. O. (2006). Principles of electronic materials and devices (Vol. 2). New York: McGraw-Hill.

[13] Song, Z., Watthage, S. C., Phillips, A. B., & Heben, M. J. (2016). Pathways toward high-performance perovskite solar cells: review of recent advances in organo-metal halide perovskites for photovoltaic applications. Journal of Photonics for Energy, 6(2), 022001.

[14] Sahoo, S. K., Manoharan, B., & Sivakumar, N. (2018). Introduction: Why Perovskite and Perovskite Solar Cells? In Perovskite Photovoltaics (pp. 1-24). Academic Press.

[15] Akhtar, J., Aamir, M., & Sher, M. (2018). Organometal Lead Halide Perovskite. In Perovskite Photovoltaics (pp. 25-42). Academic Press.

[16] Fakharuddin, A., De Rossi, F., Watson, T. M., Schmidt-Mende, L., & Jose, R. (2016). Research Update: Behind the high efficiency of hybrid perovskite solar cells. APL Materials, 4(9), 091505.

[17] Im, J. H., Lee, C. R., Lee, J. W., Park, S. W., & Park, N. G. (2011). 6.5% efficient perovskite quantum-dot-sensitized solar cell. Nanoscale, 3(10), 4088-4093.
[18] Kim, H. S., Lee, C. R., Im, J. H., Lee, K. B., Moehl, T., Marchioro, A., & Grätzel, M. (2012). Lead iodide perovskite sensitized all-solid-state submicron thin film mesoscopic solar cell with efficiency exceeding 9%. Scientific reports, 2, 591.
[19] Lee, M. M., Teuscher, J., Miyasaka, T., Murakami, T. N., & Snaith, H. J. (2012). Efficient hybrid solar cells based on meso-superstructured organometal halide perovskites. Science, 338(6107), 643-647.
[20] Xing, G., Mathews, N., Sun, S., Lim, S. S., Lam, Y. M., Grätzel, M., & Sum, T. C. (2013). Long-range balanced electron-and hole-transport lengths in organic-inorganic $CH_3NH_3PbI_3$. Science, 342(6156), 344-347.
[21] Stranks, S. D., Eperon, G. E., Grancini, G., Menelaou, C., Alcocer, M. J., Leijtens, T., & Snaith, H. J. (2013). Electron-hole diffusion lengths exceeding 1 micrometer in an organometal trihalide perovskite absorber. Science, 342(6156), 341-344.
[22] Jeng, J. Y., Chiang, Y. F., Lee, M. H., Peng, S. R., Guo, T. F., Chen, P., & Wen, T. C. (2013). $CH_3NH_3PbI_3$ perovskite/fullerene planar-heterojunction hybrid solar cells. Advanced Materials, 25(27), 3727-3732.
[23] Eperon, G. E., Burlakov, V. M., Docampo, P., Goriely, A., & Snaith, H. J. (2014). Morphological control for high performance, solution-processed planar heterojunction perovskite solar cells. Advanced Functional Materials, 24(1), 151-157.
[24] Liu, M., Johnston, M. B., & Snaith, H. J. (2013). Efficient planar heterojunction perovskite solar cells by vapour deposition. Nature, 501(7467), 395.
[25] Zhou, H., Chen, Q., Li, G., Luo, S., Song, T. B., Duan, H. S., & Yang, Y. (2014). Interface engineering of highly efficient perovskite solar cells. Science, 345(6196), 542-546.
[26] Anaraki, E. H., Kermanpur, A., Steier, L., Domanski, K., Matsui, T., Tress, W., & Correa-Baena, J. P. (2016). Highly efficient and stable planar perovskite solar cells by solution-processed tin oxide. Energy & Environmental Science, 9(10), 3128-3134.
[27] Wojciechowski, K., Saliba, M., Leijtens, T., Abate, A., & Snaith, H. J. (2014). Sub-150 C processed meso-superstructured perovskite solar cells with enhanced efficiency. Energy & Environmental Science, 7(3), 1142-1147.
[28] Zhou, Y., Yang, M., Wu, W., Vasiliev, A. L., Zhu, K., & Padture, N. P. (2015). Room-temperature crystallization of hybrid-perovskite thin films via solvent–solvent extraction for high-performance solar cells. Journal of Materials Chemistry A, 3(15), 8178-8184.
[29] Nie, W., Tsai, H., Asadpour, R., Blancon, J. C., Neukirch, A. J., Gupta, G., & Wang, H. L. (2015). High-efficiency solution-processed perovskite solar cells with millimeter-scale grains. Science, 347(6221), 522-525.
[30] Yang, Z., Rajagopal, A., Jo, S. B., Chueh, C. C., Williams, S., Huang, C. C., & Jen, A. K. Y. (2016). Stabilized wide bandgap perovskite solar cells by tin substitution. Nano letters, 16(12), 7739-7747.
[31] Yang, W. S., Park, B. W., Jung, E. H., Jeon, N. J., Kim, Y. C., Lee, D. U., & Seok, S. I. (2017). Iodide management in formamidinium-lead-halide–based perovskite layers for efficient solar cells. Science, 356(6345), 1376-1379.

[32] Noh, J. H., Im, S. H., Heo, J. H., Mandal, T. N., & Seok, S. I. (2013). Chemical management for colorful, efficient, and stable inorganic–organic hybrid nanostructured solar cells. Nano letters, 13(4), 1764-1769.
[33] Im, J. H., Kim, H. S., & Park, N. G. (2014). Morphology-photovoltaic property correlation in perovskite solar cells: One-step versus two-step deposition of $CH_3NH_3PbI_3$. Apl Materials, 2(8), 081510.
[34] Burschka, J., Pellet, N., Moon, S. J., Humphry-Baker, R., Gao, P., Nazeeruddin, M. K., & Grätzel, M. (2013). Sequential deposition as a route to high-performance perovskite-sensitized solar cells. Nature, 499(7458), 316.
[35] Zhou, Y., Yang, M., Wu, W., Vasiliev, A. L., Zhu, K., & Padture, N. P. (2015). Room-temperature crystallization of hybrid-perovskite thin films via solvent–solvent extraction for high-performance solar cells. Journal of Materials Chemistry A, 3(15), 8178-8184.
[36] Heo, J. H., Lee, M. H., Jang, M. H., & Im, S. H. (2016). Highly efficient $CH_3NH_3PbI_{3-x}Cl_x$ mixed halide perovskite solar cells prepared by re-dissolution and crystal grain growth via spray coating. Journal of Materials Chemistry A, 4(45), 17636-17642.
[37] Thompson, A. W. (1972). Calculation of true volume grain diameter. Metallography, 5(4), 366-369.
[38] Smets, A. H., Jäger, K., Isabella, O., van Swaaij, R. A. C. M. M., & Zeman, M. (2016). Solar Energy: The physics and engineering of photovoltaic conversion technologies and systems. UIT.
[39] Sutter-Fella, C. M., Miller, D. W., Ngo, Q. P., Roe, E. T., Toma, F. M., Sharp, I. D., & Javey, A. (2017). Band Tailing and Deep Defect States in $CH_3NH_3Pb(I_{1-x}Br_x)_3$ Perovskites As Revealed by Sub-Bandgap Photocurrent. ACS Energy Letters, 2(3), 709-715.
[40] Zhumekenov, A. A., Saidaminov, M. I., Haque, M. A., Alarousu, E., Sarmah, S. P., Murali, B., & Mohammed, O. F. (2016). Formamidinium lead halide perovskite crystals with unprecedented long carrier dynamics and diffusion length. ACS Energy Letters, 1(1), 32-37.
[41] Sillen, A., & Engelborghs, Y. (1998). The correct use of “average” fluorescence parameters. Photochemistry and photobiology, 67(5), 475-486.
[42] Chin, X. Y., Cortecchia, D., Yin, J., Bruno, A., & Soci, C. (2015). Lead iodide perovskite light-emitting field-effect transistor. Nature communications, 6, 7383.
[43] Wang, Q., Shao, Y., Xie, H., Lyu, L., Liu, X., Gao, Y., & Huang, J. (2014). Qualifying composition dependent p and n self-doping in $CH_3NH_3PbI_3$. Applied Physics Letters, 105(16), 163508.
[44] Bi, C., Shao, Y., Yuan, Y., Xiao, Z., Wang, C., Gao, Y., & Huang, J. (2014). Understanding the formation and evolution of interdiffusion grown organolead halide perovskite thin films by thermal annealing. Journal of Materials Chemistry A, 2(43), 18508-18514.
[45] Moulder, J. F., Stickle, W. F., Sobol, P. E., & Bomben, K. D. (1992). Handbook of X-ray Photoelectron Spectroscopy, ed. by J. Chastain, Publ. by Perkin-Elmer Corporation.

[46] Sherwood, P. M. (1976). X-ray photoelectron spectroscopic studies of some iodine compounds. Journal of the Chemical Society, Faraday Transactions 2: Molecular and Chemical Physics, 72, 1805-1820.
[47] Chen, Q., Zhou, H., Hong, Z., Luo, S., Duan, H. S., Wang, H. H., & Yang, Y. (2013). Planar heterojunction perovskite solar cells via vapor-assisted solution process. Journal of the American Chemical Society, 136(2), 622-625.
[48] Pellaroque, A., Noel, N. K., Habisreutinger, S. N., Zhang, Y., Barlow, S., Marder, S. R., & Snaith, H. J. (2017). Efficient and stable perovskite solar cells using molybdenum tris (dithiolene) s as p-dopants for spiro-OMeTAD. ACS Energy Letters, 2(9), 2044-2050.
[49] Rana, A., Kumar, A., Rahman, M. W., Vashistha, N., Garg, K. K., Pandey, S., & Singh, R. K. (2018). Non-approximated series resistance evaluation by considering high ideality factor in organic solar cell. AIP Advances, 8(12), 125121.
[50] Wali, Q., Fakharuddin, A., & Jose, R. (2015). Tin oxide as a photoanode for dye-sensitised solar cells: current progress and future challenges. Journal of Power Sources, 293, 1039-1052.
[51] Baena, J. P. C., Steier, L., Tress, W., Saliba, M., Neutzner, S., Matsui, T., & Petrozza, A. (2015). Highly efficient planar perovskite solar cells through band alignment engineering. Energy & Environmental Science, 8(10), 2928-2934.
[52] Lin, S., Yang, B., Qiu, X., Yan, J., Shi, J., Yuan, Y., & Zhou, C. (2018). Efficient and stable planar hole-transport-material-free perovskite solar cells using low temperature processed SnO2 as electron transport material. Organic Electronics, 53, 235-241.
[53] Zhao, J., Wei, L., Liu, J., Wang, P., Liu, Z., Jia, C., & Li, J. (2017). A sintering-free, nanocrystalline tin oxide electron selective layer for organometal perovskite solar cells. Science China Materials, 60(3), 208-216.
[54] Kim, H. S., & Park, N. G. (2014). Parameters affecting I–V hysteresis of CH3NH3PbI3 perovskite solar cells: effects of perovskite crystal size and mesoporous TiO_2 layer. The journal of physical chemistry letters, 5(17), 2927-2934.
[55] Kempa, T. J., Cahoon, J. F., Kim, S. K., Day, R. W., Bell, D. C., Park, H. G., & Lieber, C. M. (2012). Coaxial multishell nanowires with high-quality electronic interfaces and tunable optical cavities for ultrathin photovoltaics. Proceedings of the National Academy of Sciences, 109(5), 1407-1412.
[56] Fu, Q., Tang, X., Huang, B., Hu, T., Tan, L., Chen, L., & Chen, Y. (2018). Recent progress on the long-term stability of perovskite solar cells. Advanced Science, 5(5), 1700387.
[57] Rajagopal, A., Yao, K., & Jen, A. K. Y. (2018). Toward perovskite solar cell commercialization: a perspective and research roadmap based on interfacial engineering. Advanced Materials, 30(32), 1800455.
[58] Li, Z., Yang, M., Park, J. S., Wei, S. H., Berry, J. J., & Zhu, K. (2015). Stabilizing perovskite structures by tuning tolerance factor: formation of formamidinium and cesium lead iodide solid-state alloys. Chemistry of Materials, 28(1), 284-292.
[59] Srivastava, R. (2017). Perovskite as light harvester: Prospects, efficiency, pitfalls and roadmap. Nanostructured Solar Cells; Das, N., Ed.; Intech: Rijeka, Croatia, 245-276.

Appendix

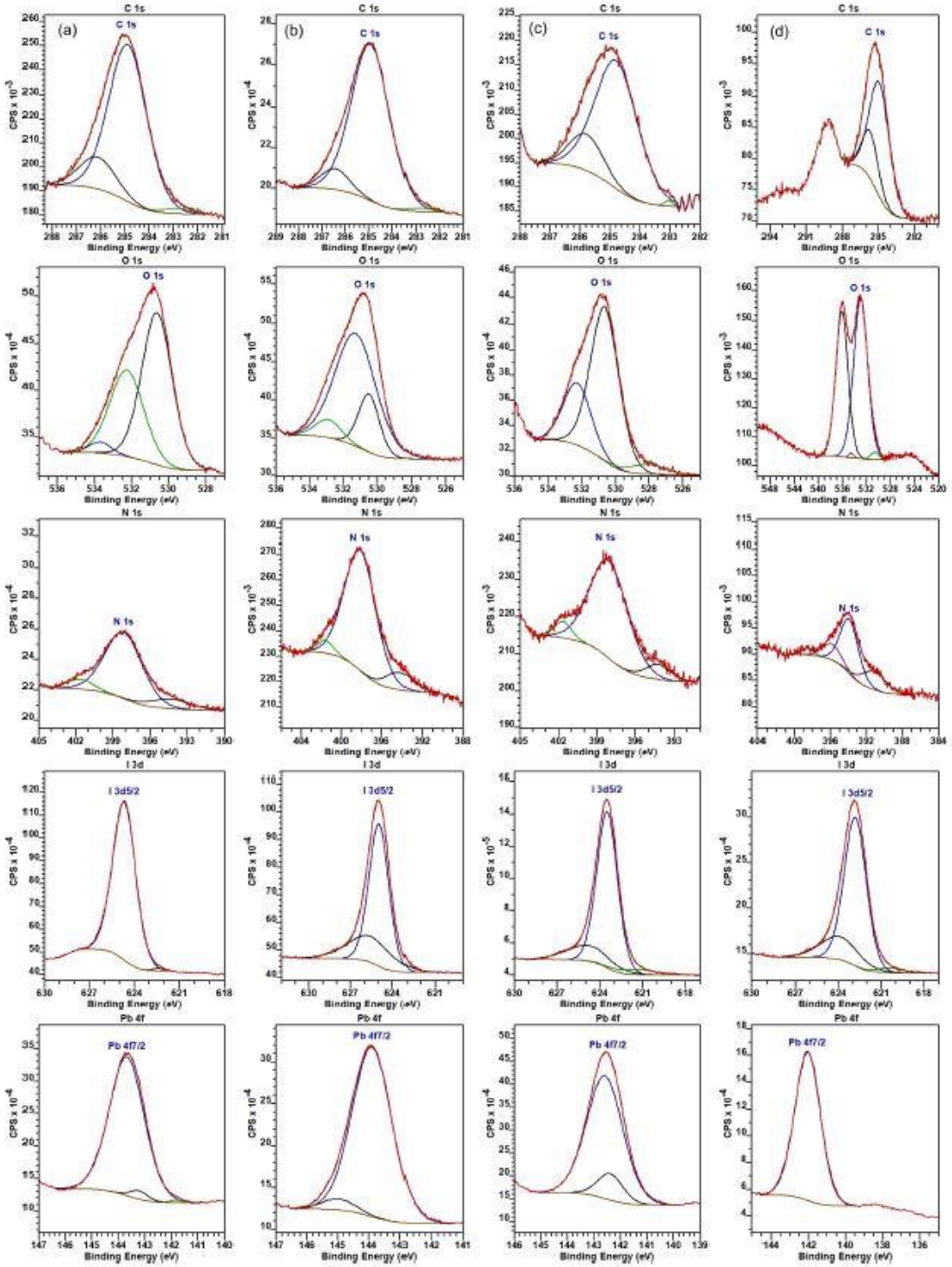

X-ray photoelectron spectroscopy (XPS) survey spectra of perovskite films documented for C 1s, O 1s, N 1s, I 3d5/2, and Pb 4f7/2. (a) One-step deposition, (b) Solvent-to-solvent extraction (SSE), (c) Hot casting, and (d) Mixed-cation show the core-level spectra of the different elements for perovskite films respectively

Vita

Shaimum Shahriar earned his Bachelor of Science degree in Electrical and Electronics Engineering from East West University, Bangladesh in 2012. He was a lecturer in Atish Dipankar University of Science and Technology from 2012 to 2013. In 2013, he joined Agrani Bank as a senior officer. He started his graduate school in UTEP's Electrical and Computer Engineering in the fall of 2014. In 2019, he received his Master of Science degree in Electrical and Computer Engineering from UTEP.

Shaimum did his doctoral research in organic inorganic halide perovskite solar cell. He published peer review journals in The American Institution of Physics (AIP), IOPscience, and Material Research Society (MRS). He had been published conference papers in IEEE PVSC and IEEE SusTech. He presented oral presentations in Grad Expo and Southwest Energy Science & Engineering Symposium in UTEP. He presented poster presentations in IEEE PVSC, 2015 and MRS, 2016. He attended Hands on Photovoltaic Experience (HOPE) at National Renewable Energy Laboratory (NREL) in summer, 2016.

While pursuing his degree, Shaimum worked as a Research and Teaching Assistant for ECE department. From fall 2016, he conducted Electronics I lab. He used use μA741 operational amplifiers, LF411 junction gate field-effect transistor (JFET) based operational amplifier to design noninverting, inverting amplifier, voltage follower, integrator, differentiator, and Electrocardiography (ECG) circuits. As a researcher, he worked with Dr. Deidra Hodges to fabricate and characterize perovskite thin films and fabricate planar structure perovskite solar cells. His best achievement was 18.75% power conversion efficiency by using SnO_2 based mixed cation perovskite solar cell.

Contact Information: shaimum52@gmail.com